Experimental exploration of gold semi-continuous films in the near- and far-field

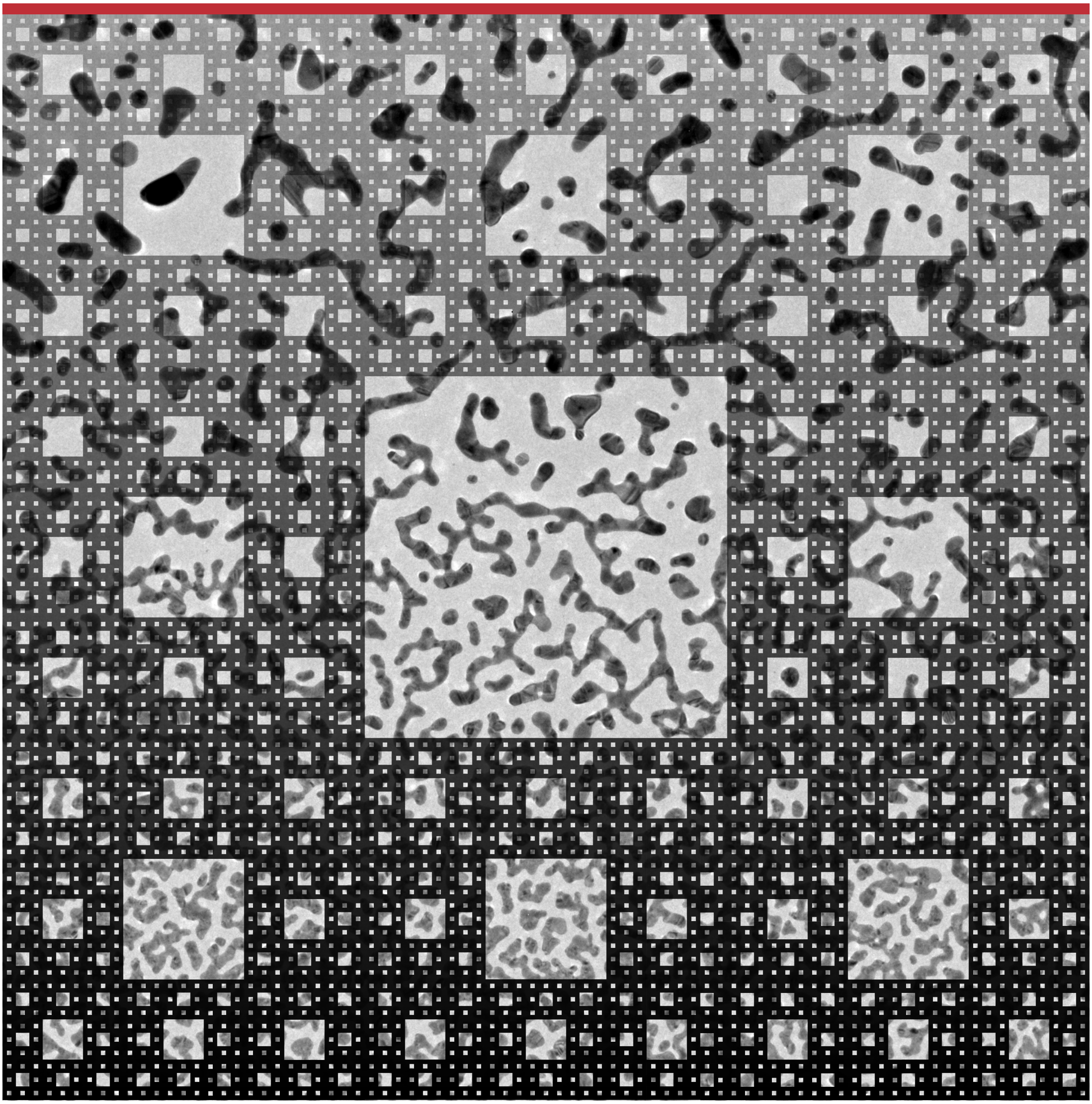

DTU Fotonik
Institut for Fotonik

Christian Frydendahl

TECHNICAL UNIVERSITY OF DENMARK

DOCTORAL THESIS

Experimental exploration of gold semi-continuous films in the near- and far-field

---

Author:
Christian FRYDENDAHL

Supervisors:
Assoc. Prof. Nicolas STENGER
Assoc. Prof. Andrei V. LAVRINENKO
Prof. N. Asger MORTENSEN

A thesis submitted in fulfilment of the requirements
for the degree of Doctor of Philosophy

in the

Structured Electromagnetic Materials, and
Plasmonics and Metamaterials groups,
Department of Photonics Engineering.

November, 2017

"You live and learn. At any rate, you live."

– Douglas Adams

Abstract (English)

This thesis is the final work of my PhD-study performed in the groups of *'Structured Electromagnetic Materials'* and *'Plasmonics and Metamaterials'* at the Technical University of Denmark (DTU). The thesis is a compilation of my research activities during that three year period, with a particular focus on experimental investigations of optical and plasmonic properties of self-organized gold percolation films, and how these can be modified by fs-laser pulses.

The thesis will start with a short introduction to metal optics and plasmonics in general. We will then introduce percolation systems and the concept of the percolation threshold. We detail how different percolation film morphologies can be fabricated by simple metal deposition techniques, and also discuss some of the physics behind such films' self-organization. We finally discuss how 'hotspots' of strong plasmonic excitation exists in such fractal structures.

We will then move on to introduce the concepts of gold photoluminescence and two-photon luminescence (TPL). We will show how it is possible to observe greatly enhanced TPL from gold percolation films, as compared to bulk gold. We will also prove that the greatest enhancement of TPL is found for gold films close to the percolation threshold. We will also briefly discuss how it is possible to observe strong white light continuum generation from such percolation films, but the physics responsible are still poorly understood.

To continue our discussion of results, we will briefly have to introduce the techniques of scanning near-field optical microscopy (SNOM) and electron energy-loss spectroscopy (EELS). We also show some partial SNOM results from experiments done at DTU.

Using high power fs-laser pulses, we demonstrate that it is possible to locally extinguish the TPL-signal from gold percolation films on silicon substrates. This effect proves to be strongly polarization sensitive, only extinguishing the TPL-signal from polarizations parallel to that of the writing laser. We explain the origin of this writing effect to be the photothermal melting and reshaping of plasmonic hotspots in the percolation films. As only those hotspots that match the polarization and wavelength of the laser are reshaped, the result is a polarization and wavelength sensitive extinction of TPL.

When we repeat this laser writing experiment on percolation films on thin glass substrates, we find a very different kind of laser writing effect. Due to the poorer heat conductivity of glass compared to silicon, the heat energy is no longer confined to just the local geometry that supports the hotspots.

The result is a total reshaping of the film. We do however still report a polarization sensitive plasmonic response, this time showing plasmon resonances aligned parallel to the writing laser's polarization. We record EELS maps of our structures and compare them to finite-element simulations of the same morphologies, explaining the origin of the resonances to be from nanorod-like particles that have been shaped by the laser writing.

Finally a summary and outlook is provided, detailing how these results could be used for plasmonic laser writing applications, like ultra-dense data storage.

Resumé (Danish)

Denne afhandling er det sidste værk i mit PhD-studie udført i *'Structured Electromagnetic Materials'* og *'Plasmonics and Metamaterials'* grupperne på Danmarks Tekniske Universitet (DTU). Afhandlingen er en samling af mine forskningsaktiviteter igennem denne 3-års periode, med et særligt fokus på eksperimentel udforskning af optiske og plasmoniske egenskaber af selvorganiserede guldperkolationsfilm, samt hvordan disse kan ændres med fs-laserpulser.

Afhandlingen starter med en kort introduktion til metaloptik og plasmonik generelt. Vi vil så introducere perkolationssystemer og konceptet om perkolationsgrænsen. Vi detaljere hvordan forskellige perkolationsfilmsmorfologier kan fremstilles ved simple metaldeponeringsteknikker, og diskutere også nogle af de fysiske mekanismer der står bag sådanne films selvorganisation. Endeligt diskutere vi hvordan 'hotspots' af stærk plasmonisk excitation findes i sådanne fraktale strukturer.

Vi fortsætter så ved at introducere koncepterne guldfotoluminescens og to-foton luminescens (TPL). Vi viser hvordan det er muligt at observere skarpt forøget TPL fra guldperkolationsfilm, sammenlignet med solidt guld. Vi beviser også at den største forøgelse af TPL findes i guldfilm nær perkolationsgrænsen. Vi vil også kort diskutere hvordan det er muligt at observere stærk hvid-lys kontinuumgeneration fra sådanne perkolationsfilm, men den fysiske mekanisme bag er stadig dårligt forstået.

For at fortsætte vores diskussion af resultater, må vi kort introducere teknikkerne skanning nærfelts optisk mikroskopi (SNOM) og elektron energitabs-spektroskopi (EELS). Vi viser også nogle delvise resultater fra SNOM-eksperimenter udført på DTU.

Ved brug af fs-laserpulser med høj effekt, demonstrere vi at det er muligt at lokalt slukke for TPL-signalet fra guldperkolationsfilm på siliciumsubstrater. Denne effekt viser sig at være stærkt polarisationsfølsom, da kun TPL-signalet fra polarisationer parallel med polarisationen af skrivelaseren slukkes. Vi forklarer årsagen af denne skriveeffekt som værende smeltningen og omformningen af plasmoniske hotspots i perkolationsfilmene. Da kun de hotspots som matcher polarisationen og bølgelængden af laseren er omformet, bliver resultatet en polarisations- og bølgelængdefølsom slukning af TPL.

Når vi gentager dette laserskrivningseksperiment på perkolationsfilm på tynde glassubstrater, finder vi en meget anderledes laserskrivningseffekt. På grund af den ringere varmeledningsevne af glas sammenlignet med silicium, er

varmeenergien ikke længere begrænset til den lokale geometri som understøtter hotspots'ene. Resultatet er en totalomformning af filmen. Vi finder dog stadigt et polarisationsfølsomt plasmonisk respons, denne gang i form af plasmonresonanser der er alignet parallelt til skrivelaserens polarisation. Vi optager EELS-kort af vores strukturer og sammenligner disse med endeligt-element simuleringer af de samme morfologier. Fra disse forklarer vi at årsagen til resonanserne er nanostavlignende partikler der er formet under laserskrivningen.

Endeligt gives et resumé og et outlook. Heri detaljeres hvordan disse resultater kunne anvendes i plasmoniske laserskrivningsanvendelser, så som datalagring med ultrahøj tæthed.

Acknowledgements

I would like first to thank my former supervisor, Prof. Philip Hofmann at Aarhus University. If not for his words of encouragement during my Master's studies, I would not have had the confidence or ambition to pursue a further career in research.

I would also like to sincerely thank my three supervisors: Nicolas, Asger, and Andrei. Before starting this PhD-study I had very limited knowledge or experience with experimental optics, and next to no knowledge of plasmonics. I thank them for giving me this opportunity, introducing me to so many interesting new topics in physics, and for providing me with counsel and guidance through these three years. I can barely believe now, how much I have learned in this short amount of time, and I certainly could not have done so without their help.

I also extend my thanks to all current and former members of the *'Structured Electromagnetic Materials'* and *'Plasmonics and Metamaterials'* groups. You have all contributed to an amazing environment in which to perform a PhD-study, with amble time for stimulating scientific discussions. Special thanks goes to my office-mates and fellow PhD-students, Kåre, Johan, Mathias, and André. Even if I have not had the opportunity to explicitly collaborate and work closely with all of you, I have still learned many valuable things from our open discussions in the office about science, life, politics, and everything else in the observable universe.

Most of my work presented here, has been the product of a strong collaboration with the group of Prof. Sergey I. Bozhevolnyi at the University of Southern Denmark. I am deeply grateful to everyone that has participated in this collaboration, as well as to all my other co-authors and collaborators in my projects during the PhD. Even though several of my ideas and projects did not come to full fruition during the three years, I have still learned many skills and lessons for the future from them. An extra special thanks goes to Taavi, for assisting me with additional simulations for one of the figures in this thesis.

I will also take this opportunity to offer my most sincere gratitude to the members of my PhD-evaluation committee: Prof. Mark I. Stockman, Prof. Uriel Levy and Prof. Peter Uhd Jepsen. Thank you for taking time out of your busy schedules to not only read this thesis, but also to participate in the evaluation of its contents.

Finally, I wish to thank my friends, family and girlfriend – for always offering me support, love, kindness, and innumerable distractions from my work.

List of Publications

Journal articles

A: S. M. Novikov, J. Beermann, **C. Frydendahl**, N. Stenger, V. Coello, N. A. Mortensen, and S. I. Bozhevolnyi. Enhancement of two-photon photoluminescence and SERS for low-coverage gold films. Optics express **24**, 16743-16751, 2016.

B: S. M. Novikov, **C. Frydendahl**, J. Beermann, V. A. Zenin, N. Stenger, V. Coello, N. A. Mortensen, and S. I. Bozhevolnyi. White light generation and anisotropic damage in gold films near percolation threshold. ACS Photonics **4**, 1207-1215, 2017.

C: **C. Frydendahl**, T. Repän, M. Geisler, S. M. Novikov, J. Beermann, A. V. Lavrinenko, S. Xiao, S. I. Bozhevolnyi, N. A. Mortensen, and N. Stenger. Optical reconfiguration and polarization control in semi-continuous gold films close to the percolation threshold. Nanoscale, **9**, 12014-12024, 2017.

Conference contributions

I: **C. Frydendahl**, S. M. Novikov, J. Beermann, N. Stenger, N. A. Mortensen, and S. I. Bozhevolnyi. Enhancement of two-photon photoluminescence for low coverage gold films. NFO **14**, Tu-9P-7, 2016.

II: S. M. Novikov, **C. Frydendahl**, J. Beermann, V. A. Zenin, N. Stenger, V. Coello, N. A. Mortensen, and S. I. Bozhevolnyi. White light generation and anisotropic damage in gold films near percolation Threshold. SPP **8**, P-07-23, 2017.

III: **C. Frydendahl**, T. Repän, M. Geisler, S. M. Novikov, J. Beerman, A. Lavrinenko, S. Xiao, S. I. Bozhevolnyi, N. A. Mortensen, and N. Stenger. Near- and far field spectroscopy of semi-continuous gold films with optically induced anisotropy. SPP **8**, P-07-22, 2017.

Contents

Abstract (English) **iii**

Resumé (Danish) **v**

Acknowledgements **ix**

List of Publications **xi**

1 Introduction **1**

1.1 Outline 2

2 Optical properties of metals **5**

2.1 Free electrons 5

2.2 The Drude model 6

2.2.1 Thin metal films 8

2.3 Interband transitions 10

3 A brief introduction to plasmonics **13**

3.1 Bulk plasmons 13

3.2 Surface plasmon polaritons 14

3.2.1 Localized surface plasmons 20

4 Metal percolation films **23**

4.1 Percolation theory 23

4.2 Fabrication 26

4.2.1 The Volmer-Weber growth process 26

4.2.2 E-beam metal deposition 28

4.3 Optical properties 31

4.3.1 Theoretical approaches 31

4.3.2 Experimental investigations 35

5 Photoluminescence in gold **39**

5.1 Two-photon luminescence 40

5.1.1 Measurement of TPL 41

5.1.2 Enhancement of TPL 43
5.2 White light generation 48

6 Near-field observation techniques 51

6.1 The optical near-field 52
6.2 Scanning near-field optical microscopy 53
6.2.1 Fiber optic probes and shear-force feedback 53
6.2.2 The DME DS 45-40 SNOM 54
6.2.3 Measurements 56
6.2.4 Scattering-type SNOM 58

7 Electron Energy-loss spectroscopy 61

7.1 Transmission electron microscopy 61
7.1.1 The energy-loss spectrum 63
7.2 Mapping plasmons with electrons 65

8 Optical modification of semi-continuous gold films 69

8.1 Photothermal processes in metal nanoparticles 69
8.1.1 Substrate influence 72
8.2 Polarization inscription 74
8.2.1 Silicon substrates 74
8.2.2 Glass substrates 77
8.3 Reconfiguration of modes 83

9 Conclusion 87

9.1 Outlook 88

Bibliography 91

Paper A - Enhancement of two-photon photoluminescence and SERS for low-coverage gold films 103

Paper B - White Light Generation and Anisotropic Damage in Gold Films near Percolation Threshold 113

Paper C - Optical reconfiguration and polarization control in semi-continuous gold films close to the percolation threshold 123

To my parents, Ole and Elsebeth.

1 Introduction

Metallic nanostructures posses the ability to localize and enhance optical fields down to the nanoscale via collective excitations of their conduction electrons. These excitations are known by their quantized quasi-particle representation as plasmons, and have been the subject of intense study in the recent decades[1]. The ability to concentrate and manipulate light on the nanoscale offers many new promising applications in the field of optics. By carefully engineering metallic nanostructures, their optical properties can be fine-tuned to allow for sub-diffraction light focusing for spectroscopy and sensing[2], enhancing light-matter interactions in new emerging 2D materials[3, 4], and quantum information processing technologies[5–7]. In the last few years in particular, interest has also been growing in the field of plasmonic colours[8]. By tuning the spectral reflectivity of a surface due to plasmonic structures on it, it is possible to create colour printed images with sub-diffraction pixel resolution[9–11].

Nanometre sized structures are needed to realize these applications, and defining features on the nanoscale often requires elaborate fabrication methods like electron-beam lithography (EBL) and focused ion beam (FIB) milling[12]. EBL allows for very precise and reproducible definition of nanostructures, but at the cost of several time consuming process steps to produce a mask pattern in a polymer resist[13]. In addition, the spatial resolution limit is still in the order of 10 nm for state of the art systems[13]. FIB milling can offer an alternative mask-less fabrication method of similar resolution to EBL. However, the method still requires long pattern writing times, and also comes with the potential risk of contaminating the structure materials with the type of ions used for milling[14], potentially altering their optical properties.

However, another alternative exists in the realm of self-assembled and self-organized materials. By letting already nanoscale particles or elements structure themselves, sub-nanometre gaps and protrusions can routinely be achieved. Such small features are perfect for hosting plasmons that enable high levels of field-enhancement and localization. The big advantage of such self-assembled structures is their fast and easy, bottom-up, fabrication methods[15–17]. Such structures are naturally limited in what structures can be achieved, based on their component sizes and method of their self-assembly. It is however possible to alter their assembly processes directly to somewhat expand the range of possible structures[18]. Another method to expand the range of achievable structures, is by laser induced photothermal reshaping post-assembly[11, 19–24].

In this thesis, we will study the optical properties of self-organized gold percolation films, and how it is possible to modify these properties by fs-laser induced photothermal reshaping. The intrinsic nanostructured morphology of percolation metal films comes from the Volmer–Weber growth process for metals on dielectric substrates[25]. During a deposition process, the metal atoms have a mutually strong interaction, while they will bond less with the substrate. During the earliest part of the deposition, this leads to the formation of isolated clusters. With continuing deposition these initial clusters tend to grow in the substrate plane, eventually reaching a 'percolation threshold' where they merge to form a connected system. The total metal film is now dominated by one large cluster with several gaps in it. Any further metal deposition will close up these remaining gaps in the film morphology, and eventually the system will transition into a continuous metal film. Any additional deposition will then simply be metal on metal growth.

Using standard metal evaporation systems, it is possible to fabricate large-scale areas of such metal percolation films, wherein the smallest feature sizes can be at the sub-nanometre scale[25]. Semi-continuous metal films thus make an ideal alternative platform for many plasmonic technologies, and have been the subject of much theoretical and experimental study already[19, 26–30].

1.1 Outline

The first two chapters will serve to introduce much of the underlying physics for understanding light's interaction with metals, both at the macro- and nanoscale. Chapter 2 will briefly introduce the simple and intuitive Drude model for a metal's dielectric function, as well as some of its results and limitations. Chapter 3 will introduce the concept of collective plasma oscillations (plasmons) in metals. The purpose of these two chapters is to (hopefully) help establish a simple intuition of plasmonics for the unfamiliar reader. For readers already familiar with the topics discussed, these chapters can be skipped without much consequence. Further details on these concepts are available in references [31–34].

In chapter 4 we will look at how these discussed concepts can be realized in the random metal structures known as percolation films. We will discuss how such films can be fabricated, the underlying physics behind their self-organization, and how they can be modelled theoretically. We will then look at a specific application of such film geometries to enhance two-photon luminescence (TPL) from gold, and how it is possible to generate a white light continuum from these films in chapter 5.

In chapter 6 we will detail a practical limitation of experimental optics known as the diffraction limit. We will discuss how it is possible to still perform optics in the near-field to circumvent this limitation. We will in this same chapter detail the basic working principles of aperture- and aperture-less scanning near-field optical microscopes (SNOMs), and look at some example images recorded from gold percolation films. To go even further beyond the spatial resolution of modern SNOM devices, we will also cover how it is possible to investigate plasmon resonances by electron-energy loss spectroscopy (EELS) in a transmission electron microscope (TEM) in chapter 7.

In chapter 8 we will discuss how it is possible to alter the morphology of plasmonic nanostructures by photothermal processes from fs-laser illumination. We will show how it is possible change the TPL-enhancement from gold percolation films on a silicon substrate locally by a fs-laser writing process. Using TEM and EELS measurements, We will also detail the morphology and plasmon resonance changes from a similar laser writing process for percolation films on thin glass substrates.

Finally, we will conclude with a summary of many of the results presented throughout the thesis, and present a short outlook of further work that could be done to expand on these results for future applications.

2 Optical properties of metals

Perhaps the most universally striking optical feature of metals, when polished to a smooth surface, is their high reflectivity. Early human civilizations around the world have utilized mirrors of polished copper as early as 4000 B.C.[35], so the ability of metals to reflect light has been well known through a majority of human civilization. Despite this, our current theoretical framework for understanding the properties of metals only begins around the 20th century with P. Drude's proposal of a kinetic model for the free charge carriers in metals in 1900[36, 37]. The Drude model is a classical model, and we know it only offers an incomplete picture of the physics as we understand them today. However, the model still provides good agreement with many observations and offers a simple intuitive framework, and as such remains popular.

In the following we will discuss how from simple kinetic considerations we can explain much of the broadband reflective properties of metals, and we will also look at the initial breakdown of this simple model when dealing with imperfect metals that show absorption due to interband transitions in their band structure.

2.1 Free electrons

When collecting individual atoms together to form a solid material, the individual atomic energy levels of the solid's constituent atoms will start to shift and merge together to form broad bands of electronic states, instead of discrete levels like in an atom. This is also the basis for the very successful electronic band structure theory of condensed matter physics[32].

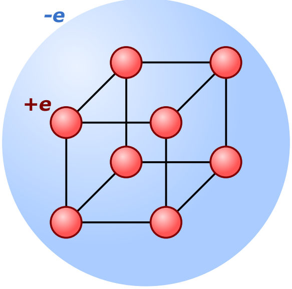

Figure 2.1: Schematic of a metal. The positively charged atomic nuclei make up a rigid lattice, and the conduction electrons form a charged plasma surrounding the lattice.

Because of the types of bonds and crystal structures that become most energetically favourable when bonding metal atoms together, the resulting solid from this collection of atoms will not have any energy gap between its valence and conduction bands in its band structure. This means that for a metal, electrons are always populating states in the conduction band, no matter their energy. Here they will approximately behave like free electrons, as the electrons in lower energy states are tightly bound to their atomic cores in the crystal lattice, and will help screen off their host atomic nuclei's positive charge. The end result is that we can treat the metal as a static lattice of ions, with a plasma of electrons weakly bound to it[1]. A schematic drawing of this can be seen on Fig. 2.1.

2.2 The Drude model

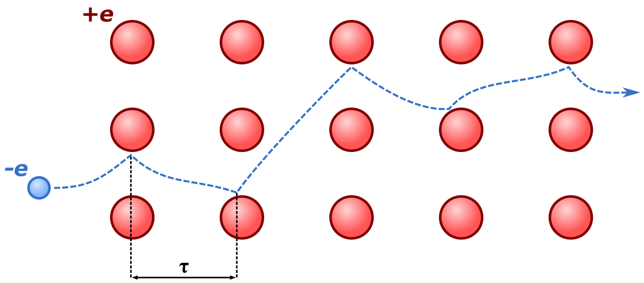

Figure 2.2: Schematic of a Drude metal. A semi-free electron propagates and experiences scattering events with the atomic lattice, with a mean time of τ between events.

In the framework as described above, we find the Drude model for metal conductivity. The model operates with simple classical physics, and assumes that the conduction electrons in the metal can propagate through the metal if an electric field is applied. During their propagation through the metal the electrons will scatter off of the positive ionic lattice, with some mean time, τ, between scattering events (see Fig. 2.2). Different metals can now be understood by having different scattering times, explaining their differences in electrical conductivity.

We can now consider how the electric field of external optical radiation would couple to the conduction electrons in a metal. The field of propagating light is an oscillating transverse wave, so if we consider an electron via an oscillator model. We can write an equation of motion for the displacement, x, of an electron with mass m_e, by a field, $E(t)$, as:

---

[1] Especially since the ions are many orders of magnitude more massive than the electrons.

$$m_e \frac{d^2x}{dt^2} + m_e \gamma \frac{dx}{dt} = -eE(t) = -eE_0 \mathrm{e}^{-i\omega t}. \tag{2.1}$$

The first left-hand term is the acceleration of the electron, while the second left-hand term is the frictional damping of the electron from its scattering with the lattice ions. We can correlate the damping coefficient, γ, to the scattering time in the Drude conductivity model, τ, as simply $\gamma = 1/\tau$. The right-hand side of eqn. 2.1 is simply the force of the oscillating optical field on the electron, with E_0 the amplitude of the electric field, and ω its angular frequency. Notice the absence of a restoring force term, as we are treating the electrons as only weakly coupled to the lattice, we neglect their interaction with the ions.

By solving eqn. 2.1 by substitution of $x = x_0 \mathrm{e}^{i\omega t}$, and regarding the polarizability of a system of N such electrons as $P = Nex$, it is possible to arrive at the following equation for the relative dielectric function, $\epsilon_r(\omega)$, of a Drude metal:

$$\epsilon_r(\omega) = 1 - \frac{\omega_p^2}{\omega^2 + i\gamma\omega}, \tag{2.2}$$

with ω_p the plasma frequency, defined as:

$$\omega_p = \left(\frac{Ne^2}{\epsilon_0 m_e} \right)^{1/2}. \tag{2.3}$$

We will see later how the plasma frequency is an important parameter in understanding metals' optical and plasmonic properties. It's worth noting the only 'free' parameter in the definition of ω_p is the electron count N. This means metals will have plasma frequencies in the ultraviolet range, while ceramics and doped semiconductors can have infrared plasma frequencies[38].

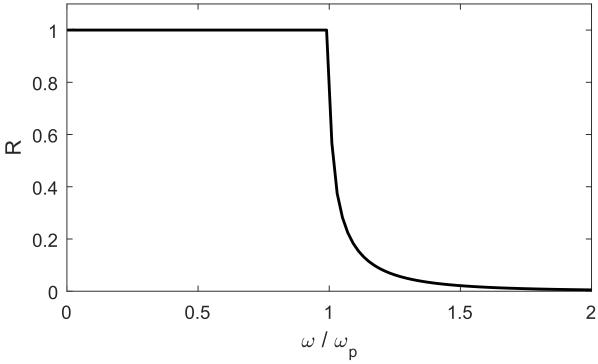

Figure 2.3: Reflectivity spectrum, R, of a lossless Drude metal, showing the transition to transparency for frequencies above ω_p.

If we consider the case of low damping ($\gamma = 0$), we can write the refractive index as $n = \sqrt{\epsilon_r}$, and from the refractive index we can calculate the reflectivity as:

$$R = \left| \frac{n-1}{n+1} \right|^2 . \tag{2.4}$$

From plotting this expression in units of ω_p in Fig. 2.3, we see how for frequencies below the plasma frequency the metal will act as a perfect reflector, while for frequencies above ω_p the metal becomes transparent.

2.2.1 Thin metal films

In the previous section we have only treated the case for bulk metals, but it is worth briefly mentioning how very thin ($1 - 15\,\mathrm{nm}$) metallic films will differ from the bulk properties quite dramatically due to the finite skin depth of electric fields in metals. If we consider the absorption of the electric field strength through the metal by a simple Beer's absorption law, the skin depth, δ, at which the field has decayed by a factor of e^{-1}, can be defined as:

$$\delta = \left(\frac{2}{\sigma_0 \omega \mu_0} \right)^{1/2} , \tag{2.5}$$

with σ_0 the DC conductivity of the metal. From this we can estimate the typical[2] skin depth of metals in the visible spectrum to be around ~10 nm. As a result we can expect metal films below and around this thickness to be partially transparent, as the light is able to partially pierce through the metal.

---

[2] A typical metal has σ_0~10^7 S/m and visible light has ω~10^{15} Hz.

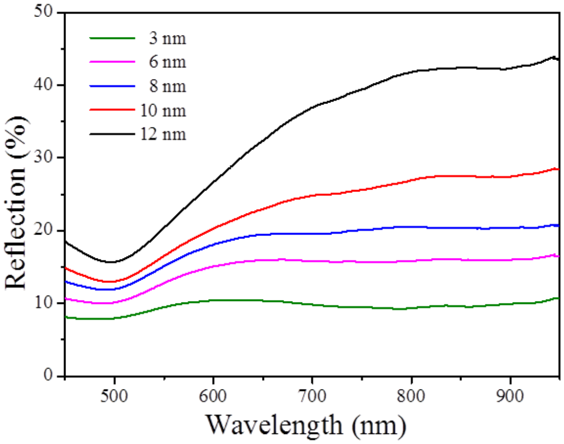

Figure 2.4: Reflectivity spectra of thin semi-continuous gold films of various thicknesses, deposited on glass substrates.

In Fig. 2.4.a we see the reflection spectra of several thin semi-continuous gold films. We see that for increasing film thickness the reflectivity increases, as expected. Likewise we see that the reflectivity is larger for longer wavelengths. However, around the 520 nm range we see a strong decrease in reflectivity. We could expect this to be explained by the plasma frequency of gold, but gold's ω_p corresponds to a wavelength of ~145 nm.

The essence of the problem here, is that our simple lossless model for metals does not explain the different colours of metals. It is thus only suitable for describing certain metals in certain wavelength ranges[3]. In the Drude framework, our main way of adding losses would be by electron scattering, either off of the lattice or lattice defects. The net effect of this would be a general broadband reduction in reflection, as this kind of scattering just equally removes energy from the electrons. It is possible to introduce this kind of wavelength selective reduction by adding resonant Lorentzian oscillator terms to eqn. 2.2 to make a Drude-Lorentz model[39]. However, to understand the physical cause of the absorption we will need a more detailed framework.

---

[3] For example: The Drude model is quite accurate for aluminium and silver in the the visible range, and gold and copper in the infrared range.

2.3 Interband transitions

In this section, we will discuss how band structure theory can explain the different colours of metals through specific energy absorption by so-called interband transitions. We will also expand our Drude model to account for the different colours of metals.

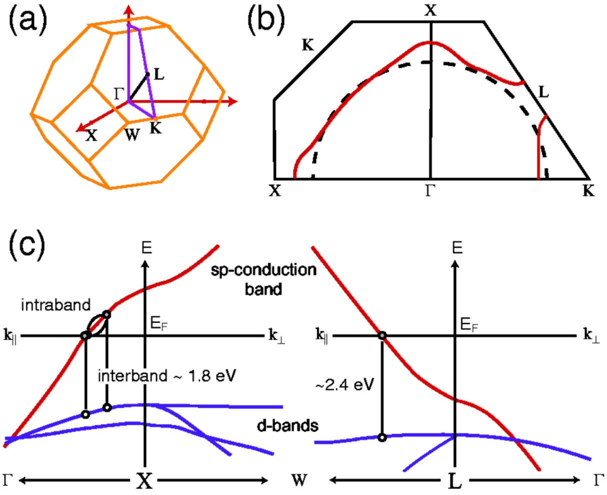

Figure 2.5: (a) Symmetry points in gold's first Brillouin zone. **(b)** The Fermi surface as mapped out along a path between the high-symmetry points X and L. Near these points the Fermi surface is deformed, compared with that of free electrons (dashed circle). This is caused by Van Hove singularities in the density of states. **(c)** Shows the band structure near X and L, close to the Fermi level. The interband edges are marked. The many parallel d-bands give rise to large density of states that permits interband transitions. Reproduced from reference [40].

Gold has the electron configuration $[\mathrm{Xe}]4f^{14}5d^{10}6s^{1}$, and a face-centred cubic crystal structure. This results in the partial band structure seen on Fig. 2.5. We see that the outer d- and sp-electron states of gold form two very different classes of bands. The d-bands are all very tightly stacked horizontally in a narrow energy range below the Fermi level, while the more free-electron-like sp-bands criss-cross each other and go far below and far above the Fermi level. It's exactly around these points where the sp-states cross through the Fermi level and the region of d-states that interband transitions can occur. The smallest gap between the bands sets the edge for where interband transitions can start to happen. For gold this is around 2.4 eV (~520 nm, which is where we start to see the strong decrease in reflection in Fig. 2.4). Essentially, gold becomes a strong absorber for wavelengths below this, and as these wavelengths of visible light are not reflected but absorbed, it causes the characteristic colour of gold. In chapter 5 we will study how it is possible to stimulate photoluminescence from this 'band gap', in a process somewhat reminiscent of that of photoluminescence in semiconductors.

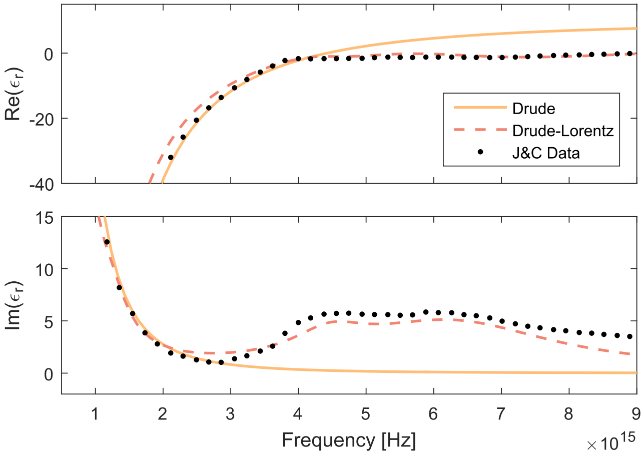

Figure 2.6: Real and imaginary parts of gold's dielectric function. A simple Drude model (details in text) and a Drude-Lorentz model, as given in reference [39]. Experimental data from P. B. Johnson and R. W. Christy[41]

To account for the interband transitions in our Drude framework, we need to perform either of two modifications to eqn. 2.2. First, we can add a constant term to account generally for the material response at high frequency, ϵ_∞, where the ω-dependent term of eqn. 2.2 otherwise goes to zero:

$$\epsilon_r(\omega) = \epsilon_\infty - \frac{\omega_p^2}{\omega^2 + i\gamma\omega} . \tag{2.6}$$

However, as mentioned before, if we truly want to capture the wavelength dependent nature of the interband transitions, we need to add additional resonant Lorentz oscillator terms[39]. A Drude-Lorentz model can look like:

$$\epsilon_r(\omega) = 1 - \frac{f_0\omega_p^2}{\omega^2 - i\gamma_0\omega} + \sum_{n=1}^{N} \frac{f_n\omega_p^2}{\omega_n^2 - \omega^2 - i\gamma_n\omega} , \tag{2.7}$$

where f_n is the oscillator strength, ω_n the resonance frequency, and γ_n the damping rate of the n'th oscillator. Fig. 2.6 shows comparisons between experimental data and a simple Drude model with $\epsilon_\infty = 10$, $\omega_p = 1.4 \cdot 10^{16}$ Hz and $\gamma = 1.13 \cdot 10^{14}$. The Drude-Lorentz model with $N = 5$ of reference [39] is also shown.

From Fig. 2.6 we clearly see how the simple Drude model breaks down at the onset of interband transitions around $4 \cdot 10^{15}$ Hz (roughly ~550 nm), while the Drude-Lorentz model much more closely resembles the data. We do however still see that the simple Drude model perfectly represents the data for the low frequency range, where gold behaves very close to an ideal metal. The conclusion is thus simply: If working with a metal in a frequency range where no interband transistions can occur in the metal, then a simple Drude model like eqn. 2.6 is perfectly sufficient, otherwise a more advanced Drude-Lorentz model like eqn. 2.7 will be required.

In the following chapters we will see how nanostructuring of metals can introduce new optical properties, based on collective electron oscillations near a metal/dielectric interface. The general bulk properties as discussed here remain important for understanding the optical response of metal nanostructures, and especially the losses and optical absorption associated with interband transitions in gold will be important for later chapters.

3 A brief introduction to plasmonics

In this chapter we will introduce the concept of collective electron oscillations, also better known by their quantization as quasi-particles called plasmons[1]. We will focus our attention on plasmons in metals using the previously discussed free electron picture of chapter 2. We will start with discussing bulk plasmons, and then moving on to surface plasmon polaritons (propagating surface waves) and finish with localized surface plasmons.

3.1 Bulk plasmons

Bulk plasmons are generally of little interest in optics (for reasons that will become clear later). They do however make a suitable starting point for discussing plasmons, as they are a simple pedagogical demonstration of the concepts. They are also important historically, as they were the first plasmon phenomenon to be realized and understood experimentally[42–44].

Bulk plasmons were initially observed independently by G. Ruthemann[42] and W. Lang[43] in 1948 as straight lines in electron-energy loss spectra through thin metal films (We will discuss this technique in broader detail in chapter 7). Y. Cauchois initially proposed in 1952 that excitations of electrons via interband transitions could be responsible[45] (we will discuss a very interesting consequence of this kind of excitation in chapter 5). However, the shapes of the observed spectra were found to be incompatible with interband transitions. D. Pines and D. Bohm would later propose a model for plasmons being responsible[46, 47]. H. Watanabe would go on to experimentally verify the plasmon explanation in 1956 by carrying out a series of measurements across several materials, testing the spectra's dependence on the angle of the electron beam and the temperature of the sample[44].

We can look at a plasma oscillation for a metal crystal in a very simple classical oscillator picture. If we consider a displacement, y, of the free electron plasma of N electrons surrounding a positive ion lattice in a metal thin film, like in Fig. 3.1[1].

---

[1] This initial displacement could be caused by an electron beam passed through the metal film.

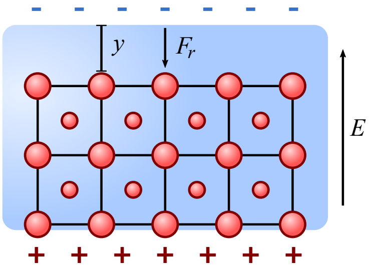

Figure 3.1: The displacement, y, of the electron plasma surrounding a metal crystal. The offset in charges causes an electric field, E, along the displacement. This results in a restoring force, F_r, pulling the electrons back towards the lattice.

The displacement of charges will result in a net charge distribution $+Ney$ on the bottom of the lattice, and $-Ney$ on the top. This then results in the electric field $E = Ney/\epsilon_0$ from the bottom to the top of the lattice. The charged electrons will now feel a restoring force, $F_r = -eE$, giving the following equation of motion:

$$m_e \frac{d^2y}{dt^2} = -eE = -y\frac{Ne^2}{\epsilon_0}, \tag{3.1}$$

which has the well-known solution of the form: $y(t) = y_0 \cos(\omega_p t)$, with the plasma frequency $\omega_p = \sqrt{Ne^2/\epsilon_0 m_e}$ as we also found it in chapter 2. The bulk plasmons observed is electron-energy loss experiments are in integer multiples of the energy $\hbar\omega_p$[31]. From our initial assumptions of the oscillation mode, we see that the bulk plasmon is exclusively a longitudinal oscillation mode[2]. This means that it is impossible to excite directly with light (outside some extreme circumstances), as the electric field of light is always transverse to its propagation direction[32]. We will thus not discuss bulk/volume plasmons in more detail here, as they are outside the scope of this thesis.

3.2 Surface plasmon polaritons

Following the developments on bulk plamons, R. H. Ritchie would go on to predict the existence of surface plasmons in 1957[48]. Ritchie's original motivation for further developing the theory on plasmons, was to explain the presence of lower energy losses present in the past experiments, which were not accounted for in the bulk plasmon picture[49].

---

[2] This fact can also be shown in greater detail, see reference [32]

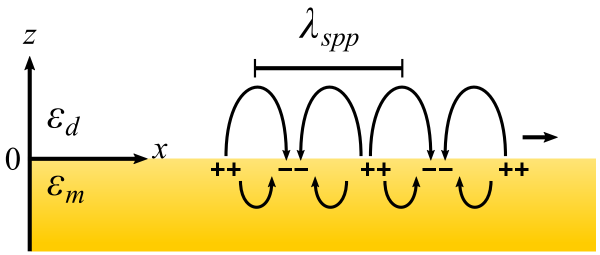

Figure 3.2: Geometry of a surface plasmon polariton at the interface of a metal and dielectric. The electrons near the interface oscillate in a longitudinal wave along the interface, creating a propagating transverse electric field along the interface.

As we saw above, bulk/volume plasmons are longitudinal modes of oscillation. If we now focus on just the interface between a dielectric (like air) and a metal, we can examine surface plasmons. Surface plasmons are a mix of transverse and longitudinal oscillations, and as such can couple to external radiation, forming a surface plasmon polariton. Surface plasmon polaritons were first demonstrated by optical excitation by A. Otto in 1968[50], and only a few months later independently verified by E. Kretschmann and H. Raether[51][3].

If we choose our coordinates such that the interface sits at the point $z = 0$ (see Fig. 3.2), then we can write the dielectric function as:

$$\epsilon_j(\omega) = \begin{cases} \epsilon_d(\omega) & \text{for } z > 0 \\ \epsilon_m(\omega) & \text{for } z < 0 \end{cases}, \tag{3.2}$$

with $j = d, m$ for either the metal or dielectric region. We have written no explicit x-dependence, as we assume the interface to be continuous along this axis. From Maxwell's equations we can obtain the equation for the electric field, $\mathbf{E}(\mathbf{r}, \omega)$[31]:

$$\nabla \times \nabla \times \mathbf{E}(\mathbf{r}, \omega) - \frac{\omega^2}{c^2}\epsilon_j(\omega)\mathbf{E}(\mathbf{r}, \omega) = 0, \tag{3.3}$$

with $\mathbf{r} = [x, y, z]$ a 3D-position vector. We are now looking for solutions of eqn. 3.3 along the metal/dielectric interface. To achieve this, we can essentially make a set of ansatzes about the form of the electric fields at either half of the interface, and then find the correct boundary conditions to unite the fields across the interface in $z = 0$.

---

[3] We will discuss their experiments in more detail later in this section.

The first ansatz we can make is that the surface plasmons should be confined to the interface, and as such should exponentially decay along the z-axis[4]. Secondly, the modes can propagate along the interface, i.e. the x-axis. As we want our surface mode to decay along the z-axis, we start by investigating strictly p-polarized waves ($\mathbf{E}$-field lying in the xz-plane). From this we can construct our plane wave electric field vector for either material half, j, as:

$$\mathbf{E}_j = \begin{pmatrix} E_{j,x} \\ 0 \\ E_{j,z} \end{pmatrix} \mathrm{e}^{ik_x x - i\omega t} \mathrm{e}^{ik_{j,z} z}. \tag{3.4}$$

We know that across the interface the x-component of the wave vector, k, is conserved, so:

$$k_x^2 + k_{j,z}^2 = \epsilon_j k^2 \tag{3.5}$$

Utilizing that the displacement field in either half of the material is divergence free ($\nabla \cdot \mathbf{D} = 0$), it is possible to write: $k_x E_{j,x} + k_{j,z} E_{j,z} = 0$, with which eqn. 3.4 can be rewritten as:

$$\mathbf{E}_j = E_{j,x} \begin{pmatrix} 1 \\ 0 \\ -k_x/k_{j,z} \end{pmatrix} \mathrm{e}^{ik_x x - i\omega t} \mathrm{e}^{ik_{j,z} z}. \tag{3.6}$$

From requiring continuity of the field components across the metal/dielectric interface, we can write:

$$\begin{aligned} E_{d,x} - E_{m,x} &= 0, \\ \epsilon_d E_{d,z} - \epsilon_m E_{m,z} &= 0. \end{aligned} \tag{3.7}$$

The above equations can now either be solved for $k_x = 0$, which is the trivial solution, or for:

$$\epsilon_d k_{m,z} - \epsilon_m k_{d,z} = 0. \tag{3.8}$$

Combined with eqn. 3.5, eqn. 3.8 gives us the dispersion relation for surface plasmon polaritons:

$$k_x^2 = \beta^2 = \frac{\epsilon_d \epsilon_m}{\epsilon_d + \epsilon_m} \frac{\omega^2}{c^2}, \tag{3.9}$$

with $k^2 = \omega^2/c^2$. In many contexts, k_x will also be referred to as the propagation constant of the plasmon, β.

---

[4] This kind of exponential surface confinement is seen for many other types of surface modes across physics.

On Fig. 3.3 a plot is shown of eqn. 3.9 for $\epsilon_d = 1$ and a Drude metal with different losses ($\gamma = 0; 4.5; 80\,\mathrm{THz}$). The dispersion of light ($\omega = ck$) in free-space is also shown. Two distinct branches are immediately apparent: A high energy branch to the left of the light-line, and a low energy branch to the right of the light-line. The high energy branch is not related to true surface modes, and is known as the Brewster mode. It is related to modes where $k_{m,z}$ is not purely imaginary, and thus allows the mode to propagate into the metal[31].

The low energy branch however relates to true propagating surface modes. It is worth noting that the low energy branch is solidly to the right of the dispersion of light. This means that surface plasmons have larger wave vectors, and i.e. shorter wavelengths than free space light ($\lambda_{spp} = 2\pi/\beta$). Surface plasmon polaritons are thus a way to confine light below its normal free-space mode volume. Without accounting for losses, the lower energy branch just continues off asymptotically, but once losses are introduced a kind of 'back bending' will occur where the Brewster and surface plasmon modes become linked. Essentially, this sets a limit for how confined the plasmon can be at the surface of the metal[31]. We see for increasing losses, that this 'back bending' happens earlier. We can see from this that the losses in metals intrinsically limits their plasmonic properties[52].

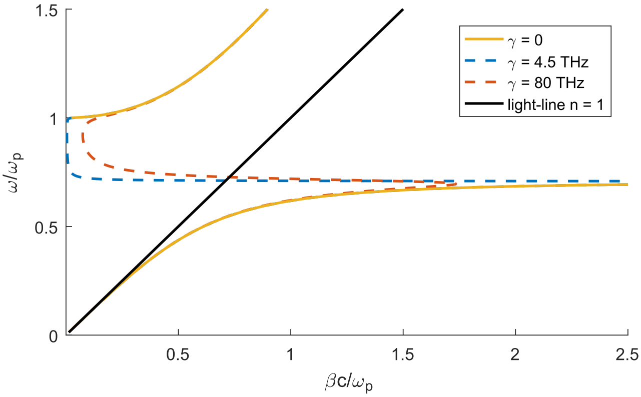

Figure 3.3: Dispersion relation for surface plasmons between a metal and air interface. The dispersion of light is also plotted, showing the momentum mismatch between surface plasmon polaritons and free-space light. For increasing losses in the metal, earlier linking of the high energy Brewster mode to the surface plasmon is observed.

Another consequence of the plasmon dispersion being to the right of the light-line, is that free-space light does not carry sufficient momentum on its own to excite the plasma oscillations. We can rectify this limitation in various ways, such as scattering the light off of a grating or other surface structure to confer an additional in-plane wave vector component, excite the plasmons by evanescent near-fields (more on this later), or even excite the surface plasmons by an electron beam (see chapter 7).

One way to achieve an evanescent field for plasmon excitation is through total internal reflection in a prism. If light in the prism at an angle of θ is reflected at the prism's facet (and θ is greater than the critical angle), no propagating component of the light will be transmitted and the light is totally reflected. However, it can be shown that an evanescent field will emerge on the other side of the prism's facet[53]. Due to the requirement of continuity of the fields across the interface, the in-plane component of this evanescent wave must then be:

$$k_x = k\sqrt{\epsilon_d}\sin\theta, \tag{3.10}$$

with k the free space wave vector and ϵ_d the dielectric constant for the prism. From eqn. 3.10 we see that we should expect a strong angle dependence for the plasmon coupling, as by changing the angle we can directly tune the size of the k_x/β of the light we are trying to couple to the plasmon. Likewise, we see that the refractive index ($n_d = \sqrt{\epsilon_d}$) of the prism material is important, as higher refractive indices will allow for larger in-plane wave vectors for a lower input angle.

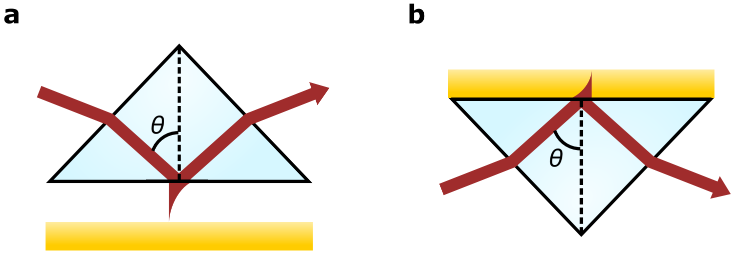

Figure 3.4: Coupling to surface plasmon polaritons in a metal film by evanescent fields from a prism, in the **(a)** Otto- and **(b)** Kretschmann configuration.

Two configurations for prism coupling exists, following the experiments by A. Otto, E. Kretschmann and H. Raether in 1968[31, 34]. They can be seen on Fig. 3.4. The Otto-configuration[50] has a small air-gap between the metal film and the prism, and relies on the 'tunneling' of the photons through the air to couple to the plasmons. This is very reminiscent of the way an optical fiber can be used for plasmon excitation and measurement in a scanning near-field optical microscope (we will discuss such devices in more detail in chapter 6).

The Kretschmann-configuration[51] instead has no air-gap, and the film is deposited directly onto the prism. For both configurations the plasmon will be observed as a strong drop in the recorded reflectivity of the input laser beam, as energy is lost in the plasmon excitation. For sensitive samples where the surface should not be touched directly the Otto-configuration is preferred. However, the Kretschmann-configuration is generally more commonly used, as it is easier to implement in practice[34]. It is worth noting that using a prism to couple light into the plasmon, equally allows for the light to couple out again. As such, a higher degree of radiative losses are associated with prism coupled plasmons. This can be exploited for imaging of plasmons in so-called leakage radiation microscopy[34].

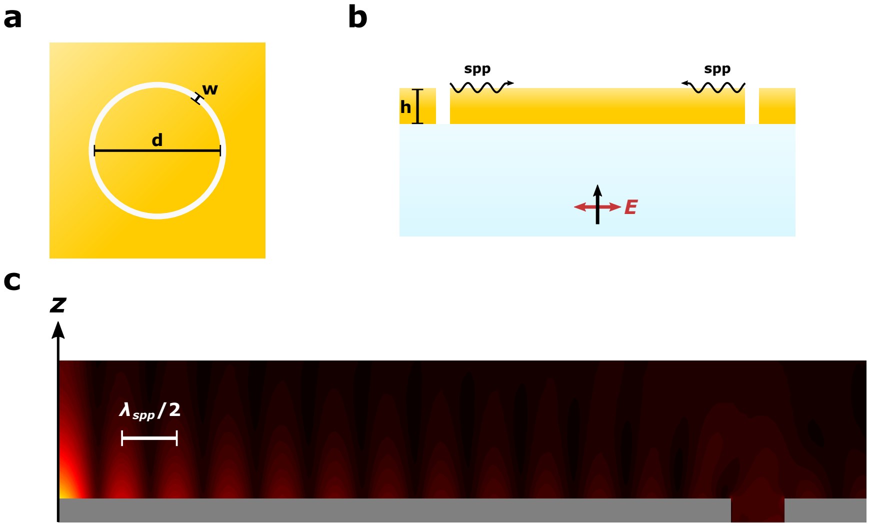

Figure 3.5: (a) Top view of the plasmonic lens geometry, defining diameter $d = 16\,\mu\text{m}$ and slit width, $w = 300\,\text{nm}$. **(b)** Profile view of the lens, defining the metal film thickness, $h = 150\,\text{nm}$ as well as showing the glass substrate and how the lens is illuminated from below by a 633 nm plane wave. **(c)** $|\mathbf{E}|^2$ plotted for half of the plasmonic lens. The geometry is rotationally symmetric around the z-axis. Unpublished.

Another common technique to couple external light to plasmon polaritons (or manipulate their propagation) is by scattering from a grating. This technique is especially convenient for on-chip plasmonics and waveguiding applications[34, 54–58]. In a similar fashion, even a simple slit in a metal film can be used to excite plasmon polaritons[59]. This has been exploited for focusing applications in plasmonic lenses[55, 60, 61]. By milling a circular slit in a thin metal film, plasmon polaritons will be launched towards the centre of the circle from all directions, creating a focused spot of field enhancement. Because each point of the circle also has an opposite point launching similar plasmons, an interference pattern of constructive/destructive interference will be observed as concentric circles. The period of these interference fringes will be $\lambda_{spp}/2$. Fig. 3.5 shows the geometry and a cross section of a simulation of the excited fields for such a lens with a diameter of 16 µm. The evanescent nature of the fields is clearly visible in Fig. 3.5.c, as the field intensity rapidly decays with distance from the metal film. The fields were obtained by a finite element simulation performed with COMSOL Multiphysics 4.4, with gold's dielectric function modelled using values from reference [41]. From a rough estimate, using eqn. 3.9: $\lambda_{spp}/2 \simeq 300\,\text{nm}$, which fits the scale in Fig. 3.5 very well.

3.2.1 Localized surface plasmons

We have discussed the two cases for when light interacts with macroscale metal structures, but in this final section we will deal with the special case of exciting plasmons in sub-wavelength metal structures[5]. Limiting the physical size of the particle in which the plasmon is excited allows for further confinement of the plasmon, resulting in localized surface plasmons.

If we consider the case of a metal sphere of radius, r, which is significantly smaller than the exciting wavelength, and also smaller than the skin depth in the material it is made from, δ (see chapter 2). What will then occur upon illumination, is that the external field will fully penetrate into the sphere and uniformly perturb the sphere's electron plasma. Similar to the case for the bulk plasmon, this will then cause a collective oscillation of the electrons. However, in this case we can specifically drive the oscillation with the frequency of light used, ω, and the limited size of the metal particle will help determine the resonance frequency of the surface plasmon.

An analogy to this could be the vibrations in a fixed string, where the length of the string plays a critical role in its fundamental vibration modes. In a more generalized description of localized surface modes, we can relax the criteria of the structures being of similar size to the skin depth and still get similar results[34]. The general point however remains: For localized surface plasmons, we do not need any momentum matching to couple to external light, but the structures will also only have a strong plasmonic response when we illuminate them with a wavelength of light sufficiently close to the eigenmodes of the specific geometry. The left-hand side of Fig. 3.6 shows a simple dipole resonance for a metal sphere.

We can now also consider what happens if we take two such spheres and put them within a short distance of each other. As the two particles approach each other, eventually their plasmon modes will start to influence each other and hybridize into a coupled gap mode for the particle pair. We can expect two cases, one where both spheres' plasmon oscillate in the same phase, or the other case where they oscillate out of phase. We refer to the in phase plasmons as a 'bonding' mode, and the out of phase as an 'anti-bonding' mode, due to the similarity to hybridization seen in molecular bonding[62].

---

[5] For visible light this being the nanoscale.

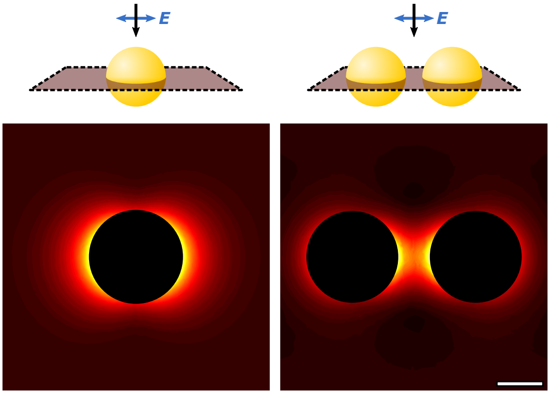

Figure 3.6: Excitation of plasmons in metal nanospheres from plane wave illumination. $|\mathbf{E}|^2$ is plotted from the highlighted planes. The left images show a simple dipole resonance for a single sphere, aligned with the polarization of the exciting light. The right images show a gap plasmon between two such spheres. The scale bar is 40 nm. Simulations performed by T. Repän.

For the bonding mode, its resonance energy will tend to redshift the closer we move the two particles, while for the anti-bonding mode its energy will blueshift. Generally the anti-bonding mode is considered a 'dark' plasmon mode, as it is difficult to excite by light due to the geometry (as the structure is sub-wavelength, it will be uniformly engulfed in the electric field of the light, favouring in-phase oscillations[62]).

Localizing the excitation mode in the smaller gap between two structures generally leads to a smaller mode volume for the plasmon, which allows for a higher degree of electric field enhancement and localization, as well as a greater degree of fine-tuning of resonance frequency[63, 64]. This is especially exploited for applications in various optical antenna geometries[63, 64]. See right-hand side of Fig. 3.6 for a gap plasmon mode between two metal nanospheres.

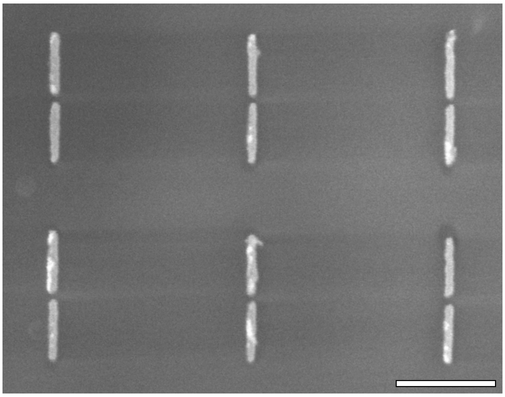

Figure 3.7: SEM-image of plasmonic gap antennas made with EBL. 40 nm gold with 10 nm titanium adhesion layer on a glass substrate. Scale bar is 500 nm. Unpublished.

For practical applications, nanoantennas will typically be defined using electron-beam lithography (EBL). Fig. 3.7 shows an example of an array of gap antennas fabricated during my studies in collaboration with N. Stenger. By varying the length of the individual rods making up the gap, it is possible to change their individual plasmon resonance, and as such change the hybridized gap plasmon as well[64].

4 Metal percolation films

As we have discussed previously, metals are able to host collective electron excitations known as plasmons. These excitations can in the right circumstances couple to external electrical fields, such as light. We also touched on the fact that structuring metal at the nanoscale changes the available modes of excitation. In this chapter, we will look at an example of self-organized random nanostructures in metals, achieved by a simple one-step fabrication process. These structures are known as metal percolation films[1].

4.1 Percolation theory

Perhaps an ideal place to start our discussion is with the mathematical discipline of percolation theory, where many of the concepts and terminology originates. The verb "percolate" refers to the windy and tortuous path a liquid will take as it passes through a porous medium (a well-known example for most people being hot water passed through coffee grounds to brew coffee in a regular drip coffee maker). Percolation theory thus deals with this kind of random motion/growth of a system, where at each time interval the system can branch/evolve randomly in a direction, based on the points it has already reached[65]. This results in a system of initially isolated self-similar structures, which will experience dramatic changes in properties at the point of percolation (when the system becomes dominated by one connected region[65]).

---

[1] Also often referred to as semi-continuous metal films, or metal/dielectric composite films.

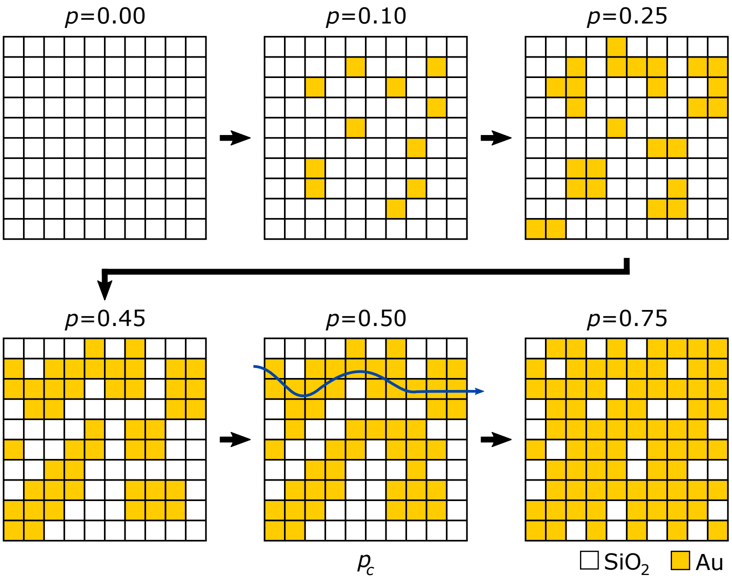

Figure 4.1: Simple top-view cartoon of the growth process of a gold film on a SiO_2 substrate during constant metal deposition. A potential route from left to right is marked in the fifth frame were the system has reached its percolation threshold, p_c, and becomes connected.

There are multiple ways to describe and define percolation systems (as indeed many different types of systems also exists.)[19, 65]. We will here limit our attention to what is typically referred to as 'site percolation' in a 2D geometry. An example of such a system is shown on Fig. 4.1. The system consists of a 2D lattice of either vacant (SiO_2 substrate) or occupied (Au) 'sites'. As time progresses more and more lattice elements become occupied, and the result is isolated clusters that eventually 'percolate' together, forming a connected system. we can for each frame designate a probability p of a site being occupied, and a probability $1 - p$ of a site being unoccupied. In the fifth frame the system reaches its percolation threshold ($p = p_c$), and an electrical current could be passed from the left to the right of the lattice through the connected gold elements. As a straight path is not available, the resistivity of the percolation film will generally be a lot larger than for a fully formed film[2]. As additional material is deposited the resistivity will also decrease as a more and more straight path becomes available. The percolation threshold thus marks a phase transition of the system as a whole, as it marks the point where the collective film goes from being an insulator to a conductor[3].

---

[2] In our Drude model terms from chapter 2: A longer path in the metal means more scattering events, which limits conductivity.

This style of growth pattern is observed in many self-assembled structures[19], and overall results in a high degree of self-similarity. This means that a small subset of the structure is representative of the whole, even across different size scales[19].

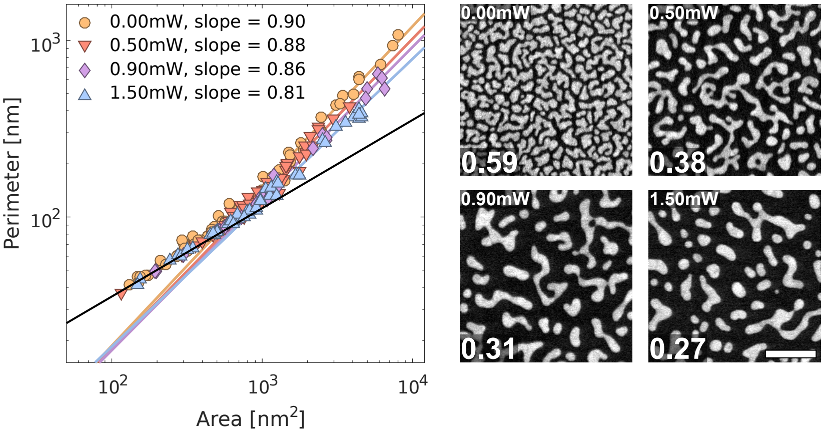

Figure 4.2: Perimeter vs. area plot of four 5 nm gold percolation film morphologies. The solid black line is the theoretical expression for perfectly circular particles. STEM dark-field images of the samples are labelled with the laser power used to alter the morphology in the top left corner, and in the bottom left the filling fraction of gold in the image is noted. The scale bar is 150 nm, all images at same scale.

A simple way to see the self-similar/fractal nature of the 2D percolation geometry is in a perimeter vs. area plot of its constituent particles. On Fig. 4.2 four different morphologies can be seen: A pristine 5 nm percolation film, and three examples of morphologies obtained by partially melting similar films with three different laser powers. By recording scanning transmission electron microscope (STEM) dark-field images of the morphologies, it is possible to gain high quality greyscale images of the sample structures. From these we can extract the perimeter and areas of each particle present in the image. If we plot the perimeter vs. particle area of each particle in the images, we get the set of curves on the log-log plot in the left of Fig. 4.2. The fact that the points fall on a straight line in the log-log plot indicates that the perimeter/area ratio (P/A) of the particles is preserved across size scales (with the ratio given by the slope of the linear fit). For the case of perfectly circular particles of random sizes, we would expect the black curve with slope 0.5 also shown in Fig. 4.2. As expected the P/A-ratio decreases for the samples that have been partially melted, as more and more of the particles contract to more spherical shapes for higher laser powers. The scale invariance of the P/A-ratio is a strong indicator of self-similarity, and a common feature of fractal systems[19]. We will see in a later section how this fractal/self-similar morphology of the films plays a large impact in their optical properties, and in later chapters we will also see how the percolation threshold is critical for maximizing plasmonic field enhancement in these kinds of films.

---

[3] The individual clusters that make up the film before percolation are of course still conductive, the percolation threshold simply marks the transition from isolated to connected clusters.

4.2 Fabrication

The gold percolation films studied here have all been fabricated by metal evaporation onto a dielectric substrate, using an electron-beam physical vapor deposition (e-beam) system in the cleanroom facilities at DTU Danchip. We will here discuss the physics responsible for the nanostructuring that happens inherently during this kind of deposition, as well as how metal evaporation is achieved and controlled in an e-beam set-up.

4.2.1 The Volmer-Weber growth process

When evaporating metals onto a substrate for thin film growth, we are dealing with a phase transition of gas/liquid phase metal atoms to a solid phase metal film on the substrate material. We refer to the first stable points where the metal atoms can coalesce together into a solid as nucleation sites[25]. These points are where the metal atoms have a higher probability of growing in time during deposition, rather than dissociate. The substrate temperature and evaporation temperature at the metal source will naturally influence the required size for such a nucleation site to be stable, as more energetic atoms will require larger clusters to become stably bound[25]. During a deposition the gas phase atoms will adsorb unto the substrate material. Here they thermalize with the substrate, and start to diffuse on it. During diffusion they will either dissociate back into the gas phase, or form nucleation sites/bond to nucleation sites. A schematic picture of the different processes that can occur when the gas phase atoms hit the substrate material can be seen on Fig. 4.3.

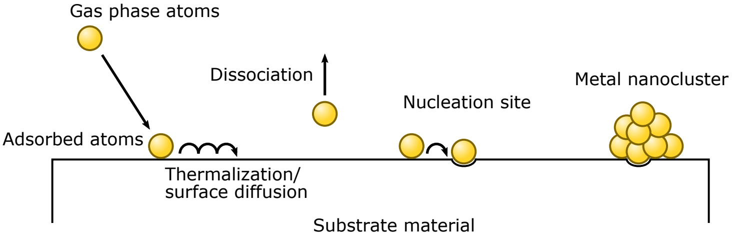

Figure 4.3: Microscale schematic of the deposition process. Gas phase atoms adsorb on the substrate surface, and then thermalize/diffuse until they either dissociate back into the gas phase, or bond to a point of lower potential on the substrate, or another metal atom.

In the case of metal deposition onto a dielectric substrate, the metal atoms will have a much stronger mutual bonding than to the substrate. This means that the metal atoms as they are deposited onto the substrate are more likely to attach to already existing metal clusters than to form new nucleation sites. This type of film growth is referred to as 3D-island or Volmer-Weber growth. In the case of equally strong interaction between the deposited material and the substrate, the atoms will instead quickly form flat layers, leading to 2D-layer or Frank–van der Merwe growth. An example of 2D-growth could be metal on metal deposition. Finally, a third kind of growth exists that is a mix of 2D-layer and 3D-island growth, called Stranski-Krastanow growth. Here the deposition initially results in 2D-layers, but due to a lattice mismatch between substrate and deposited material eventually the strain and energy cost associated with additional 2D-layers becomes too great. This results in 3D-islands forming on top of the 2D-layer, typically after 1-3 monolayers. An example of Stranski-Krastanow growth is Ge/Si(001), where germanium quantum dots can be grown on a silicon (001) surface simply from the ~4% mismatch in lattice constants between Ge and Si(001)[25, 66, 67].

If we reconsider the Volmer-Weber process, we can understand how a percolation film will naturally self-organize. As the initial metal clusters grow during continuous metal deposition, they will eventually become connected in increasingly larger and larger structures, that also become more twisted and tortuous due to the randomness of where additional material is added. Eventually the film will reach a percolation threshold where it becomes possible to find a fully connected path through the system. For additional deposition after this point, the film will slowly become more and more interconnected until it forms a rough fully connected film with large holes/gaps in it. Further deposition will close the film together completely, and the growth will shift to a 2D layer by layer growth, as the gold is now being deposited onto a gold film, with more or less equal likelihood of bonding to any point[25, 68].

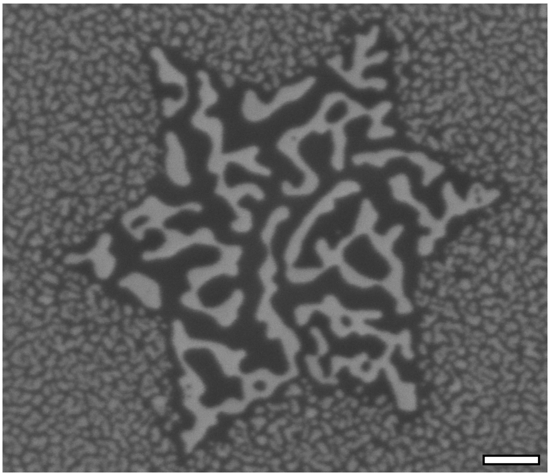

Figure 4.4: SEM-image of a multi-pointed MoS_2 monolayer flake on a SiO_2/Si-substrate. 4 nm of gold has been deposited. Scale bar is 250 nm.

An example of the strong influence of substrate material for film growth can be seen on Fig. 4.4. Here we see an electron micrograph of a monolayer[4] MoS_2 flake with 4 nm gold deposited. It is very clear that the gold structures formed on top of the flake differ drastically from the ones on the surrounding SiO_2/Si-substrate. The reason for this can be explained by the surface energy between gold and MoS_2 versus that of gold and silicon. The stronger interaction between gold and MoS_2 allows for much more efficient nucleation and film growth, resulting in bigger clusters at the same deposition thickness.

4.2.2 E-beam metal deposition

One method of metal deposition is that of electron beam (e-beam) evaporation. A high energy beam of electrons is used to heat part of a metal ingot enough to evaporate atoms off of it. As only a small part of the ingot is evaporated, it is possible to conserve deposition material, and the evaporated material is also projected into a directional jet of gas phase atoms[68].

---

[4] MoS_2 is an indirect band gap semiconductor, but transitions to a direct band gap for monolayers[69]

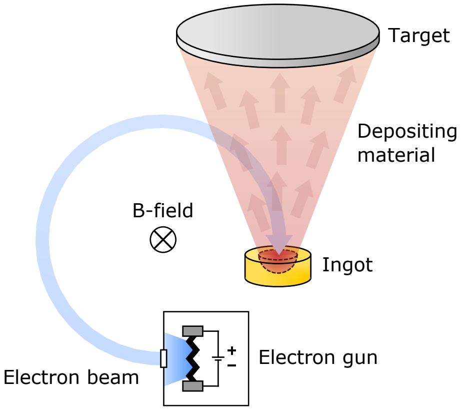

Figure 4.5: Cartoon of the e-beam evaporation and deposition process. In a high-vacuum chamber, an electron gun generates a high current of electrons that are diverted into a metal ingot by a magnetic field. The kinetic energy of the electrons locally heat the ingot and cause a section of it to evaporate, creating a directed jet of metal atoms towards a target.

The electron beam is typically generated by a tungsten[5] filament that is Ohmically heated by applying a large voltage to it. By heating the filament enough the electrons in it eventually receive enough kinetic energy that they are able to escape to the vacuum level. At this point the filament will eject electrons in many different directions, and a pinhole is usually placed in front of it to limit the angular distribution of electrons. The beam passing the pinhole is thus relatively collimated and can be accelerated by electric fields and directed by magnetic fields. As an electron beam cannot propagate in air (due to collisions with the air molecules), the entire deposition process has to happen in high-vacuum[6]. As low air-pressure is generally desired for the deposition process to be more uniform and well-controlled, this is not a major disadvantage to the e-beam method. As both the amount of electrons and their energy can be controlled well electrically in the system, it is possible to vary the deposition rate across a broad range of values, and likewise it is possible to evaporate many different materials, despite their differences in melting point[68].

During a deposition process, a series of steps will be performed before the actual material deposition. This is to ensure consistent material evaporation during the process, removing any potential contaminants from the source material surface, and also to protect the source metal ingot and maximize its lifetime. Before actual deposition, the source ingot will first go through a soaking process where it is slowly raised to temperature by scanning the e-beam across it. This helps ensure a uniform evaporation from the ingot, and by letting the initial outer layers evaporate with the shutter between the ingot and target staying closed, any surface contaminants on the source ingot can be removed without contaminating the target substrate.

---

[5] Tungsten is used due to its exceptionally high melting point of ~3400 °C

[6] Pressures of about ~10^{-4}-10^{-8} torr.

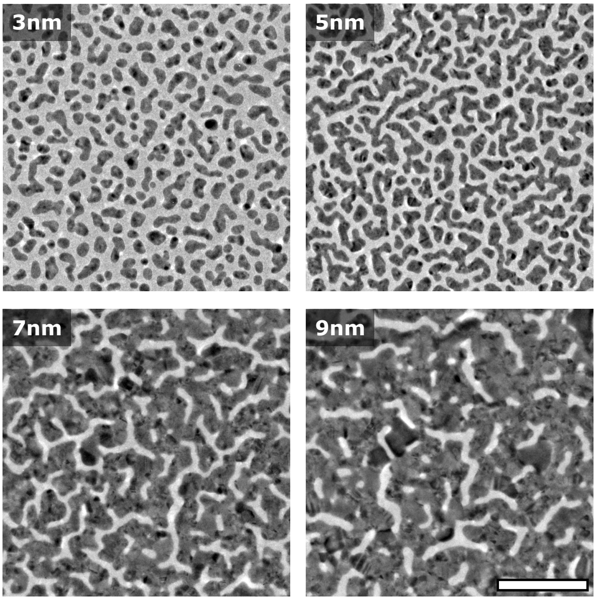

Figure 4.6: TEM-images of four different gold morphologies achieved by varying the deposition time at a constant deposition rate of 2 Å/s. The listed thickness is the total deposited amount, which is not necessarily the actual thickness of the clusters. The dark contrast is gold, the lighter substrate is SiO_2. Scale bar is 50 nm, all images at same scale.

The samples investigated in this thesis were all fabricated by maintaining a constant gold deposition rate of 2.0 Å/s (within experimental limits of roughly ±0.1 Å/s). High-resolution transmission electron microscope (TEM) images of four different film morphologies achieved by varying the deposition time can be seen on Fig. 4.6. The contrast in the TEM-images also offers us some additional insight into the structure of the gold films, as the contrast is somewhat proportional to the thickness of the material (thicker material appears darker). From this we can see that the majority of the film is actually of a similar thickness, with the exception of sparsely distributed 'grains' of significantly darker contrast. For the thicker sample depositions these grains also seem to grow significantly in size, while the surrounding film uniformly seems to become thicker. Essentially, what we are seeing here is the initial nucleation sites of the film deposition, slowly growing into larger and larger crystal domains of what will eventually become a highly polycrystalline/amorphous gold film if depositing beyond the 9 nm case.

4.3 Optical properties

The optical properties of metal percolation films (and random media in general), has already been studied in detail[19, 70]. We will here try to summarize some of these results, and also discuss how the fractal and self similar morphology of metal percolation films naturally results in very broadband optical properties.

4.3.1 Theoretical approaches

An obvious first approach to treat the optical properties of semi-continuous media in general is that of effective-medium and mean-field theories[19, 71]. Such approaches are able to predict the linear properties of semi-continuous media quite well[19]. However, because such models do not account for the exact local field distributions in the structures, they miss out on some of the crucial phenomena[19].

Several models have been developed to calculate the exact optical response of random metal clusters when illuminated with external radiation[26–28, 72, 73]. We will here focus on the theoretical model as outlined in references [19, 73–77]. The premise is quite straight-forward: We consider a lattice of $L \times L$ elements in x, y-coordinates. Each site member then consists either of a dielectric or metal element. External radiation is directed perpendicular to the xy-plane (along the z-axis), and each lattice element is much smaller than the wavelength of the light exciting the structure[7]. We model the metal's dielectric function as a Drude metal (see chapter 2), and the dielectric as the constant ϵ_d. For treating the film's response to an external field, $\mathbf{E}_0(\mathbf{r})$, we consider the local AC conductivity of the system, $\sigma(\mathbf{r})$. For metal elements this becomes $\sigma_m = -i\omega\epsilon_0(\epsilon_m - 1)$ and for dielectric elements it is $\sigma_d = -i\omega\epsilon_0(\epsilon_d - 1)$. We can now express the total electric field in terms of the local potential, $\phi(\mathbf{r})$, and the external field:

$$\mathbf{E}(\mathbf{r}) = -\nabla\phi(\mathbf{r}) + \mathbf{E}_0(\mathbf{r}). \tag{4.1}$$

---

[7] I.e. we can neglect field variation across the structures, also known as the quasistatic approximation.

The local current, $\mathbf{j}(\mathbf{r})$, is given by Ohm's law[8], so we can write:

$$\mathbf{j}(\mathbf{r}) = \sigma(\mathbf{r})\left[-\nabla\phi(\mathbf{r}) + \mathbf{E}_0\right]. \tag{4.2}$$

From current conservation, $\nabla \cdot \mathbf{j}(\mathbf{r}) = 0$, we finally get the Laplace equation for the local potential:

$$\nabla \cdot \left(\sigma(\mathbf{r})\left[-\nabla\phi(\mathbf{r}) + \mathbf{E}_0\right]\right) = 0. \tag{4.3}$$

To solve eq. 4.3, we can regard the conductivity between the bonds of our lattice elements. For the i'th site this becomes:

$$\sum_j \sigma_{ij}(\phi_i - \phi_j + E_{ij}) = 0, \tag{4.4}$$

where the summation over j is for the 4-point connected nearest neighbours to lattice site i (i.e., $j = i-1, i+1, i+L, i-L$). σ_{ij} is the conductivity between site i and j, given as $\sigma_{ij} = 2\sigma_i\sigma_j/(\sigma_i + \sigma_j)$. E_{ij} is the electromotive force between sites i and j. If a is the physical size of each lattice element, and the external radiation is y-polarized, we can define $E_{ij} = \pm aE_0$, for bonds in the $\pm y$-directions, respectively, and bonds along the x-direction $E_{ij} = 0$ (for x-polarized light, this would just be reversed).

Eq. 4.4 is essentially a Kirchoff equation, and we can use a matrix representation for the full set of equations of the system:

$$\hat{H}\mathbf{\Phi} = \mathbf{F}, \tag{4.5}$$

where $\hat{H}$ is the $L^2 \times L^2$ sparse block matrix Kirchoff Hamiltonian of the system. It has diagonal elements $\hat{H}_{ii} = \sum_j \sigma_{ij}$ (the summation here is like eq. 4.4) and off-diagonal elements $\hat{H}_{ij} = -\sigma_{ij}$. $\mathbf{\Phi} = [\phi_i]$ and $\mathbf{F} = [-\sum_j \sigma_{ij}E_{ij}]$ are simply two L^2-length column vectors.

By solving eq. 4.5 for $\mathbf{\Phi}$, it is possible to get the explicit local electric field distribution for a given percolation film geometry[9]. Eq. 4.5 can be solved with periodic boundary conditions – i.e. the first row of lattice sites are connected to the last row, and the first column is connected to the last column. However, when opting for such boundary conditions, the system of equations represented by eq. 4.5 becomes inconsistent, as one of the equations will become linearly dependent on the others. This can be rectified by 'grounding' one of the lattice sites[28] (for example, the corner $i, j = 1, 1$). In practice, this is achieved by simply assuming its potential $\phi_i = 0$, and removing the corresponding row i and column j from $\hat{H}$, and rows i from $\mathbf{\Phi}$ and $\mathbf{F}$ when doing the calculation.

---

[8] $\mathbf{j}(\mathbf{r}) = \sigma(\mathbf{r})\mathbf{E}(\mathbf{r})$

[9] The actual direct solving of eq. 4.5 is incredibly computationally intensive, and a block elimination method is normally used[28, 78]. Alternatively, the sparse nature of $\hat{H}$ allows for sparse matrix numerical methods, greatly reducing computational requirements.

Fig. 4.7 shows the local field intensities $I(x, y)$ and squared intensities $I^2(x, y)$ for silver percolation films at three different excitation wavelengths, obtained from solving eq. 4.5 in reference [28]. From these distributions we clearly see that the optical response of the film is dominated by very intense plasmonic 'hotspots'. We also see that these spots are strongly localized to small regions of the film, and that the spatial distributions of the hotspots vary for different excitation wavelengths. Finally, we see that the excitations from longer wavelengths of light also have a larger general intensity than for shorter wavelengths. The localization of the plasmonic hotspots is often attributed to the fact that fractal or chaotic systems, like percolation films, lack translation symmetry. Thus they do not support propagating waves[29] (the most extreme case of this being potential Anderson localization[79]). The fact that several different resonance energies are supported can likewise be attributed to the fractal/self-similar geometry. The localized plasmon resonance of a metallic structure strongly depends on its size, and as the percolation films have similar shaped metal structures at different size scales, we likewise expect them to have plasmon resonances across different energies.

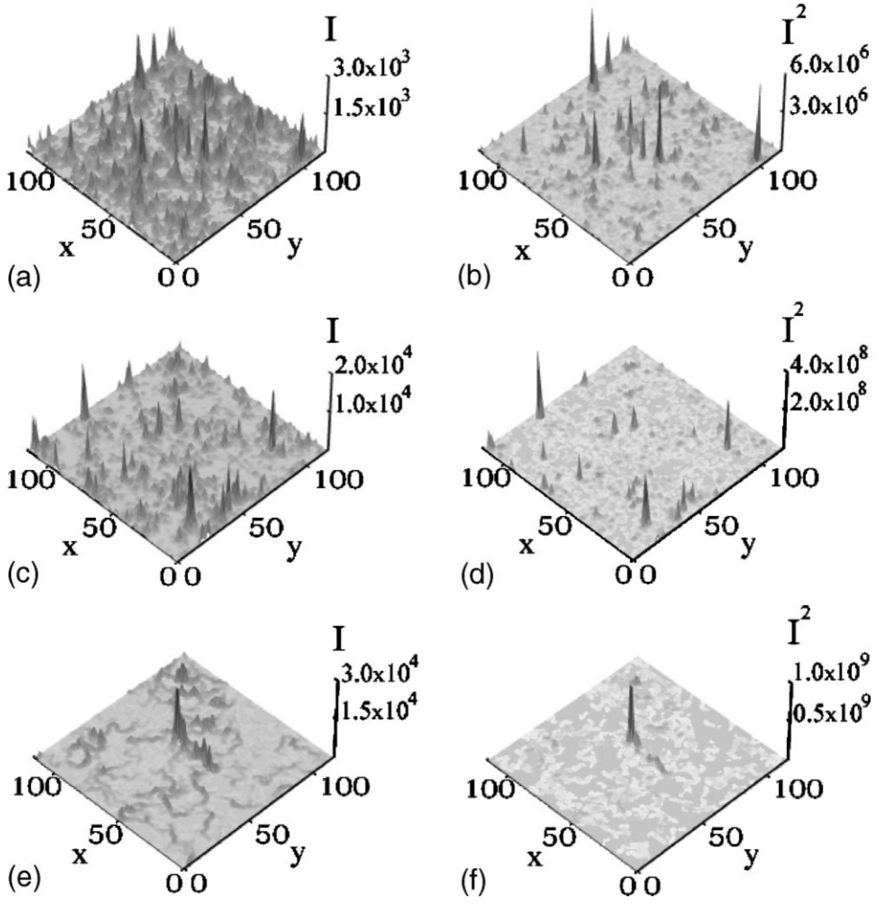

Figure 4.7: The spatial distributions for the normalized local intensity $I(x, y)$ and for the non-linear intensity $I^2(x, y)$ for silver on glass percolation films. The distributions are calculated for three different wavelengths: **(a-b)** $\lambda = 0.370\,\mu\text{m}$, **(c-d)** $\lambda = 1\,\mu\text{m}$, and **(e-d)** $\lambda = 5\,\mu\text{m}$. The metal filling factor is chosen as $p = p_c$ for all cases. Reproduced from reference [28].

4.3.2 Experimental investigations

We will here highlight some of our own experimental results for near-field measurements of gold percolation films, performed with electron-energy loss spectroscopy[10]. On Fig. 4.8 are a set of examples of how the plasmons in a 5 nm gold film can be spatially visualized by integrating the EELS data over various energy ranges[80] and overlaying this on the sample morphology also recorded in the scanning transmission microscope (STEM).

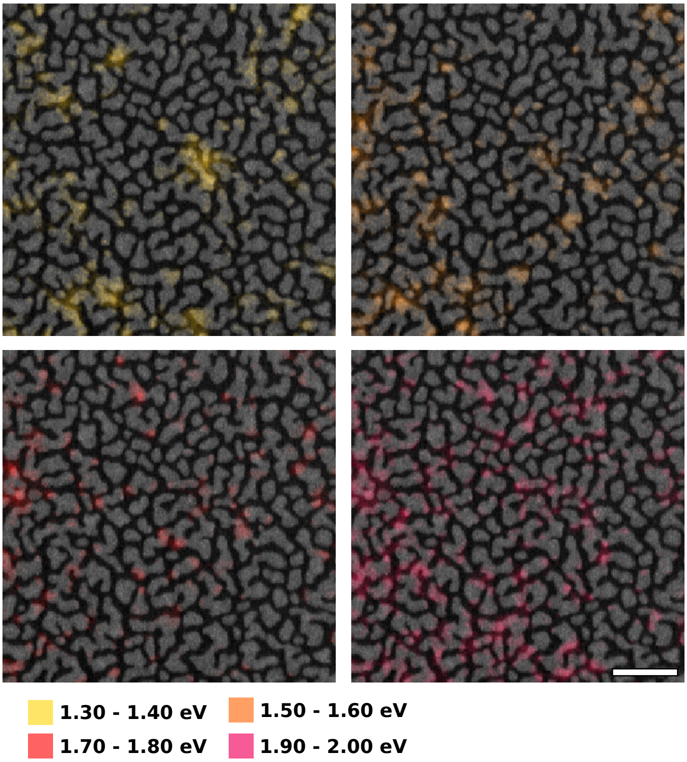

Figure 4.8: STEM dark-field images of the 5 nm thin film gold sample with integrated EELS maps projected on top. The background corrected EELS data were integrated in different energy ranges to produce intensity maps of the recorded EELS signal. The coloured parts of the images generally show between 5-15 times as high EELS signal as the rest of the image. Scale bar is 100 nm.

---

[10] See chapter 7 for an explanation of the method and equipment.

From the images we see that the local field distribution in the gold film varies quite considerably for different energy ranges. For example, we see that the higher energy plasmons are typically quite well localized on the surface of the gold, while the lower energy modes can in some cases extend fairly significantly. In general, several hot spots are apparent where the local intensity is significantly larger than the immediate surrounding areas. We also see that the apparent position of these hot spots is not related to the geometry of the film in a simple way, as many similar looking regions appear dark in the EELS measurement, while others show large EELS intensity signal. This is in agreement with similar measurements for silver films, see reference [81].

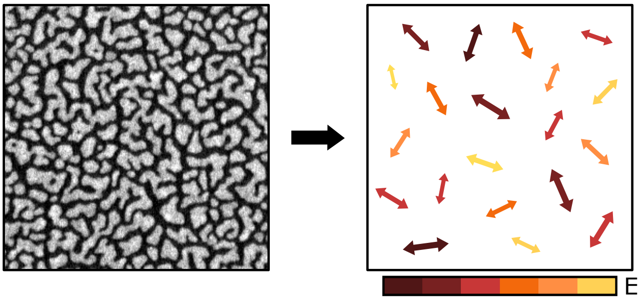

Figure 4.9: The complex geometry of the percolation film results in various plasmonic hotspots at different resonance energies and with different polarizations. We can thus think of an equivalent model for the percolation film that consists of a random distribution of linearly polarized plasmon resonances. We here represent these hotspots as double arrows aligned with their polarization. The size of the arrows indicates their relative field intensity, and the colours represents their resonance energy.

Because of the random nature of their morphologies, the specific detailed spatial distribution of plasmon resonances can be difficult to reproduce and compare across percolation film samples. As a result, direct qualitative maps of the plasmons like in Fig. 4.8 best serve to give us a general impression of how the plasmons are distributed. Making detailed comparisons between several EELS maps like in Fig. 4.8 at different energies also quickly becomes very overwhelming to interpret. Lastly, the fact that many of the films' optical properties are dominated by strongly localized plasmonic hotspots[19, 26, 28, 82] allows us to make an equivalent model of the films based on their local properties[83].

Fig. 4.9 shows a schematic of how a complex gold percolation geometry can be thought of equivalently as a random distribution of plasmonic hotspots with random polarizations[11] and resonance energies. Such a random distribution of plasmonic hotspots can more or less be fully described in a purely quantitative statistical framework. Because the sizes of the particles and gaps in our images are all several orders of magnitude smaller than the investigated regions ($500\times500\,\mathrm{nm}^2$), we assume that our EELS maps are recorded at the size scale where the films can be considered isotropic. In other words: Our measured regions, while only a small subset of the entire sample, are large enough that any probabilistic conclusions we draw from them can be said to apply to the films as a whole, due to their isotropy.

To make a statistical description of our samples, we take advantage of the methods of previous theoretical and experimental works on self-similar and fractal structures[28, 78, 82, 84]. We can extract two parameters that describe the plasmon resonances in our EELS maps: The central position of the plasmon peak in the EELS data, and the amplitude of the resonances (its EELS intensity). We achieve this by a series of sequential Gaussian fits, that progressively become more and more detailed (full method in chapter 7). After having identified the plasmon resonance energies and their intensities, we can now perform two rather simple treatments. First, a histogram can be constructed of the different resonances energies to show how the plasmons are distributed in terms of their energy in the sample. Secondly, we can construct a probability density function (PDF) of the EELS intensities of the plasmons. By then binning the intensities, for a certain range of resonance energies, we form a distribution of intensities in the spectral image (i.e. a histogram). We then normalize this histogram with the total amount of resonances detected to get a probability. By breaking this PDF analysis down by energy ranges, we can sort out which part of the energy spectrum that provides the largest EELS intensities in the percolation film (right-most points of the PDFs), and by that token which energy range would have the largest field enhancement.

---

[11] We will show the polarization dependence explicitly in chapter 6.

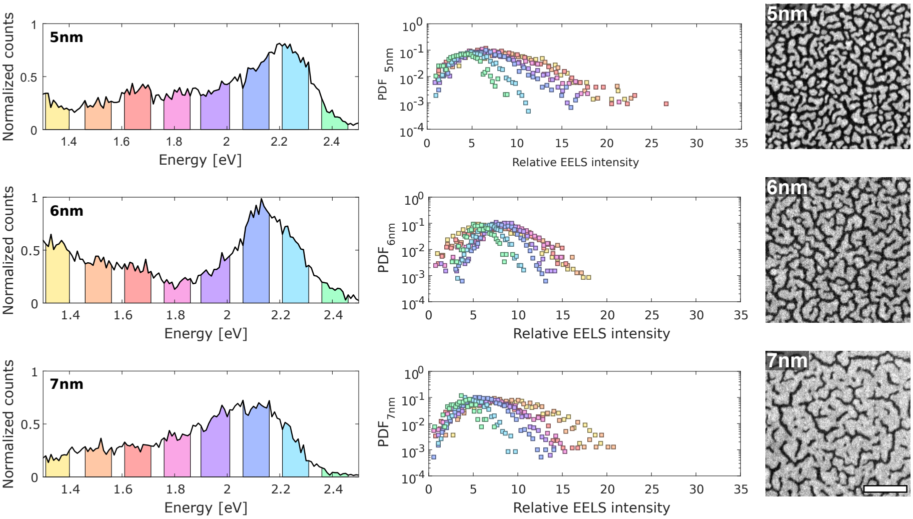

Figure 4.10: Quantitative analysis of the spectral images recorded from three different percolation film thicknesses: 5, 6, and 7 nm. The left row shows histograms for how the plasmon resonances are distributed in terms of energy. The centre column shows constructed PDFs of how the EELS intensity is divided inside subset energy ranges identified with the colours in the resonance histograms on the left. On the right is shown a STEM dark-field image of the sample morphology. Scale bar is 150 nm.

Fig. 4.10 shows the results of such an analysis carried out on 5, 6, and 7 nm gold samples. In the left column simple histograms are plotted showing the distribution in central peak energies for the plasmon modes identified. From these we can see a general peak in the amount of resonances near 2.1-2.2 eV. For increasing deposition thickness this peak shifts towards lower energies. The centre column of Fig. 4.8 shows PDFs of the relative EELS intensities for these plasmons, based on taking data from the highlighted coloured energy ranges in the histograms. The EELS intensities are normalized to the median of the 50 lowest intensities seen in the individual maps, to get a relative measure of how much larger some resonances might be than others. From these PDFs we are able to see that across all three samples, the highest intensities are found in the lower energy ranges 1.3-1.7 eV. This is also in agreement with prior work[19, 30, 73–77].

5 Photoluminescence in gold

The ability of noble metals to emit light after initial optical excitation has been an active area of study for the last several decades. Despite this, the underlying physical mechanisms are still poorly understood for some systems[85–87].

Metallic photoluminescence was first addressed by A. Mooradian in 1969[88]. In this initial publication, Mooradian showed that it was possible to get a spectrum of photoluminescence from noble metals when exciting them with a powerful near-UV light source. He also showed that the shape of this spectrum was dependent on the temperature of the metal.

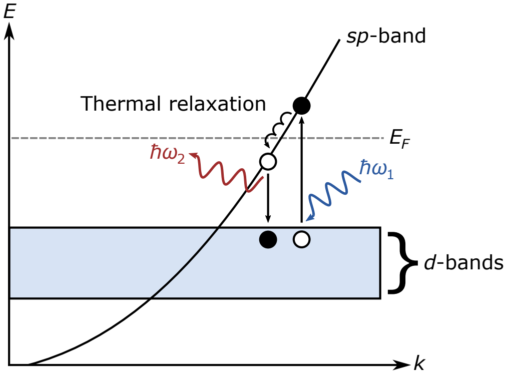

Figure 5.1: Schematic of the photoluminescence process in metals. d-band electrons are optically excited into a higher energy sp-band. After some set of thermal relaxation processes, the excited electron recombines with a d-band hole, emitting a photon of different wavelength.

Mooradian's explanation for the observations was that by illuminating the metal close to the interband transition edge, it is possible to excite electrons from the d-states up into the sp-conduction band. Here the electrons will have time to thermally relax by phonon emission, before radiatively recombining with holes in the d-band (see Fig. 5.1). Because there is no strict band gap, like in a semiconductor, the electrons can equally efficiently relax to various different energy states before re-emitting a photon. This creates a broad spectrum of luminescence[88]. By cooling the metal down to cryogenic temperatures, it is observed that this spectrum becomes more narrow. At low temperature, the electrons and holes inherently have a more narrow distribution of initial thermal energy, and they will be more likely to re-emit photons of similar energies as the exciting photon[88].

Later in 1986 G. T. Boyd *et al.* would investigate the enhancement of gold photoluminescence from rough surfaces[89]. They attribute the higher luminescence signal observed from rough films to be due to localized surface plasmons hosted in the nanostructured surface roughness. Because of the presence of resonant structures, both the light absorption and emission processes are enhanced, as compared with the flat films[85, 89]. Like Mooradian, they find that the efficiency for the luminescence process from the smooth films is about η~10^{-10}, while in some cases the signals from rough films can be close to an order of magnitude larger. They also investigate two-photon excitation of luminescence, reporting that a luminescence signal is only observed from the rough films. They attribute this to the fact that a two-photon process is even more sensitive to the field enhancement from the plasmons in the rough films.

In 1998 J. P. Wilcoxon *et al.* were the first to observe photoluminescence from gold nanoclusters[90]. They found a significant dependence between the metal cluster sizes and emission efficiency. For the smallest of their investigated clusters, they reported η~10^{-4}-10^{-5}. Later studies by several other groups would go on to improve this to η~10^{-3}, when investigating nanoparticles or nanostructures of different dimensions[91–96]. These later results also showed a very strong dependence of the luminescence on the plasmon resonances of the structures. This has mainly been attributed to the plasmons enhancing absorption and emission of certain wavelengths of light. However, from these types of resonant nanostructures it has become possible to observe photoluminescence from noble metals in infrared energy ranges that could not be supported by interband transitions[85]. This has resulted in multiple alternative explanations for the observed luminescence, ranging from black body radiation[87, 96–98], inelastic light scattering[99, 100], *intraband* excitation emission processes[40, 87, 101], to direct photoexcitation of electrons in plasmonic structures[85].

5.1 Two-photon luminescence

As discussed above, it is also possible to stimulate luminescence in metals by two-photon absorption. The basic principle is very simple: Instead of using one photon of energy $\hbar\omega_1$ (like in Fig. 5.1) to excite the luminescence, two photons of energy $\frac{1}{2}\hbar\omega_1$ are used[89]. Two-photon luminescence (TPL) is thus a three particle process, and as such the efficiency decreases. Two-photon excitation however also leads to new spectral features[89, 97]. Usually for single-photon luminescence prominent peaks are seen in the spectrum from radiative recombination near the interband edge of the metal. For TPL, the spectrum is generally more broad and evenly distributed, with a potential peak for second-harmonic generation (SHG). This is also how TPL was initially observed in 1981 by C. K. Chen *et al.*, as a broad background spectrum in their experiment of enhancement of SHG from rough metal films[102]. Because of its much higher sensitivity to field enhancement effects, TPL can be spectrally engineered to a very high degree[93, 97, 98].

5.1.1 Measurement of TPL

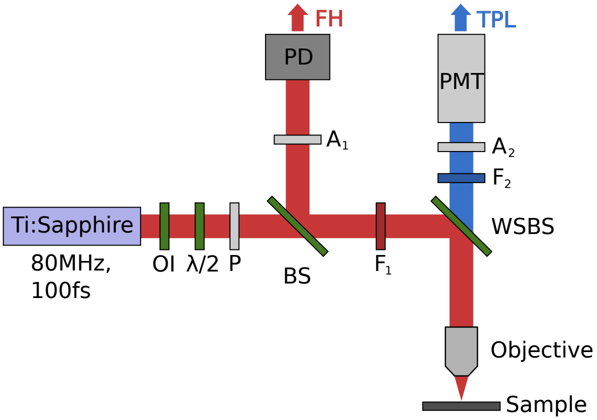

Figure 5.2: Overview of the TPL set-up utilized for all TPL-measurements presented here. The optics consists of a reflection microscope with a scanning sample stage, using a fs-laser as illumination source.

All TPL-investigations presented here were done in collaboration with Prof. S. I. Bozhevolnyi's group at University of Southern Denmark, with the measurements carried out by either S. M. Novikov or J. Beermann. On Fig. 5.2 is a schematic drawing of the TPL set-up that was used. The set-up is based on a reflection microscope, where the same objective is used for sample illumination and signal collection. The light source used is a fs-pulsed Ti:Sapphire laser ($730 - 860$ nm, ~100 fs, 80 MHz repetition). The laser is typically operated at 740 nm, which we will refer to as the fundamental harmonic (FH) frequency.

The light from the laser is passed through an optical isolator (to stop back-reflection from the sample into the laser cavity), a half-wave plate, polarizer, beam splitter, bandpass filter (matching FH wavelength), and a wavelength-selective beam splitter, before being focused onto the sample by a $100\times$ (NA $=$ 0.70) microscope objective. From the reflection back from the sample, the wavelength-selective beam splitter sorts the TPL-signal to go through a filter (350-550 nm pass) before being collected in a photomultiplier tube. The FH-signal is then sent back through the first colour filter, and the signal is diverted to a photodiode by the first beam splitter. This allows for simultaneous collection of the sample's linear reflectivity (FH-signal) and its TPL-signal (the two filters serving to reduce mixing of signals).

By mounting the sample on a computer controlled scanning stage, it is possible to make scanned images of the TPL- and FH-signal across an area of the sample. See Fig. 5.3 for an example of a typical TPL-image. By the half-wave plate and polarizer, it is possible to vary the incident power and polarization of light very accurately. As the initial light entering the setup is linearly polarized to the axis of the optical isolator, the half-wave plate and second polarizer allows the operator to easily scale the power of the beam by partially cross polarizing it at the desired polarization.

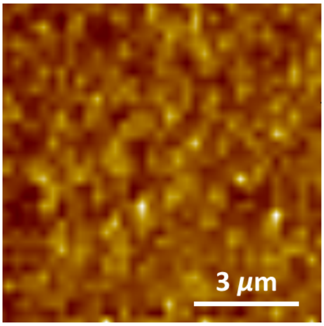

Figure 5.3: Example of a typical TPL-image recorded from a 6 nm percolation gold film. Isolated 'hot spots' show higher signal by about 20-30% than the rest of the film. As the resolution of the measurement is diffraction limited, it is not possible to truly resolve individual metal clusters.

5.1.2 Enhancement of TPL

As discussed above, it is possible to see an enhancement of photoluminescence from a rough metal film as compared to a smooth metal film. This has been attributed to the electric field enhancement from the plasmons hosted in the nanoscale features in the rough film[89]. In this section we will discuss how it is also possible to see large TPL-signal enhancement from semi-continuous gold films[103].

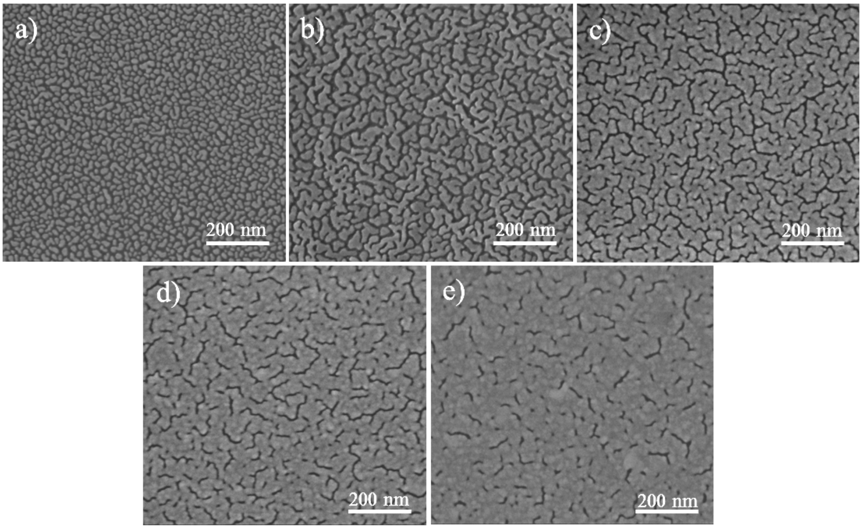

Figure 5.4: SEM-images of five different percolation gold film morphologies achieved by deposition onto a glass substrate. **(a)** 3 nm, **(b)** 6 nm, **(c)** 8 nm, **(d)** 10 nm, and **(e)** 12 nm.

By varying the deposition time while depositing at a constant rate of 2 Å/s, five gold films on glass substrates were fabricated. Scanning Electron Microscope (SEM) images of the resulting gold morphologies can be seen on Fig. 5.4. From these images we see again that the gold follows the characteristic Volmer-Weber growth process, starting out as isolated clusters in Fig. 5.4.a, then merging to large intertwined clusters in Fig. 5.4.b, before finally fully percolating and becoming a progressively denser film through Fig. 5.4.c-e.

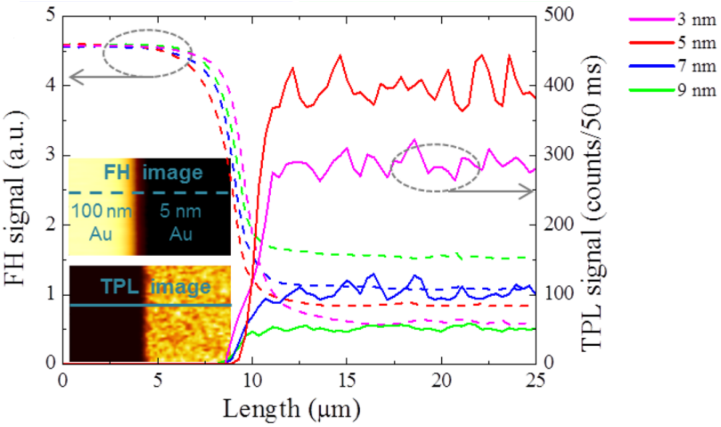

Figure 5.5: TPL (solid lines) and FH/reflectivity (dashed lines) from 100 nm bulk gold and thin gold film samples. One half of the scanned area of the sample was bulk gold, and the other a thin percolating film.

On Fig. 5.5 we show the difference in TPL-signal between a bulk gold film and four different percolation films. To produce these samples, first a 100 nm bulk gold film was deposited on one half of the substrate by using a silicon shadowmask to cover the other half. Next the same sample had a thin gold film deposited across it without the shadowmask. This allows us to record the TPL- and FH-signals from both types of samples in the same focus and measurement. For all deposition thicknesses the semi-continuous gold films have significantly larger TPL-signals than the bulk half of the sample, with the 5 nm sample having the highest signal. We also see the expected FH-signal from the percolation films, with thicker depositions having higher reflectivity. In order to more thoroughly investigate the TPL-enhancement's dependence on deposition thickness, we fabricated a broad set of samples from 2-12 nm depositions.

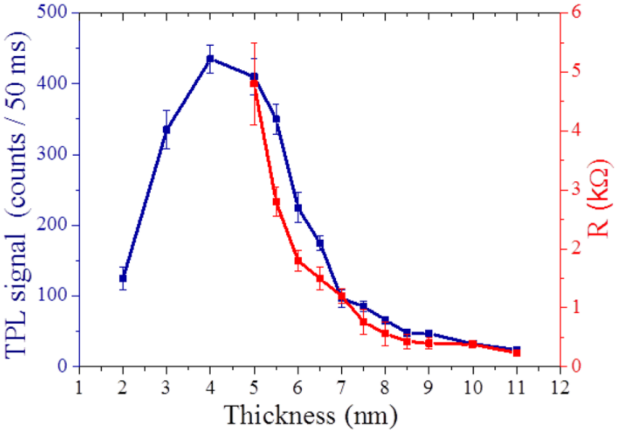

Figure 5.6: Electrical resistance and TPL-signal from various thicknesses of gold deposition on glass substrates. TPL-signal recorded at constant incident power and a wavelength of 740 nm

Using a photoresist and defining a simple narrow strip pattern with UV-lithography before metal deposition, it is possible to perform consistent electrical resistance measurements of the different film thicknesses. By restricting the percolation films into same size narrow strips, we can ensure that we are measuring the resistance on a comparable scale, even with a simple 2-point probe measurement. In Fig. 5.6 we show that the percolation threshold for our fabrication is around 5 nm deposition, as this is the point at which the film strips become conductive. In the same figure we have also plotted the averaged TPL-signal from the same sample thicknesses, showing that the TPL-signal has its largest enhancement around the film's percolation threshold.

We can understand this in terms of the plasmon distribution in percolation films based on their filling fraction. Generally, the largest field enhancements are observed for films close to the percolation threshold, while above and below the percolation threshold the predicted and observed enhancement is lower[19, 28]. We can also understand this fact in terms of the geometry around the percolation threshold, as this point is uniquely defined to be when the system transitions to consist of a large connected cluster. That would automatically infer that just around the percolation threshold, the film will have the highest possible amount of small gaps between the metal clusters per area. Likewise, these gaps between the metal clusters are also likely to be only a few nanometres[25], ensuring the highest degree of field localization in these gap modes.

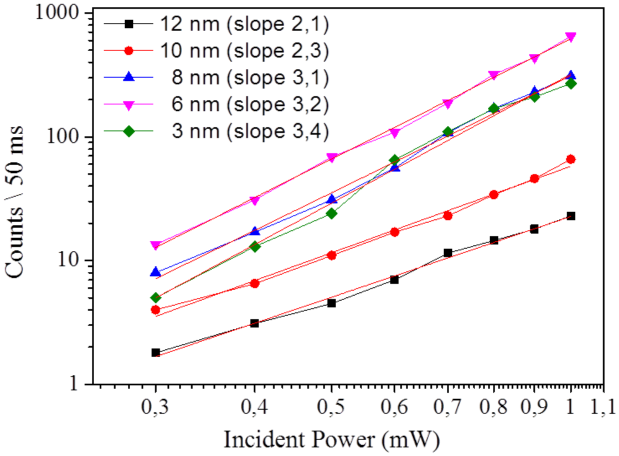

Figure 5.7: Measured TPL-signal from five different gold morphologies as a function of incident power. Red lines show linear fits to extract the slope. Excitation at 740 nm.

On Fig. 5.7 we see a log-log plot of the averaged TPL-intensities for 5 different films for different laser powers of excitation. For increasing power we would expect a quadratic dependence between the TPL-intensity and the incident power, as the TPL-signal is from a 2-photon process. However, for several of the samples we see slopes that are well above 2. We have attributed this increase in intensity to white light generation in the gold films[104]. A low-pass filter is used to filter out the FH-signal from the photomultiplier tube collecting the TPL-signal (collecting TPL between 350-550 nm). We could expect part of the white light signal to 'overlap' the TPL-measurement. From white-light generation in dielectrics, we would expect the white-light signal to have $I_{WL} \propto P_{in}^4$[104]. This would then explain the larger than expected slopes (see more details in next section).

Upon comparison between TPL-enhancement from percolation films on silicon and glass substrates we also notice a clear difference. For similar incident powers we record a significantly higher TPL-signal from glass substrates compared to silicon, almost by 2 orders of magnitude, see Fig. 5.8. Between the two different silicon substrates (p-doped and undoped) of Fig. 5.8 we also see that the low conductivity undoped silicon substrate has TPL-signals 2-3 times larger than for the boron doped silicon.

We generally attribute the difference between glass and silicon substrates to the differences in heat conductivity between the two materials. Intrinsic silicon is about 2 orders of magnitude a better heat conductor than glass[105].

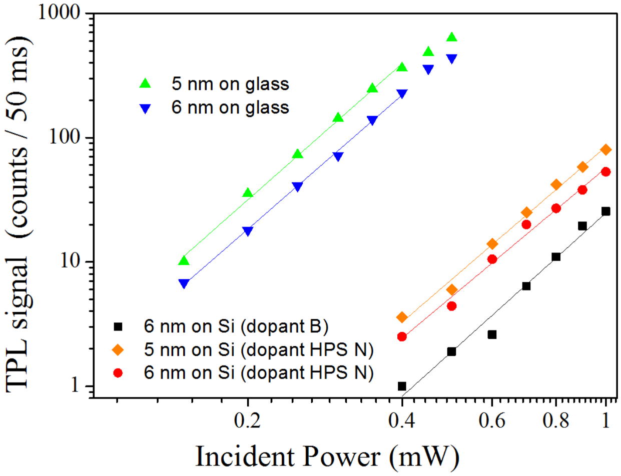

Figure 5.8: Comparison of TPL-signal from 5 and 6 nm gold percolation films on glass and silicon substrates. Two types of silicon substrates have been used, boron doped (p-type) and high purity silicon (HPS)/undoped silicon. Excitation at 740 nm.

A thermally insulating substrate would allow the metallic structures where the plasmonic hotspots are hosted to heat up more (less heat carried away by substrate material). We know from the previous section above that phonons are an important aspect of gold photoluminescence. As a result, the temperature of the gold influences the luminescence spectrum[88], with a hotter sample producing larger intensities for a broader wavelength range. Another explanation could be charge carrier excitation in the silicon, potentially screening the plasmon resonances in the gold, lowering field enhancement.

5.2 White light generation

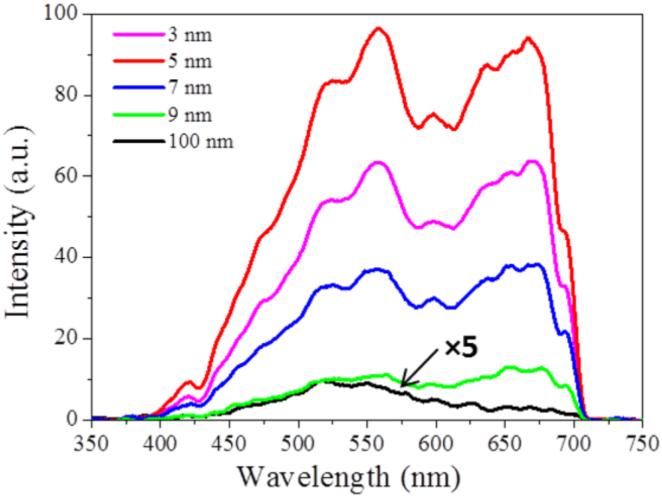

Figure 5.9: WL spectra recorded from several different gold percolation films on glass substrates. The sharp cut-off above 700 nm is attributed to a filter in the measurement setup. Excitation at 780 nm, and the average incident power was ~0.4 mW for thin gold films and ~10 mW for the 100 nm gold sample.

White light (WL) generation from plasmonic gold nanostructures was first observed in 2005 by P. Mühlschlegel *et al.* [104][1]. In their experiment they investigate the optical response from plasmonic gap antennas by pulsed laser illumination. Besides seeing TPL coming from the gold making up the antennas, they also observe WL continuum generation in the gaps of their antennas. Likewise when plotting their signal strength compared to incident power, they find a higher than quadratic power dependence for WL generation. The exact mechanism for the WL generation is still not fully understood, but large field enhancement seems to be a requirement, and the effect is highly non-linear[86, 87, 106].

On Fig. 5.9 are several WL spectra from percolation films and a bulk gold sample. The spectra were recorded with a similar set-up as the one shown in Fig. 5.2. The set-up has been modified to use a spectrometer as read-out for the 'TPL-signal' and a notch-filter has replaced the low-pass filter, to cut only the FH-signal. Like in reference [104] we observe a noticeable peak around ~550 nm that could be attributed to the interband edge in gold[89, 104]. We also observe a noticeable peak around ~675 nm, however the notch filter to remove the 780 nm excitation results in the hard cut-off around 720 nm. The 5 nm sample again proves to have the highest signal intensity, which we again attribute to the fact that films near the percolation threshold have the largest degree of field enhancement. Our measurements match the previously reported results from a very similar experiment in reference [29], although they do not see a significant peak around 550 nm. When we compare to the bulk (100 nm) sample, we see most prominently a peak in this 500-550 nm area, which is consistent with photoluminescence from gold's interband transistions. However, this signal is also significantly weaker than the ones measured from percolation films.

---

[1] Although continuum generation from gold percolation films has been reported as early as 2000[29]

Ducourtieux *et al.* attribute the continuum generation to optical non-linearities that are strongly enhanced from the field enhancement of the plasmon resonances in the gold films. The broad range of possible excitations thus provide a wide optical range of enhancement, leading to WL generation. They also identify the maximal WL generation to be from films at the percolation threshold, which in their fabrication is identified as 5.5 nm deposition.

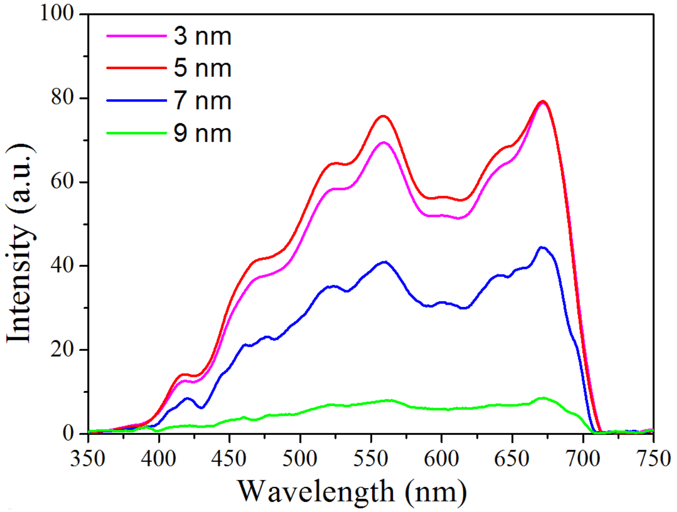

Figure 5.10: WL spectra from different percolation film thicknesses on intrinsic silicon substrates. Excitation was done at 780 nm, and the average incident power was ~2.0 mW

Fig. 5.10 shows WL spectra from percolation films on silicon substrates. The arbitrary units in both Fig. 5.9 and 5.10 corresponds to 200 counts/s, but a much larger incident power of ~2.0 mW was needed to achieve similar signal intensities from the percolation films. The spectra show a great deal of similarity to those from glass substrates, but do seem to show higher relative signal around 450 nm than for the films on glass. The peak around ~675 nm also looks much more narrow.

To summarize our findings: We see broadband WL emission from our gold percolation film samples when illuminated with fs-laser pulses. The maximal amount of emission is seen from films close to the percolation threshold, which is around 5 nm gold deposition. We also see a significant difference in efficiency of WL generation between gold films on glass or non-conductive silicon substrates, with almost 100 times higher signal from the films on glass substrates. Films on doped silicon substrates show even lower efficiency. We have attributed this difference due to the similar difference in heat conductivity between the two substrate materials, leading to a higher degree of plasmonic heating in the gold structures on glass substrates.

6 Near-field observation techniques

A very commonly encountered limitation of conventional optical investigations, is that of the diffraction limit. The diffraction limit was first described by E. Abbe in 1873[107]. In practical terms, it says that a beam of light cannot be focused to a spot with a diameter smaller than half the wavelength of the light. This also means that using a microscope objective, it is not possible to resolve an image with greater resolution than what is set by this limit. For visible light, this results in a resolution limit around ~200 nm, which is very unsuited for any imaging in nanoscience. There are alternative imaging techniques, like electron microscopy (see chapter 7) to get around this[1], however for some purposes it is still desired to stay in optics for sub-diffraction imaging/focusing. Plamonics offers a direct way to focus optical fields to spatial dimensions well below the diffraction limit[2], as we saw for both surface plasmon polaritons and localized surface plasmons in chapter 3.

However, we are interested in direct imaging of sub-diffraction sized features. This kind of measurement for optical near-fields was first realized by the group of D. W. Pohl in 1984[110, 111]. Inspired by other scanning probe techniques like scanning tunnelling microscopy (STM), that also have their inception in the early 1980's, Pohl's group utilized a sharp metal coated quartz 'waveguide' with a roughly ~20 nm aperture defined at the tip. By then shining a laser through the small aperture, and scanning it across the sample in a few nanometres proximity, it was possible to record optical images with a resolution of about 10 times higher than that predicted for the diffraction limit[110]. This technique has now come to be known as scanning near-field optical microscopy (SNOM, sometimes NSOM), and has been a popular method to study percolation films historically[19, 29]. Modern devices use a similar method as described above, although replacing the quartz waveguide with a tapered optical fiber, or in the case of scattering-type SNOM (s-SNOM) use a metal coated or uncoated atomic force microscope (AFM) cantilever (more on this later).

We will in this chapter briefly discuss the optical near-field, and in particular how it can be utilized for sub-diffraction imaging with a SNOM. We will also detail some practical aspects of SNOM experiments done here at DTU in the time of my PhD.

---

[1] The de Broglie wavelength of electrons at a similar energy as visible photons is still several orders of magnitude shorter, allowing perfectly for sub-diffraction imaging.

[2] Far-field sub-diffraction imaging techniques like confocal microscopy[108] and stimulated emission depletion (STED) microscopy also exists[109].

6.1 The optical near-field

As discussed above, the diffraction limit puts an upper threshold to the degree with which propagating optical fields can be focused and resolved. It can be shown that the origin of the diffraction limit comes from spatial filtering during propagation of the fields[112, 113]. If we regard a point-dipole source[3], it will be characterized by a Dirac delta function, and such a function has an infinite range of frequencies associated with it. Upon propagation the high frequency components will be filtered out, and the imaging optics will also not be able to collect all components. Because of this loss of information, it is not possible to reconstruct the dipole source as a single point, and it will instead have a finite spatial size upon imaging[31].

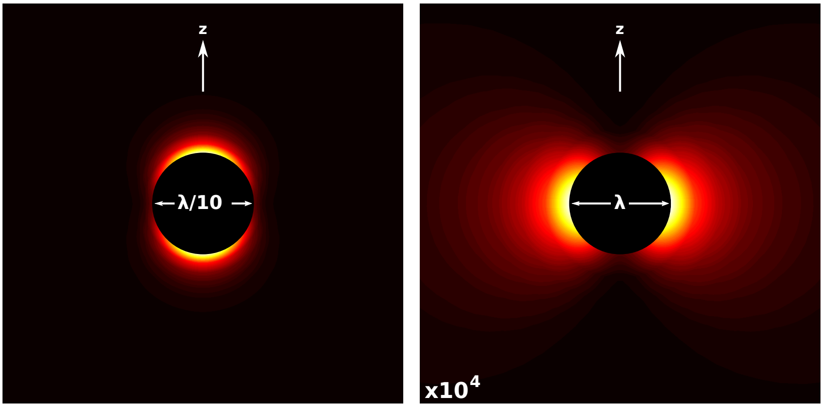

Figure 6.1: $|\mathbf{E}|^2$ plotted for a dipole orientated along the z-axis in different distances relative to the emitted wavelength[111]. On the left image we see the near-field orientated along the dipole, on the right we see the far-field emitted transverse to the dipole. The colour scale for the far-field image is magnified by 10^4 relative to the near-field image.

However, this only applies to the propagating part of the field of a dipole. We have so far neglected the near-field of the source. The near-field manifests itself as an evanescent field-component that extends only a small fraction of a wavelength away from the dipole source, see Fig. 6.1. We saw previously in chapter 3, total internal reflection in a prism can produce evanescent fields. Likewise, an evanescent field can also be coupled into a prism or waveguide to result in a propagating mode (often called photon tunnelling[31]). The intensity of this propagating field can then be collected with an ordinary photodetector.

---

[3] The smallest electromagnetic source we can imagine. Any larger emitter could potentially be regarded as a superposition of such point dipoles.

In other words, by bringing a small apertured waveguide probe close to a dipole-like source of radiation on a sample (or from other sources of evanescent fields, like plasmons), it is possible to measure the near-field intensity. Scanning this probe across the sample can then produce an image of the sample's near-field intensity with a spatial resolution limited to the aperture size of the probe (typically few tens of nanometres). Likewise, it is also possible to couple radiation into this probe and generate an evanescent field with which to excite a sample locally in the near-field.

These are the generalized operating principles of a SNOM. In the next section we will discuss the practical implementation of a SNOM in an optical set-up, as done here at DTU with the Danish Micro Engineering (DME) DS 45-40 SNOM.

6.2 Scanning near-field optical microscopy

In this section we will detail the operating principles of the DME DS 45-40 SNOM used during my PhD-studies (many of these principles will apply in general for similar SNOM systems). However, because of limitations of the system and lack of external technical support (the manufacturing company, Danish Micro Engineering (DME), underwent bankruptcy proceedings during my thesis studies), it has only been possible to acquire partial results from this system in the time limit of my studies.

6.2.1 Fiber optic probes and shear-force feedback

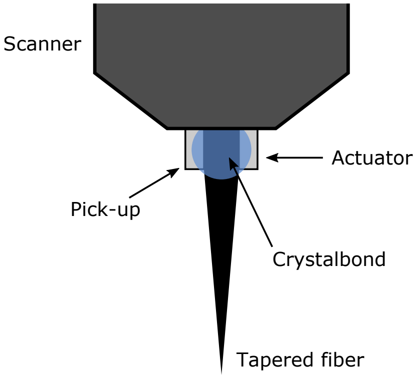

Figure 6.2: Overview of the mounting of the fiber optic probe.

We will start our discussion with the optical probes themselves, and the shear-force feedback system of the piezoelectric scanner used to track the probe/sample distance. A schematic of the system can be seen on Fig. 6.2.

The probes used have all been single mode optical fibers pulled to sharp tapers with an apex of ~150 nm. The fibers have not had any metal cladding or aperture defined, and were manufactured and purchased from the company LovaLite. The probes are mounted to the system by manually glueing[4] them in-between two piezoelectric elements, which are then mounted on the rest of the 3D piezo scanner used for scanning the sample surface. One of the piezos in the mounting will act as an actuator to drive a vibration of the fibertip, while the second piezo will act as a pick-up to record the amplitude and frequency of the vibration. The fiber tip will oscillate like a stiff beam that is clamped in one end. By scanning across different actuation frequencies, it is possible to find the frequency for which the fibertip has its mechanical resonance frequency. Typical resonance frequencies for the mounted fibers are in the tens of kHz, with resonantor quality factors of 120-160 achievable with some care during the mounting process.

By driving the fiber at its resonance frequency, it is possible to detect damping of its oscillation with the pick-up piezo. By bringing the tip into close proximity of a sample surface (few to tens of nanometres), the tip of the fiber will experience van der Waals forces from the sample's surface[111]. The result of this is a shear-force in the fiber that dampens its vibration. The degree of dampening depends on the distance between the probe and the sample surface. This kind of shear-force feedback is thus an ideal way to track the probe/surface distance.

6.2.2 The DME DS 45-40 SNOM

On Fig. 6.3 is a schematic drawing of the optical set-up and supporting electronics for the SNOM experiments at DTU. The SNOM is run in a combined illumination and collection scheme. The light source is a 5.0 mW helium neon laser (wavelength ~633 nm). The laser is first run through an optical isolator to cut any back-reflections into the laser cavity[5]. In order to utilize a lock-in amplifier for the collecting photodetector, we have to modulate the laser with an optical chopper. After the chopper, the laser is passed through a Glan-Thompson polarizer aligned with the polarization of the optical isolator. Passing through a 50/50 beamsplitter, the laser is now coupled into the flat end of the tapered optical fiber using a 3D stage and a microscope objective (20×, NA $= 0.5$). Some portion of the laser light will be transmitted from the fiber and excite the sample (the rest is reflected back into the set-up). The same fiber will also collect a signal from the sample, which is passed back and collected with the same microscope objective. The signal from the fiber will then be passed back to the beamsplitter, where it will be partially reflected. The signal is then passed through another Glan-Thompson polarizer that is rotated 90° in relation to the first. The purpose of this cross-polarization is to cut as much of the background signal from the rest of the set-up as possible[6]. Finally, the signal is collected by a photodetecter, which passes its voltage signal to the lock-in amplifier.

---

[4] We use crystalbond 509 as a simple hot-melt glue. The hard resin-like texture of the solid glue seems ideal for the mechanical resonator purposes here.

[5] The tapered end of the optical fiber dramatically limits the transmission of the fiber, resulting in a strong reflection back into the optical set-up.

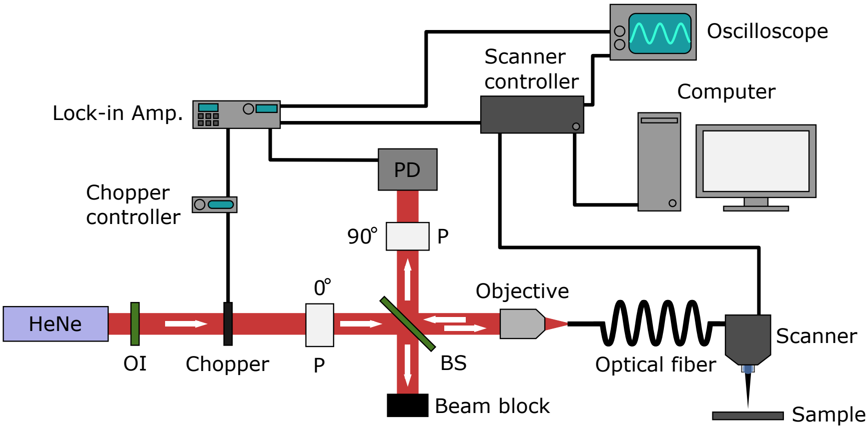

Figure 6.3: Schematic drawing of the optical set-up used for the DME DS 45-40 SNOM at DTU.

The lock-in amplifier is supplied with the chopper's modulation frequency from the chopper controller, and is able to amplify the signal from the detector by several orders of magnitude. The amplified signal is then passed on to the scanner controller, where it is correlated with the fibertip's position on the sample. The shear-force of the fiber is recorded simultaneously as the optical signal, and thus it is possible to record a near-field and shear-force topographic image at the same time.

An oscilloscope is also connected to both the lock-in amplifier and the scanner controller. From the signal of the lock-in it is possible to monitor that the chopper is accurately modulating the laser signal, and from the scanner controller it is possible to observe the shear-force feedback that is adjusting the height of the fiber tip during a scan.

Finally, the sample stage consists of a manual 2D translation stage. A simple 10× periscope mounted microscope is positioned perpendicular to the near-field probe. A camera is attached to the microscope and connected to the computer, allowing for real-space imaging of the probe's position on the sample, both before and while scanning.

---

[6] Any light that is reflected from the fiber will follow the same beam path as the signal we are interested in, but will be polarized to the first polarizer, thus cut in the cross polarization.

In addition to the 'reflection' geometry shown in Fig. 6.3, it is also possible to operate the system in 'transmission'. Here the laser source is instead shone through the sample from below, and the fibertip is scanned across the sample for collection of the near-field signal.

6.2.3 Measurements

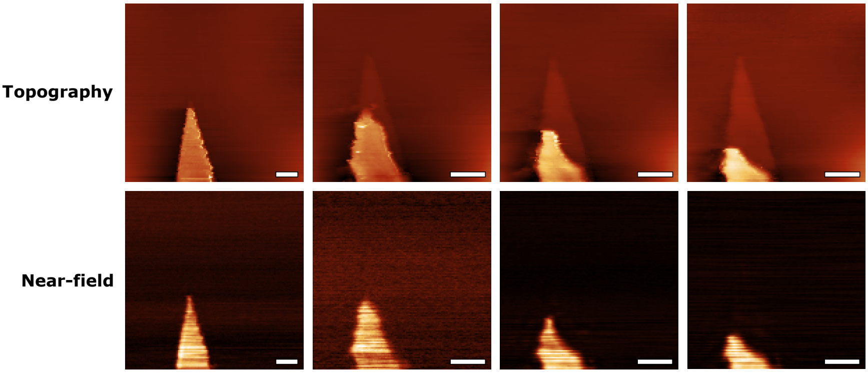

Figure 6.4: Consecutive scans of the same 40 nm thick gold taper on SiO_2 substrate. The top row of images shows the recorded topography from the shear-force feedback, the bottom row the recorded near-field intensity. Scale bars are all 5 µm.

A constant limitation of the SNOM setup has been degradation of soft metal samples during scanning, likely caused by too large sample/probe interaction. Examples of recorded images of a gold taper on glass substrate can be seen on Fig. 6.4. With each consecutive scan we see how more and more of the gold taper is scratched off from the substrate.

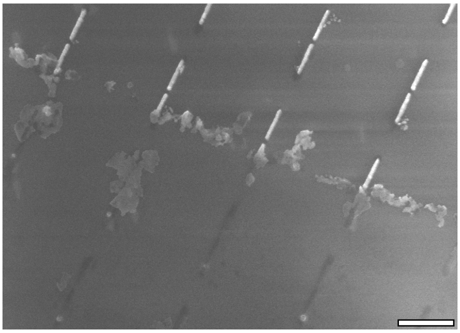

Figure 6.5: Edge of a region scanned with the SNOM system of gap nanoantenna on silicon substrate. The bottom half of the image shows the scanned region, where the antenna have been removed completely during scanning. The antenna are 40 nm thick gold deposited on top 10 nm titanium. Scale bar is 500 nm.

Fig. 6.5 shows a SEM-image of an array of nanoantenna that have been scanned with the SNOM. The scanned part of the antenna array very clearly shows damage to the nanostructures, with some having been removed even completely from the substrate.

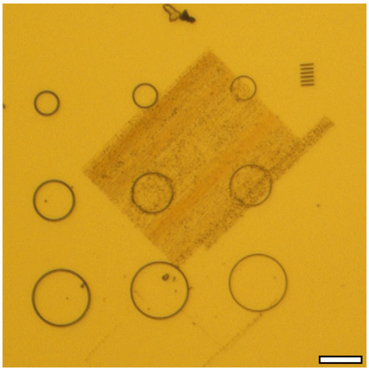

Figure 6.6: 150 nm gold film on glass substrate with circular trenches milled by FIB. A large square of high surface roughness can be seen left-over from a region scanned by the SNOM. Scale bar is 10 µm.

The problem also extends to even thick gold films. Fig. 6.6 shows an optical microscope image of a 150 nm thick gold film deposited on a glass substrate. Circular rings have been defined in the film using focused ion-beam (FIB) milling intended for plasmonic lenses[55]. However, when attempting to scan the gold film, surface roughness can be seen to increase for each consecutive scan. When observing the regions scanned with the SNOM in a microscope, very clear and defined scratch marks can be observed.

Despite the issues, it has been possible to extract some information from the generally very noisy optical images. Fig. 6.7 shows a scan over 500 nm diameter latex spheres dispersed on a glass slide, where they have self-assembled into a lattice of closely packed spheres[114]. From both the topography and optical images, it is possible to discern the widths of the spheres from a profile extraction.

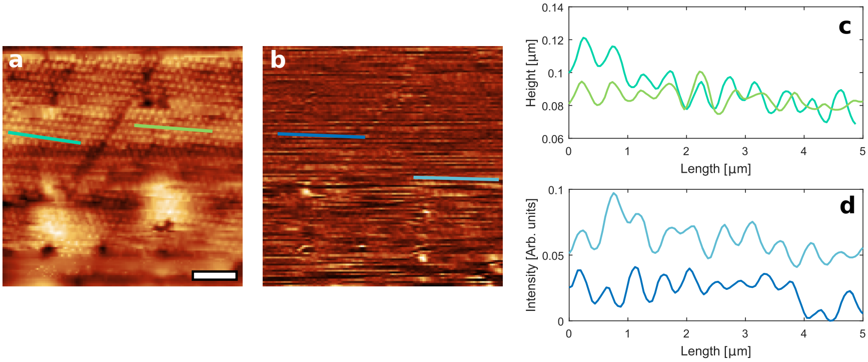

Figure 6.7: Profiles of latex spheres on SiO_2. **(a)** shows a topographical image recorded with the SNOM set-up, while **(b)** shows the simultaneously recorded optical signal. **(c)** shows profiles extracted from (a), and **(d)** shows profiles from (b). Scale bar for (a) and (b) is 3µm.

6.2.4 Scattering-type SNOM

So far all of our discussion has involved so-called apertured SNOMs, i.e. the near-field probes used have a clearly defined aperture that the evanescent fields are transmitted through. However, a second class of SNOM devices exists, where instead a sharp tip is brought close to alter the local optical properties of the sample. This tip can be metal coated to couple plasmonically to the sample, or uncoated to simply alter the local optical properties. By illuminating the sample and collecting a signal of scattered light in the far-field, it is possible to see how the same probe changes the sample's properties locally. Raster scanning the probe across the sample to record this in different positions can make an image. We refer to this kind of SNOM as aperture-less SNOM, or scattering-type SNOM (s-SNOM).

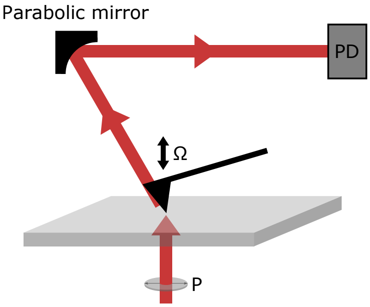

Figure 6.8: General beampath for a s-SNOM operated in transmission configuration. A polarized light source from below is shone at the sample, while the AFM cantilever is scanned across the sample. A parabolic mirror is used to collect and direct light scattered from the sample by the AFM tip toward a photodetector, where the intensity is measured.

An example of the beampath for a s-SNOM in a transmission configuration can be see on Fig. 6.8. Typically s-SNOM setups will have an additional parallel beampath for so-called pseudoheterodyne interferometry (not pictured in Fig. 6.8). The modulated signal from the AFM cantilever's oscillation frequency, Ω, is compared to a reflection from a mirror oscillating at a frequency M. By then demodulating the combined signal it is possible to measure the phase as well as the amplitude of the near-field signal[115].

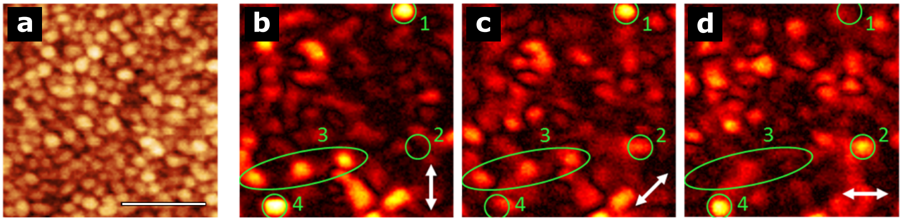

Figure 6.9: Topography, **(a)**, and near-field images, **(b-d)**, of a 5 nm gold percolation film on glass substrate. All images were recorded from the same region of the sample. Excitation was done in the far-field with transmission from below of 1500 nm light. The illumination source was set to three different polarizations. The polarization of the excitation source is marked with the white double arrows in (b-d). The scale bar is 200 nm

Fig. 6.9 shows images recorded of a 5 nm gold film on glass substrate, recorded with a NeaSpec system in Prof. S. I. Bozhevolnyi's group by V. A. Zenin. The s-SNOM is operated in ’transmission’ mode where the sample is illuminated from below with a linearly polarized 1500 nm laser. The sample is then scanned consecutively in the same region, for three different polarizations of the illuminating laser. In Fig. 6.9.b-d, four regions have been highlighted. In these four regions we see distinct hotspots of near-field intensity for the three different polarizations. We also see that there is almost no overlap of the physical position of hotspots between images Fig. 6.9.b and d, where there is a 90° difference in excitation polarization. We can conclude from this that the plasmonic hotspots present in the films are highly polarized, and that the hotspots’ spatial distribution for different excitation polarizations are also fairly unique (as also shown previously for general random clusters[26, 27]). We will show how this fact can be exploited for anisotropic optical modification in gold percolation films in chapter 8.

7 Electron Energy-loss spectroscopy

In chapter 3 we discussed how plasmons are able to couple and interact with external light. We also briefly touched on the fact that plasmons were initially understood experimentally, from exciting bulk plasmons in thin metal films with an electron beam in a transmission electron microscope (TEM)[42–44]. The excitation of the plasmons were observed as energy losses in the electrons as they were passed through the samples. By using a magnetic field as a dispersive element[1] for the electron beam after it has passed the sample, it is possible to observe the energy losses of the electrons over a wide energy spectrum. We refer to this method as electron energy-loss spectroscopy (EELS). EELS was first developed in 1944 by J. Hillier and R. F. Baker[116]. By filtering the electrons used to image a sample by energy, they were able to observe the high-energy core loss edges (hundreds to thousands of eV) in the probing electron beam. These edges are the result of the electron beam interacting with tightly bound inner shell electrons of the sample's lattice atoms. This is now a common method in EELS to make detailed maps of a sample's elemental composition, as the edges are unique identifiers for different elements[117].

For plasmons, we are however interested in low energy losses (few eV). We will here briefly discuss how an EELS measurement is performed in modern microscopes, and what data processing procedures need to be done to extract the plasmon energies and their EELS amplitudes from the spectra.

7.1 Transmission electron microscopy

The field of an electron beam can be shown by explicit calculation with Maxwell's equations to be confined within close distance to the beam[118]. This means that the electron beam can be regarded as a source of evanescent electric fields. As we saw in chapter 3 and 6, such fields can be used to great effect to excite plasmons. Furthermore, the beam's field can also be expressed in individual frequency (energy) components in terms of its Fourier transform. We can thus think of the electron beam as a supercontinuum evanescent light source[118], which is an ideal experimental probe for plasmon excitation. Optical experiments are typically restricted to one or few wavelengths of light, but in EELS we can probe multiple different energies, in one measurement, from the polychromatic source.

---

[1] The strength of the Lorentz force from the magnetic field that deflects the electrons depends on their velocity, the magnitude of which is dependent on their kinetic energy.

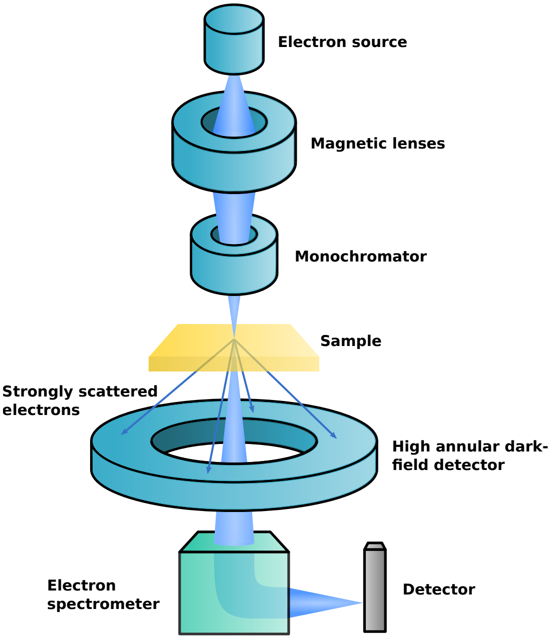

Figure 7.1: Schematic of the STEM EELS acquisition process. The electron beam is focused to a point in the sample and raster scanned across it. The electrons scattered at a high angle are collected by the ADF detector, while the electrons only weakly scattered are passed through and analysed in a spectrometer.

All EELS results presented in this thesis were acquired on a FEI Titan TEM with a monochromator and a probe aberration corrector, hosted at DTU's Center for Electron Nanoscopy (CEN). On Fig. 7.1 is a simple schematic overview of how an EEL spectrum is recorded in a scanning transmission electron microscope (STEM). Electrons are emitted from a source (typically a field emission gun[119]), and are then collected and focused onto the sample into a sub-nanometre spot through a series of magnetic lenses[120]. The typical energy of the electrons used for such experiments is hundreds of keV, and to ensure enough signal electrons pass through the sample, its thickness should normally not exceed 100 nm. In our case, the microscope is also fitted with a monochromator above the sample, to ensure as narrow a spread in electron energy as possible[121]. When passing through the sample the electrons can interact with it in different ways, although the majority of the electrons will not interact at all. These 'non-interacting' electrons make up a large peak in the final spectrum, that we will refer to as the zero-loss peak (ZLP). The width of the ZLP will also show the energy distribution of the electron beam, and it is from its full-width-half-maximum we can see the energy resolution[121, 122].

Some of the electrons interacting with the sample will be scattered at very high angle. These electrons are collected by an annular dark-field detector (ADF) that sits like a ring below the sample. From this detector it is possible to record images of the sample's morphology in greyscale, where the contrast comes from the electron scattering rate. Heavier elements and thicker regions of the sample will appear brighter (more scattering), and different crystal orientations in a polycrystalline sample will appear with different contrasts as well, due to their differences in scattering rate[123].

Those electrons interacting only weakly with the sample (or not at all) will pass through to the electron spectrometer. Here by using a magnetic field they are dispersed onto an electron detector, their deflection angle and subsequent position on the detector revealing their kinetic energy.

7.1.1 The energy-loss spectrum

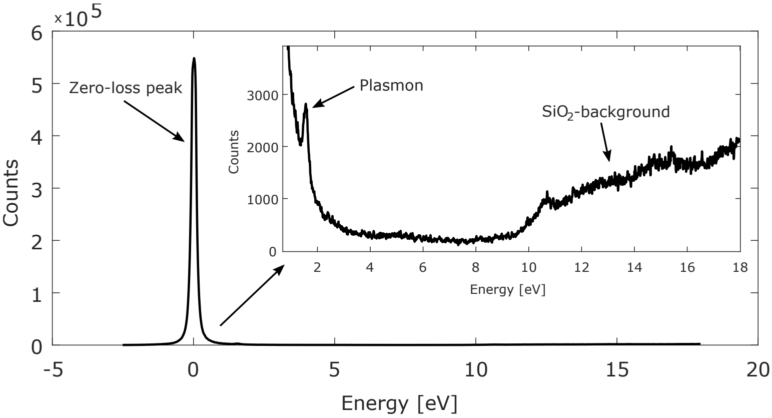

Figure 7.2: An example of an EEL spectrum taken from a gold percolation film on a 18 nm SiO_2 membrane. The ZLP is clearly seen as the dominant spectral feature. An insert shows a magnified view of the rest of the spectrum, highlighting a plasmon peak around 1.5 eV which is still partially inside the ZLP. The broad background signature of the SiO_2 membrane material is also seen from around 10 eV.

Fig. 7.2 shows an example a of a recorded EEL spectrum from near a gold cluster in a gold percolation film on a thin glass substrate (this type of sample is discussed in greater detail in chapter 8). The ZLP is prominently visible in the spectrum, and in the magnified inset we can see how the ZLP overlaps to some degree with a peak that resembles a plasmon resonance. From around

10 eV we also see a broad signal coming from the membrane structure acting as substrate for our sample. We will later use an integral of this to help normalize our data, as the intensity of this signal will be consistent across the sample. As we are interested in the plasmonic properties of our sample, and since we see a great deal of the resonances can overlap with the ZLP, we will have to perform a background subtraction on our data.

For all EELS results presented in this thesis, we have opted to fit a power-law to a subset of the data points that are to the left of the first plasmon resonance in a spectrum. The calculated fit is then subtracted from the entirety of the spectrum, and all data points below 0.5 eV are discarded, as the background correction is not accurate for this range (anything from 0.0-0.5 eV is also solidly inside the ZLP and difficult to interpret anyway).

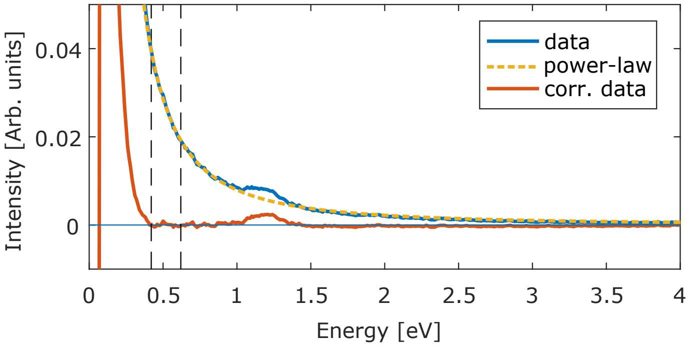

Figure 7.3: An example of how a small subset of the EELS data (marked in-between the dashed vertical lines) can be used to calculate a power-law fit for subtracting the ZLP.

7.2 Mapping plasmons with electrons

A natural extension of being able to record EEL spectra from an electron beam passed through a sample, is to record such spectra in a 2D array from the sample. We refer to this kind of array as a hyperspectral image (sometimes also referred to as a data cube, as the EELS intensities are in x, y, and energy coordinates).

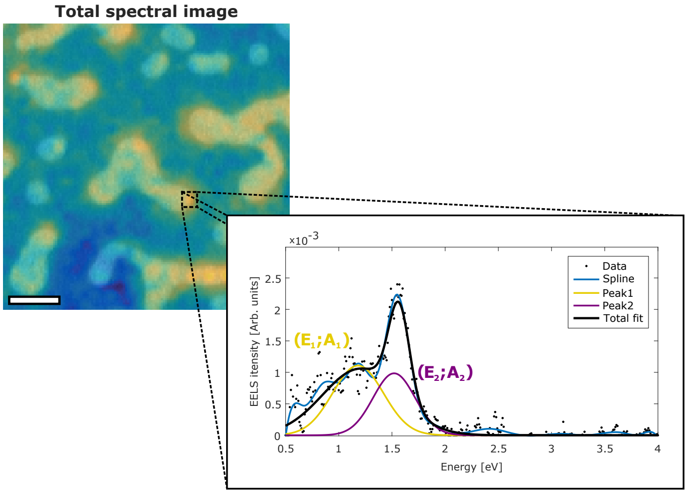

Figure 7.4: Example of a spectral image of a laser modified 5 nm gold film on a thin glass substrate. An EEL spectrum from a point on one of the particles in the image has been highlighted, showing how successive Gaussian fitting can be used to identify plasmon peaks and extract their amplitudes and resonance energies. The scale bar for the spectral image is 75 nm.

On Fig. 7.4 we see an example of a summed EELS map overlaid on top of the sample morphology it was recorded from. Each spectrum in the image has had the ZLP subtracted as described above, and been normalized by the integral from 10-14 eV of the SiO_2 background. An example EEL spectrum from a point near a gold particle has been highlighted. We can utilize the EELS data of a hyperspectral image in two main ways:

- Integrate the EELS signal along the energy axis for a certain energy range to make a 2D colour intensity map that spatially maps the plasmons in this energy range.
- Extract the central position and height of the plasmon peaks in the spectra to categorize the resonance energies and intensities in the image.

In this thesis we will be utilizing both approaches with hyperspectral images of several different gold percolation film morphologies. A very big challenge however for extracting the plasmon resonance energies and amplitudes from percolation films, is the sheer volume of data from a typical spectral image. In our case, a typical image consists of ~10,000 spectra. Each of those spectra can then contain vastly different amounts of plasmon resonances, at widely different energies (some even overlapping considerably). As a result, we have had to develop a very computationally intensive automatic fitting routine. In a sort of 'first sorting', for a given spectral image we first average all spectra together and plot the result. In this summed set of spectra a set of Gaussian functions are fitted by hand to the resulting 'primary modes' of the system - those modes either so intense or frequent in the individual spectra that they end up dominating the average of all spectra.

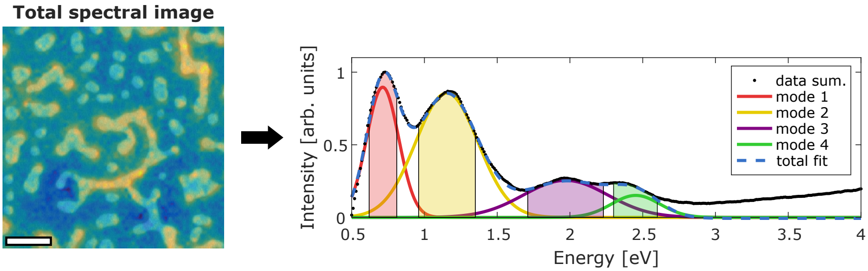
Total spectral image

Figure 7.5: Summed spectra from a spectral image, showing four primary modes present in the image. The scale bar for the spectral image is 150 nm.

An example of such a summed image can be seen on Fig, 7.5. The data are from the same spectral image as the excerpt in Fig. 7.4. A fit of the sum of four Gaussian functions is also highlighted, with the individual function terms also plotted. From the four Gaussian functions we can designate regions of interest within a portion of their widths (in this case within 50% and above of their amplitude, i.e. full-width-half-maximum). For each of the individual spectra that make up the spectral image, we now make a smoothing spline (to reduce the random oscillations from noise in the data), and we look primarily for peaks in the spectra within the energy ranges defined by the widths from the primary modes. After noting the amount of peaks identified, a series of independent Gaussian fits are carried out for each peak in only the data from the vicinity of the peak. The quality of this fit (in this vicinity) is then evaluated from the residual, and if it is found to be too poor, it is ignored for the further data treatment.

After double-checking the validity of the independent Gaussian fits, the width, amplitude, and central position of each of the remaining fits are then used as initial guesses for fitting of a sum of the same number of Gaussian functions across the full spectrum data. From this total fit we can now extract the amplitude and resonance energy of all of the identified (and verified) plasmon resonances in the spectrum. An example of this series of fits is shown in Fig. 7.4. This procedure is then repeated for each spectrum of the image, and the collected data can later be described statistically.

This method is of course not perfect, and will not catch all the different varieties of plasmon resonances present in the image. We justify the use of the primary modes to initially 'target' our search for plasmons, by the fact that our images are of $500 \times 500\,\mathrm{nm}^2$. This size fits quite well with the diffraction limited spot in an optical experiment. So for any optical experiments we could compare our EELS data with, this kind of averaging of the modes in the image would already have occurred in the optical experiment as well. In other words, an optical experiment would also be most sensitive to the primary modes of the system, as everything else would be averaged out by the large spotsize.

8 Optical modification of semi-continuous gold films

A general energy loss process for plasmons in metals is due to Ohmic resistive losses. Basically, the electron scattering processes as we understand them in the Drude picture (see chapter 2) is the transfer of energy from the electrons to the material's crystal lattice by phonons. This transfer of energy to the lattice is also what we traditionally understand as heating of a material. The more general case of Ohmic heating is that of an electrical resistor with a large current passed through it. Due to resistive losses in the resistor, energy from the electron current will be deposited as heat, causing it to increase its temperature. Because of gold's relatively low melting point (1060 °C), it is possible to melt gold locally from the Ohmic heating caused by the decay of strong plasmon excitations. In this chapter we will discuss some of the general processes for this reshaping, and also how it is possible to alter the general properties of gold percolation films by such local reshaping from plasmon excitation. The exact mechanisms at play and parameters needed to attain certain reshaping modes has been beyond the scope of the work in this thesis, but we will refer to results of prior literature on the topic to frame our own work.

8.1 Photothermal processes in metal nanoparticles

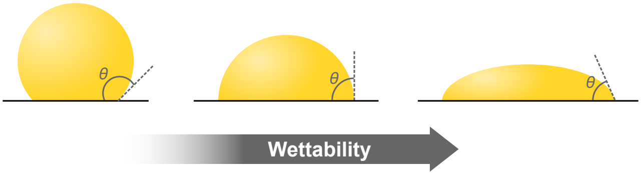

Figure 8.1: Three different substrates with increasing levels of wettability for a liquid drop on top of the substrate. The wetting angle θ is indicated for each case.

There are several ways in which gold can be reshaped by plasmonic heating, but the most pedagogical case is probably that of a gold nanorod melting into a sphere. For now we simply deal with the case of a metal nanorod being heated, and neglect the complications of the heat energy being delivered by plasmon decay[1]. When the metal rod reaches a temperature matching its melting point, which may well be lower than the melting point of the bulk metal[2], the now liquid metal will try to contract into a sphere because of surface tension forces[126]. A very general trend observed for liquids (and plasmas) is that they will contract to spherical shapes to limit their surface energy (the atoms at the surface have higher energy than the bulk atoms because of the lack of neighbour atoms to bond with). We can understand why a spherical shape is preferred from the simple fact that a sphere is the 3D Euclidean shape with the least amount of surface area per volume[126]. However, when dealing with liquids on a substrate things become a little more complex, as the spherical droplet will be deformed based on the surface's wettability[130–132]. For a surface with high wettability (strong liquid-surface interaction) the liquid droplet will be flattened and spread out across the substrate, while for a low wettability substrate (low liquid-surface interaction) it will remain almost spherical. Fig. 8.1 shows examples of different wetting angles. For the specific case of water we refer to surfaces with low wettability as hydrophobic, and high wetability as hydrophilic. We will discuss the influence of the substrate material when melting metal particles in more detail in a later section.

---

[1] Several processes happen at different timescales when a metallic particle is plasmonically excited[20, 124–126].

As stated above, we would expect a general shortening and 'rounding' of isolated particles when they are melted. We can also consider the case of a coupled system of plasmonic nanoparticles (see chapter 3). Here the situation is a little more complicated. In general two processes can occur: Separation, or merging/welding of the particles into one. For weakly coupled particles with a relatively large separation between them, we would expect the case of them decoupling. However, for the case of two very closely situated particles they can actually exchange material and start to melt together with the right excitation[20, 21, 23]. To make matters more complicated, a kind of intermediate process can also occur, where two particles are joined by a small 'neck' extending between them, instead of fully merging. This kind of 'necking' has been studied for joining together self-assembled nanosphere chains[20, 22, 133].

On Fig. 8.2 we have highlighted how the longitudinal plasmon resonance for elongated particles are influenced by their reshaping, as if being partially melted/contracted towards more spherical shapes, while preserving the volume of the particles. The curves presented here are based on simulations done in collaboration with T. Repän.

---

[2] Due to the high relative surface energy associated with nanoparticles, as compared to bulk materials, their melting points can often be considerably lower[127–129].

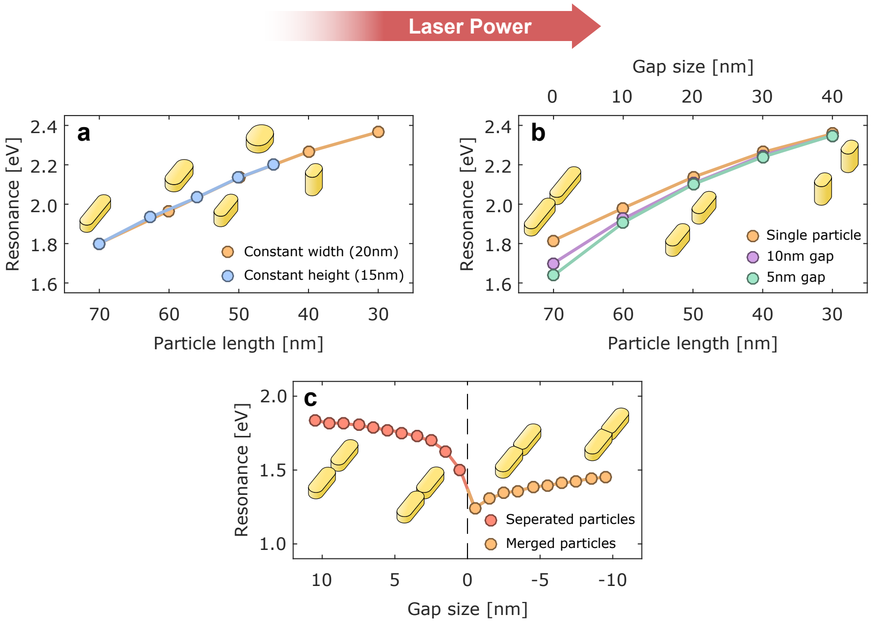

Figure 8.2: Simulations of the longitudinal plasmon resonance for gold rods being reshaped as if melted. In all plots reading from left to right corresponds to an increase in deposited power into the system. **(a)** The case of a single gold nanorod being contracted, while its volume is preserved. To compensate for the shortening, volume is either added to the height or the width of the particle. **(b)** The case of two coupled gold rods being shortened, so that they eventually decouple. Lost volume from contraction added back as height. **(c)** Two gold nanorods moved towards each other, to emulate merging. Lost volume in the particles' overlapping region is added to the height of the connected particle.

On Fig. 8.2.a is the initial case of an elongated particle being contracted, and to maintain its volume it is either made taller or wider. We see the expected outcome that its plasmon resonance blueshifts as it contracts in length. We also see that the blueshift is only affected by the change in dimension parallel to the plasmon excitation, i.e. both the widening and heightening of the particle corresponds to similar curves. In Fig. 8.2.b we study the case for a set of coupled particles. By shortening both of the two particles we effectively shorten the gap between them, which as expected for the bonding mode of a plasmonic dimer causes a blueshift in resonance energy. We have also plotted the resonance of a single particle of the same shape, to see at which point the particle coupling is broken and they effectively become two separated particles. Finally, in Fig. 8.2.c we study the case of two particles merging. Here, instead of shortening the particles, their centre coordinates are moved towards each other. As this is initially somewhat the opposite case as in Fig. 8.2.b, we expect to see a redshift before the two particles merge. As soon as the two particles merge, we return somewhat to the case of Fig. 8.2.a, as we have one new very long particle. As the two particles overlap more and more, any lost volume from the overlap is added to the joint particle's height. Effectively, the continued merging of the particles acts as a shortening of the joint particle, and we return to the case of Fig. 8.2.a with a blueshift.

Another photothermal process worth briefly mentioning is that of laser ablation, i.e. directly evaporating or sublimating material by transfer of large amounts of energy from high laser intensity. This technique is however typically not reliant on plasmonic excitation (although it can be), opting instead for simply delivering the energy by high intensity photon absorption. Laser ablation has found uses for the synthesis/fabrication of nanoparticles by ablating material into an aqueous solution[134, 135]. Because the process mostly relies on intensity of the laser itself, it is also compatible with a wide variety of materials[134, 135]. As the processes studied in this thesis are not believed to involve ablation, we will not discuss it in further detail here.

8.1.1 Substrate influence

In our own experiments of melting and reshaping gold percolation films with a fs-laser (the same laser as in the TPL set-up discussed in chapter 5), we have noticed a significant difference in the morphology changes between percolation films on glass and silicon substrates.

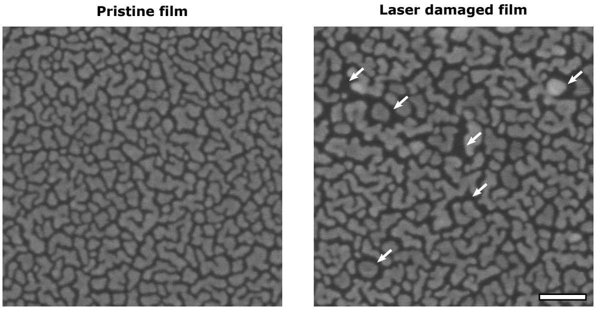

Figure 8.3: SEM-image of how the fs-laser affects a 5 nm gold percolation film on an intrinsic silicon substrate (undoped). An average laser power of ~3 mW was used to damage the film, at a wavelength of 740 nm. Arrows added to highlight regions of large morphology change. The scale bar is 100 nm.

On Fig. 8.3 are examples of a 5 nm gold deposition on an intrinsic silicon substrate. One part of the film has been left as deposited, and another part has been illuminated with a 740 nm ~3 mW fs-laser pulse to induce morphology changes. The overall changes in the film's morphology are quite subtle, but manifests themselves in two ways. First, several areas of the laser illuminated film shows abnormally wide gaps between neighbouring clusters when compared with the pristine film. Secondly, several rounded or spherical looking particles show up in the damaged image. These particles are also always situated near larger gaps to neighbour clusters. Both of these things would indicate that a gold cluster has been melted and turned into a gold droplet from surface tension. Lastly, some regions of the film appear virtually unchanged, indicating that the injection of heat into the system happens very locally, and it also does not propagate a great deal from its injection point. The local introduction of heat is very consistent with the idea that the heating happens from plasmon Ohmic losses, as heat can only be introduced in the specific plasmonic hotspots corresponding to the laser wavelength used.

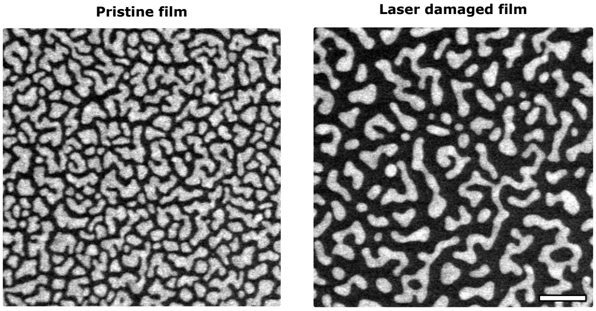

Figure 8.4: STEM dark-field image of laser damage done in a 5 nm gold percolation film on 18 nm glass membrane substrate. A laser power of ~0.5 mW was used for the damage at 740 nm wavelength. The scale bar is 100 nm.

If we now consider the case of a 5 nm percolation film on a 18 nm thin SiO_2-substrate as shown on Fig. 8.4, we see that the morphology changes from the laser are significantly different. Despite having been illuminated at a much lower average laser power of ~0.5 mW compared to the ~3 mW of Fig. 8.3, the morphology for the glass substrate seems to have been affected much more. Not only do the changes on individual clusters seem more significant (more rounded and spherized), the changes also seem to have affected every cluster in the region, and is no longer isolated like for the silicon case.

Gold has a similar wetting angle of about 135° on both polished glass and silicon[130–132]. However, despite having similar specific heat capacities, the heat conductivity of silicon is almost 100 times higher than that of glass[105]. We attribute the massive differences in morphology changes to be due this discrepancy between the two substrate materials. Because the glass substrate is incapable of acting like a proper heat sink to divert the heat away from the gold structures where injected, the heat instead dissipates into the substrate plane. The result is that the effects of the laser are much more equally felt by all of the percolation film.

This analysis is of course not conclusive as a direct comparison between glass and silicon, as the glass samples are also placed on thin 18 nm membranes. As a result, the mass of the substrate is much lower in the glass samples. This will give it a lower heat capacity and make it function worse as a heat sink/temperature reservoir, in addition to being a worse heat conductor. However, when trying to perform polarization sensitive laser modifications to the films by laser writing, samples on thick glass substrates were always found to be less consistent and reliable compared with silicon[136]. This fact also leads us to believe that the silicon substrate is much better suited for isolating the melting to just specific sites of plasmonic hotspots, as this would give better polarized behaviour. We will discuss this kind of polarization manipulation in the next section.

8.2 Polarization inscription

We have studied how it is possible to 'inscribe' specific polarization sensitivity into the optical properties gold percolation films, both on silicon and on 18 nm thin glass TEM membranes. All fs-laser writing and TPL-measurements were like in chapter 5 done in collaboration with Prof. S. I. Bozhevolnyi's group at University of Southern Denmark. We will start our discussion here by looking at the case of gold films on silicon substrates, as it is the most straightforward.

8.2.1 Silicon substrates

As we discussed in chapter 4, and saw in chapter 6, the plasmonic hotspots in percolation films are strongly polarized. We can use this fact along with photothermal processes to remove hotspots for a given polarization from a sample. In fact, this specific removal of hotspots with a given polarization is what is visible on Fig. 8.3, as the laser has only damaged the local part of the film that hosted a plasmon resonance matching the polarization of the laser. We can see the consequence of this removal of polarization when we study TPL-enhancement, like in chapter 5, from the altered films.

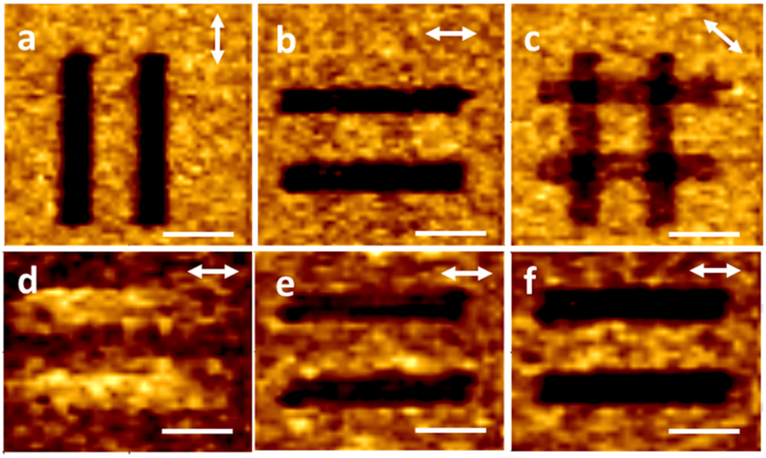

Figure 8.5: TPL-images from a 5 nm gold percolation film on silicon substrate with laser lines written in it. **(a-c)** shows polarization and **(d-f)** shows wavelength dependencies. Two pairs of lines in **(a-c)** were written with the laser polarization aligned along the lines. Both writing and reading were done at the wavelength of 740 nm. A pair of lines in **(d-f)** were written at the wavelength of 780 nm with the laser polarization along the lines again. Reading was done at the wavelength of **(d)** 740, **(e)** 780, and **(f)** 820 nm. The white arrows indicates the laser polarization during the read-out. Laser powers of ~3 and ~1 mW were used for writing and reading, respectively. The scale bars are 5 µm.

On Fig. 8.5 we see a set of TPL-images recorded from two different regions of a 5 nm gold film. In two different areas lines have been 'written' with the fs-laser. In Fig. 8.5.a-c two pairs of lines have been written before recording TPL-images, with the polarization of the laser aligned along each pair of lines. TPL-images have then been recorded in the same laser set-up, using a lower laser power than for the writing. The result is that when recording a TPL-image with the polarization that is parallel to the polarization of the writing, the laser written areas show up in the TPL-images as a clear dark contrast with almost no TPL-signal. For the case of Fig. 8.5.c, we see that when aligning the read-out polarization to 45°, we can see all lines at the same time. What we see here, is that it is possible to selectively 'extinguish' the TPL-signal from a region of the film for a given polarization.

The case of Fig. 8.5.d-e demonstrates the effects of different wavelengths. Here again a pair of lines have been written with a laser polarization along the lines, at a wavelength of 780 nm. Then the lines have been scanned again, but now with a shorter wavelength of 740 nm in Fig. 8.5.d, the same wavelength of

780 nm in Fig. 8.5.e, and a longer wavelength of 820 nm on Fig. 8.5.f. For the case of Fig. 8.5.d we see a larger enhancement of TPL-signal from the laser written region, while for the cases of Fig. 8.5.e and f we see the expected reduction of TPL-signal. We can understand this 'contrast inversion' from our discussion in the previous section above: When resonant elongated plasmonic particles are shortened due to photothermal processes their resonance frequency will blueshift. In other words, the clusters that were affected by the longer wavelength will be shifted towards a shorter wavelength. Hotspots were however already present at the shorter wavelength, and were themselves unaffected by the writing process at the longer wavelength. The net effect is that now at the shorter wavelength a larger concentration of resonances for the given polarization has been achieved, and we thus see an even larger enhancement of TPL when recording images at this shorter wavelength.

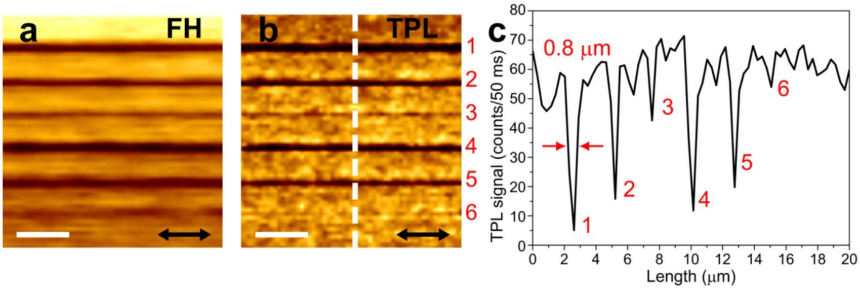

Figure 8.6: (a) FH and **(b)** TPL-images of a 5 nm thin gold film on a silicon substrate, obtained with different laser powers during the writing procedure (exposure time of 50 ms, scan speed of 20 μm/s, spot size of ~750 nm) and different scanning step sizes. Read-out and writing performed with the same polarization. For the scanning step size of 360 nm, the FH writing powers are: P_1~5 mW, P_2~4 mW, and P_3~3 mW. For the step size of 800 nm powers are: P_4~5 mW, P_5 ~4 mW, and P_6~3 mW. **(c)** Cross sections taken from the dashed line in (b). The scale bars are 5 μm.

On Fig. 8.6 some examples of the degree of signal reduction achievable for different step sizes and laser powers can be seen. Here three different laser powers and two step sizes for the laser scan have been compared. For the case of 5 mW and a step size of 360 nm (peak 1 in Fig. 8.6.c) we see it is even possible to almost completely extinguish the TPL-signal for a given polarization (when reading back at same or longer wavelengths). A very similar writing process has also been reported recently, highlighting writing with three different polarizations in the same spot, and wavelength separated images as well, see reference [106].

8.2.2 Glass substrates

We have now seen how the localized reshaping of plasmonic hotspots in gold films on silicon substrates can be used for polarization control of the film's optical properties. Now we will move on to the more complex case of reshaping gold films on glass substrates. As discussed above, here the heat seems to dissipate much more into the gold films than when compared with silicon samples. However, we will show that it is still possible to achieve polarization effects in these structures, despite the fact that the morphology changes are much less isolated.

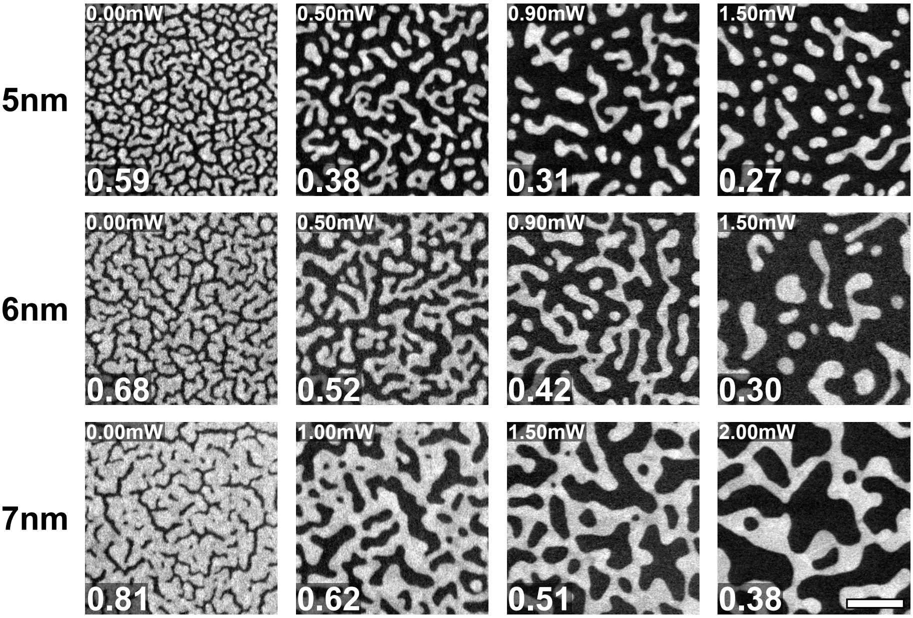

Figure 8.7: STEM dark-field images of different gold percolation film morphologies on 18 nm SiO_2 TEM membranes. The films have been illuminated with the same scan parameters, but different laser powers. Numbers in the upper left corners are the laser power used for illumination, and for all samples a wavelength of 740 nm was used. The numbers in the lower left corners of the images indicate found filling fractions of gold from image analysis. All images are at the same scale, the scale bar is 150 nm.

Fig. 8.7 shows a small 'catalogue' of how different deposition thicknesses give different film morphologies, and how these morphologies are influenced by various levels of fs-laser power. The films were illuminated with the laser in separate positions with the different laser powers. The filling fraction of gold in each image has also been calculated. For the 5 nm sample we see that it initially consists of smaller isolated clusters, and the effect of the laser seems to be to melt and merge many of these clusters. For increasing laser powers we also consistently see the filling fraction drop, indicating that more and more of the gold in the sample is being collected into the new clusters (assuming minimal evaporation/dissipation into the substrate).

The 6 nm sample appears to be closer to the percolation threshold than the 5 nm sample. It consists of bigger gold clusters that are however still isolated. The effects of the laser also seem somewhat different, as the resulting morphologies for the two lower laser powers seems to become merged together in long tortuous filaments, with a few almost spherical particles mixed in-between. The case of 1.50 mW is however different. It seems this laser power is above the threshold to nearly melt the clusters completely, as they do not seem able to form the large windy clusters.

The 7 nm sample appears to be well above the percolation threshold, looking like a solid single cluster, with many small gaps in it. The effects of laser illumination seems mainly to be either fusing or opening up of the gaps in the film. For the 2.00 mW case the result appears to be a lattice of thick gold clusters that are interconnected through thin windy wires.

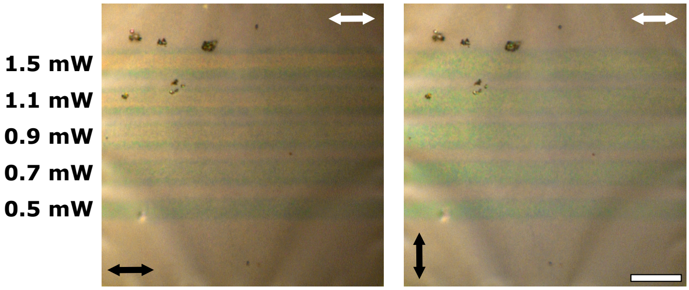

Figure 8.8: Microscope images of five lines written with the fs-laser at different powers in a 5 nm gold percolation film on a 18 nm SiO_2 membrane. The white double arrows indicate the polarization of the writing laser, the black arrows show the orientation of a polarizer inserted in the microscope before the camera. All lines were written with a wavelength of 740 nm. The scale bar is 10 µm.

From just viewing the laser illuminated regions afterwards in an ordinary microscope, it is very clear that the regions have been changed compared to the surrounding gold on the glass membrane. An example of several lines written next to each other on the 5 nm gold film sample can be seen on Fig. 8.8. When observing the sample through an optical polarizer, it also becomes apparent that there is a difference between aligning this parallel or perpendicular to the polarization of the laser used for the writing process. When aligning the polarizer parallel to the writing laser's polarization, a reddish hue becomes visible in the centre of the written lines (most apparent for the 1.5 mW line.). This colour is however absent when viewing in the perpendicular orientation. The 6 and 7 nm samples show similar behaviour, but it is less pronounced than for the 5 nm sample. We will focus our attention on this sample as a result.

Because the laser modified samples are on a transparent substrate, we can perform optical transmission spectroscopy on them. The results of such measurements done in collaboration with M. Geisler can be seen on Fig. 8.9.

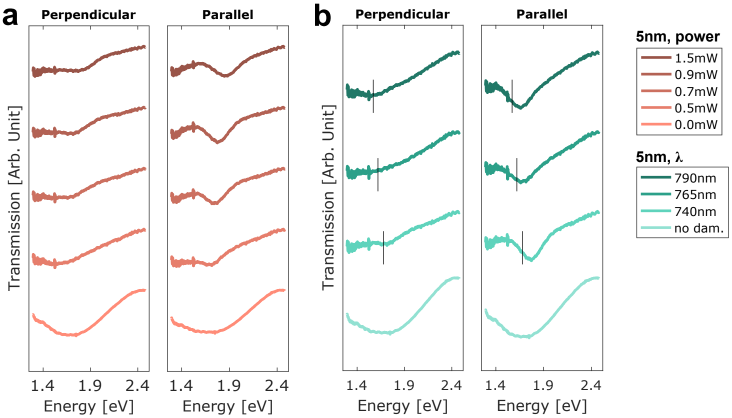

Figure 8.9: Transmission spectra of a 5 nm percolation film that has been altered with different laser powers and wavelengths. The microscope light source for illumination has been polarized either parallel or perpendicular to the polarization of the laser used to alter the films. **(a)** are spectra from regions altered with different laser powers, at a wavelength of 740 nm. **(b)** shows the influence of the wavelength of the laser used for the damage. The vertical black bars corresponds to the photon energy of the laser during the writing process.

In the transmission microscope used, we are able to change the polarization of the white light source used for sample illumination. We have recorded transmission spectra for when the microscope light source is aligned either parallel or perpendicular to the polarization of the laser used to perform the morphology changes in the samples. From these spectra we see very clearly that a polarized extinction feature is present after the laser writing. When aligning the microscope light source to parallel with the laser used for the writing process, we see a sharp dip in transmission around 1.80-2.00 eV. For increasing laser powers this dip tends to blueshift, which could indicate that the gold clusters hosting the polarized mode are further shortened along this axis in the samples made with higher laser powers. On Fig. 8.9.b we also show spectra from sample regions illuminated with the same laser power, but at different wavelengths. From these spectra we see that the wavelength of the laser used for the photothermal process is also important, as the dip in transmission seems to be just slightly blueshifted relative to the laser wavelength used (reminiscent of what happens in Fig. 8.5.d).

To study the near-field cause of this emergent polarization sensitive colour, we have recorded detailed hyperspectral images of the different 5 nm film morphologies using EELS. By integrating the EELS data in the range of 1.80-2.00 eV, we can now construct a colour map showing the regions with high electron-energy loss in the energy ranges where we see the transmission dip in Fig. 8.9. The result can be seen on Fig. 8.10 for three different powers of laser writing, and for two sets of samples that have been laser written with polarizations 90° apart.

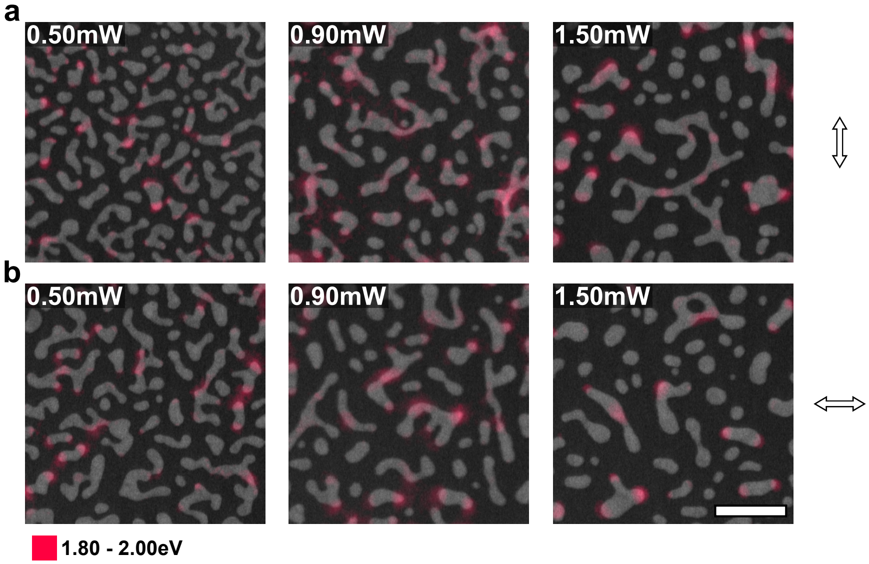

Figure 8.10: Colour maps of the recorded EEL spectra integrated in the energy range of 1.80–2.00 eV and overlaid on top of their respective STEM dark-field images of the 5 nm samples. Each row of images consists of samples with the same polarization used for laser writing (white arrows), (**a**) being the samples with y-polarized laser writing, and (**b**) the samples with x-polarized laser writing. The numbers in the top left corners of the images indicate the amount of power used for laser writing. The scale bar is 150 nm.

In these images we can identify several elongated particles that are about ~50-100 nm long and show very strong EELS signals at their endpoints. Many of these elongated particles also appear to be aligned along the polarization used when damaging the sample with the laser (especially in the 1.5 mW sample images), although many also appear to be oriented more or less randomly. Elongated gold particles with dipolar plasmon resonances could explain the polarization sensitivity that we observe in Figs. 8.8 and 8.9. However, from EELS measurements alone we cannot resolve the polarization sensitivity of the structures, as the excitation with an electron beam is not polarized. The other problem, as discussed in chapter 7, is that the excitation with electrons can also excite plasmonic dark modes, resonances normally inaccessible with just light[137]. As the polarization sensitivity observed in Fig. 8.9 is from a polarized far-field light source, we will have to correlate our near-field EELS data to how a far-field excitation would look like. In collaboration with T. Repän we have reconstructed the 3D geometry of the gold morphologies, by using our STEM dark-field images and EELS data. The process is outlined in Fig. 8.11.

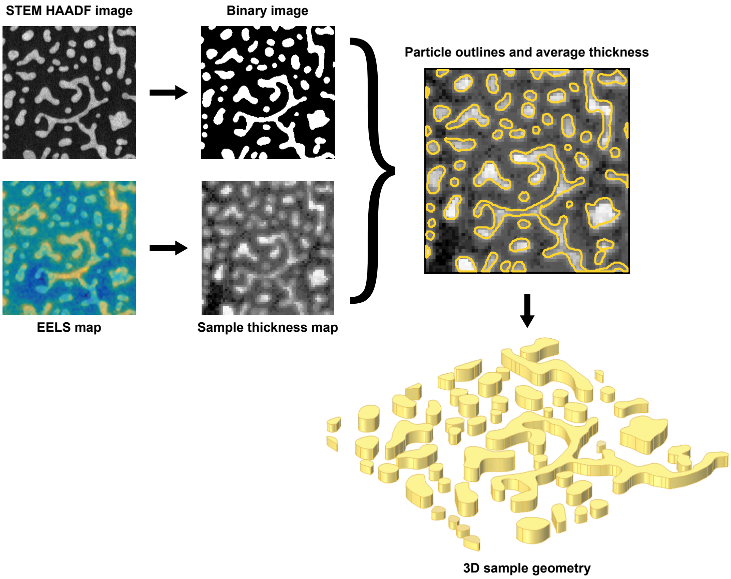

Figure 8.11: Overview of the process to generate the thin film geometries used in simulations. The dark-field STEM images are converted into black/white binaries to recover the particle outlines, and the EELS data is integrated in order to construct relative thickness maps of the samples. Using the thickness map and the particle outlines, an average thickness of each gold particle is found, and the sample geometry can be reconstructed with the clusters as relatively scaled prisms.

After reconstructing the geometries for the two regions of the 5 nm gold film damaged with 1.5 mW and different polarizations (seen in the right column of Fig. 8.10), we performed finite element simulations of far-field plane wave excitations on them. From these simulations it is possible to align the polarization of the exciting wave to parallel or perpendicular to the polarization of the laser used in the writing process. In other words, we can try to now realize how the plasmons would be excited on the gold clusters like in the transmission spectroscopy measurements of Fig. 8.9.

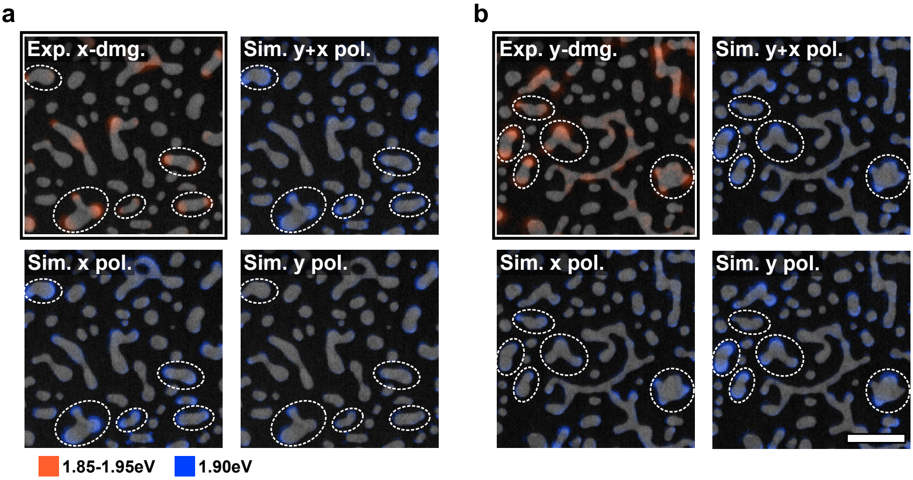

Figure 8.12: Comparison between EELS data and the norms of electric field z-components from simulated polarized far-field excitation of the 1.5 mW laser written regions in the 5 nm sample. (**a**) is for a writing laser with polarization along the images' x-axis, and (**b**) for the sample with laser writing polarized along the y-axis. The EELS data was integrated in the region of 1.85–1.95 eV and the excitation energy for simulations was 1.90 eV. The electric field norms from the simulation were taken right below the gold particles. The scale bar is 150 nm.

The results of the simulations can be seen on Fig. 8.12. We have chosen to highlight the norm of the electric field z-component in the images, as it is the field component the electrons in EELS are most sensitive to[118]. Because we have the two orthogonal polarizations for the far-field as separate simulations, we can compare the two individually, or look at their sum. We expect the sum of the two polarizations to give the greatest agreement with the EELS data, as it would most closely represent the uniform non-polarized case. We find generally good agreement between the summed simulations' field distributions and the EELS intensities. The two individual polarization simulations also seem to confirm our suspicion that indeed the rod-like particles host dipolar resonances, and they are aligned parallel to the polarization of the laser writing. For the simulations with a perpendicular polarization to the laser writing, we see very little plasmonic excitation in the gold clusters. For the simulations polarized parallel to the laser writing, we see large excitation with field distributions very similar to the EELS data.

To summarize: The effects of the fs-laser on gold percolation films on a glass substrate are very different to films on a silicon substrate. For the silicon samples the photothermal damage of the laser is very localized to the specific regions of the plasmon hotspots (likely due to increased heat conductivity of the substrate). The net effect of this is that hotspots of a certain polarization are removed from the sample after laser writing. For the glass case however, it appears that there is no big loss of plasmon resonances at the laser wavelength, as we see no strong indication of this in Fig. 8.9.b. However, similar to the silicon samples, at a slightly blueshifted wavelength (with respect to the laser used for writing), we see a large aggregation of plasmonic excitation. This effect is also strongly polarized to be aligned with the laser polarization used in the writing process, and is likely caused by gold nanorod-like particles that have formed in the sample.

8.3 Reconfiguration of modes

We detailed in chapter 7 how it is possible to extract the resonance energy and EELS signal amplitude of plasmon resonances in an EELS map. By recording hyperspectral images of intrinsic percolation films and films that have been modified with a fs-laser we can also study how the plasmon resonances in the films evolve with the morphology changes. The results of such an analysis can be seen here on Fig. 8.13. We have mapped $500 \times 500\,\mathrm{nm}^2$ regions of the four different film morphologies. Like discussed for the similar analysis in chapter 4, such an area is large enough that we can consider the sample as isotropic at this scale, and can use this area to make general statements about the film as a whole.

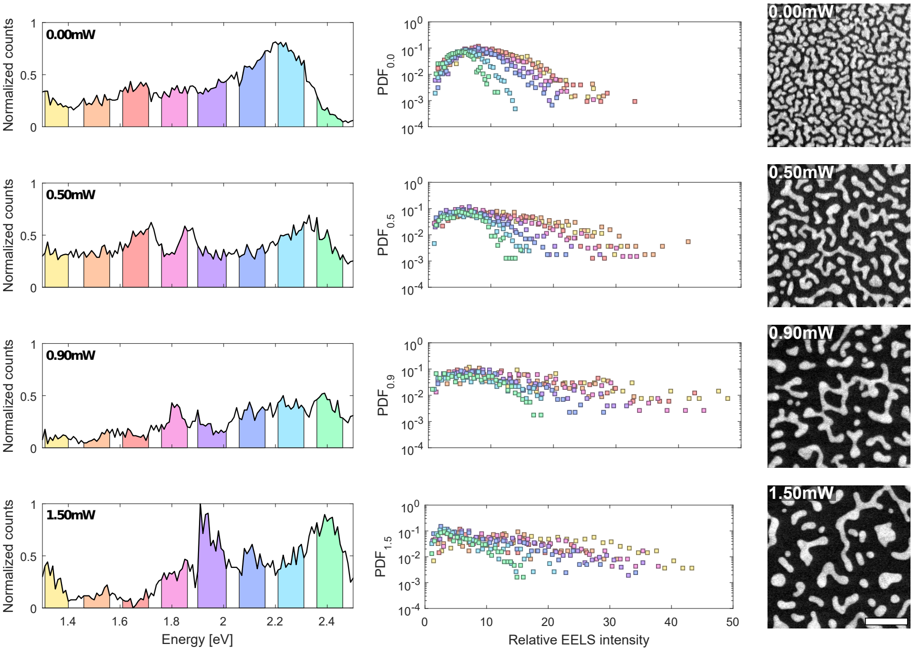

Figure 8.13: Plasmon modes for an intrinsic 5 nm gold film, and three 5 nm gold film samples that have been modified with different laser powers. The left column shows histograms of the identified central energies of plasmon resonances in the spectral images. The centre column consists of PDFs showing the EELS intensity distribution across different energy ranges matching the highlighted colours in the histograms on the left. On the right are shown STEM dark-field images of example film morphologies. The scale bar is 150 nm.

By identifying the plasmon resonances in the EELS data we can construct histograms of how many modes are present at which energy, like in the left of Fig. 8.13. If we then take all the resonances within a narrow range of these energies (highlighted colours on the histograms), we can sort them by their magnitude in EELS intensity in the spectra (amplitude), and bin them into 30 values based on their intensity. We then divide this distribution function of intensities by the total count of intensities, and we get a probability distribution function (PDF) of the EELS intensity for that energy range. Taking the 50 minimum intensities from each of the four spectral images, and calculating the median value, we can normalize the PDFs to this value. This gives us the PDFs for the relative EELS intensities, which let's us compare the PDFs between the four samples. These PDFs are highlighted in the centre column of Fig. 8.13. The shape of these PDFs now offers us insight into the system that would have been very difficult to attain by just EELS intensity colour maps. First of all, the shape of the PDF can tell us about the degree to which the gold clusters are coupled together. In prior work it has been well documented that metal percolation films exhibit Gaussian function-like PDFs for their electric field intensities[28, 78], while isolated plasmonic particles show power-law-like PDFs[82, 84][3]. In our case, we see the PDFs for the intrinsic films start out with quite Gaussian shapes, but eventually get more and more twisted into a scaling power-law shape for the samples modified with larger laser powers. When compared with the large drops in filling fraction observed in Fig. 8.7, we can conclude that we are indeed seeing the plasmonic coupling of the percolation films being lifted from the photothermal reshaping by laser illumination. Secondly, by comparing the right-most points of the PDFs (i.e. largest relative EELS intensity) between the different energy ranges, we see that for the intrinsic film we get the expected behaviour of the lower energy modes also supporting the most intense hotspots[78]. However, we also see that we generally find more intense hotspots from the laser modified films, and some of the higher energy modes especially (1.90-2.00 eV and 2.10-2.20 eV) experience almost a factor of 2 increase in their highest relative EELS intensities.

We can understand the effects of the laser as a decoupling of the clusters in the percolation films. This also causes a redistribution of the initially broad ranges of plasmon resonances into more narrow bands of resonances (seen in the histograms in Fig. 8.13).

---

[3] A single isolated dipole would simply have its field intensity scale with the distance as $I \propto 1/r^4$ in space, whereas many interacting and interfering dipoles would have a much more complex spatial scaling of intensity.

9 Conclusion

In conclusion, we have reviewed and studied the general physics of metal percolation films. We have studied how such films can be fabricated using e-beam metal deposition systems, and explained the metal growth process responsible for the self-assembly of the deposited metal into percolation structures. We have characterized the morphologies of different deposition recipes by SEM- and TEM-imaging. We have found only minor differences between glass and silicon substrates in terms of achieved morphologies from similar gold depositions, while the later studied properties of the films have deviated dramatically based on their substrate materials.

We have shown how two-photon luminescence (TPL) of gold can be plasmonically enhanced in gold percolation films. Different deposition thicknesses of metal will produce different degrees of enhancement, but we have shown that the highest degree of enhancement is found for films near the percolation threshold. In addition, we have found that percolation films on glass substrates produce TPL-enhancement by about 2 orders of magnitude higher than when compared to silicon substrates. We preliminarily attribute this to the differences between the substrates to act as heat sinks, i.e. to remove heat from the Ohmic losses in the metal structures. We have also observed white light generation from the gold percolation films, when excited with a fs-laser. The exact mechanism(s) of the white light generation in gold is still not understood. Additionally, we have also studied how it is possible to perform polarization sensitive writing with the TPL-setup in gold percolation films. We found that it is possible to locally extinguish the TPL-signal for a given polarization in the percolation films. This is achieved through photothermal reshaping processes of the gold, from scanning the region of the film with high power fs-laser pulses. We found this effect is not as easily reproducible for percolation films on glass substrates, when compared to silicon substrates. We again attribute this difference to the substrates' ability to channel heat away from the gold clusters, ensuring much more localized reshaping of clusters on the silicon substrates.

We have measured the distribution of plasmonic hotspots in our gold percolation film samples, by using s-SNOM and EELS. Using polarized excitation in the s-SNOM experiment, we have reconfirmed that the hotspots are strongly linearly polarized, and that the spatial distribution of hotspots is unique between a 90° difference in excitation polarization. Using EELS we have mapped the spatial distribution of plasmonic hotspots in percolation films, down to few nanometre resolution. This reveals the incredible complexity of how the plasmonic hotspots are formed, and how the field distributions in these films are not linked to the geometry in a simple, or predictable, way[81].

Using a quantitative/statistical analysis method, we have studied the distributions of plasmon excitations in various percolation film morphologies on 18 nm thin glass membranes. Many of these morphologies have been achieved by photothermal reshaping of the metal clusters present in intrinsic films by fs-laser illumination. We have studied how the plasmon modes are gradually more and more reshuffled for increasing laser powers used to reshape the morphologies. We have also shown how the plasmon modes in the film become less and less coupled to each other, as the system transitions into morphologies more akin to isolated gold particles for the higher laser powers.

We have also studied how this kind of laser writing leaves behind a strongly polarized plasmon excitation in the films, observable in the far-field. We have carefully reconstructed our film morphologies observed in the EELS experiments, and performed finite-element simulations of plane wave excitations on them. From these simulations we have highlighted how the polarization dependence observed in the far-field is caused by nanorod-like particles formed along the polarization of the fs-laser used for the laser writing process.

9.1 Outlook

Besides the many already interesting optical applications for metal percolation films, the possibility to modify the local optical properties of the films by fs-laser writing opens up a new set of interesting applications.

For one, the polarization sensitive writing effect in TPL-signal from percolation films on silicon substrates allows for writing of two distinct images on top of each other, with minimal cross-talk between them on read-out. This, along with the fact that the percolation films are very easy to fabricate with just simple metal evaporation systems (a method that is also easily scalable to very large surface areas), makes high density information storage devices seem like an obvious application. In addition, the materials used would also just be gold, silicon, and possibly glass. The potential lifetime of such storage devices could be hundreds (if indeed not thousands) of years, with minimal to no loss of information. Additional work would need to be done to determine the smallest writing spotsize needed for writing and readout of information. Further experiments are also needed to determine if it would be possible to encapsulate the percolation films in silicon/SiO_2 to create a sandwiched structure of multiple layers for multiplexing, like previously demonstrated with gold nanorods[9].

Secondly, the ability to manipulate wavelength and polarization sensitivity in the percolation films both on silicon and glass substrates by fs-laser writing could open new sensing applications and devices for percolation films.

The ability of the gold percolation films to also generate white light at fairly low pump powers (few tenths of mW) could also have novel applications. One aspect that also remains unstudied is how photothermal reshaping of the metal films could influence parts of the white light spectrum, by removing or adding additional plasmon resonances for certain wavelengths.

Finally, from just observing the percolation films on glass substrates after fs-laser writing, a clear red colour becomes apparent. Further investigations are needed, but potentially metal percolation films could act as cheap, large area, substrates for emerging plasmonic colour laser printing technologies.

Bibliography

[1] J. A. Schuller et al. “Plasmonics for extreme light concentration and manipulation”. In: *Nat. Mater.* 9.3 (2010), pp. 193–204.

[2] T. Y. Jeon et al. “Nanostructured plasmonic substrates for use as SERS sensors”. In: *Nano Converg.* 3.1 (2016), p. 18.

[3] Z.-W. Li et al. “Light–matter interaction of 2D materials: Physics and device applications”. In: *Chin. Phys. B* 26.3 (2017), p. 036802.

[4] T. Low et al. “Polaritons in layered two-dimensional materials”. In: *Nat. Mater.* 16 (2017), pp. 182–194.

[5] M. S. Tame et al. “Quantum plasmonics”. In: *Nat. Phys.* 9.6 (2013), pp. 329–340.

[6] M. Pelton. “Modified spontaneous emission in nanophotonic structures”. In: *Nat. Photonics* 9.7 (2015), pp. 427–435.

[7] S. I. Bozhevolnyi and N. A. Mortensen. “Plasmonics for emerging quantum technologies”. In: *Nanophotonics* 6 (2017). DOI: 10.1515/nanoph-2016-0179.

[8] A. Kristensen et al. “Plasmonic colour generation”. In: *Nat. Rev. Mater.* 2 (2016), p. 16088.

[9] P. Zijlstra, J. W. Chon, and M. Gu. “Five-dimensional optical recording mediated by surface plasmons in gold nanorods”. In: *Nature* 459.7245 (2009), p. 410.

[10] K. Kumar et al. “Printing colour at the optical diffraction limit”. In: *Nat. Nanotechnol.* 7.9 (2012), pp. 557–561.

[11] X. Zhu et al. “Plasmonic colour laser printing”. In: *Nat. Nanotechnol.* 11.4 (2016), pp. 325–329.

[12] Z. F. X. Zhu. “Plasmonics in nanostructures”. In: *Adv. Mater.* 25 (2013), pp. 3840–3856.

[13] Y. Chen. “Nanofabrication by electron beam lithography and its applications: A review”. In: *Microelectron. Eng.* 135 (2015), pp. 57–72.

[14] C.-S. Kim, S.-H. Ahn, and D.-Y. Jang. “Review: Developments in micro/nanoscale fabrication by focused ion beams”. In: *Vacuum* 86.8 (2012), pp. 1014–1035.

[15] P. Colson, C. Henrist, and R. Cloots. “Nanosphere lithography: a powerful method for the controlled manufacturing of nanomaterials”. In: *J. Nanomater.* 2013 (2013), p. 948510.

[16] A. Klinkova, R. M. Choueiri, and E. Kumacheva. "Self-assembled plasmonic nanostructures". In: *Chem. Soc. Rev.* 43.11 (2014), pp. 3976–3991.

[17] C. Xi et al. "Directed self-assembly of gold nanoparticles into plasmonic chains". In: *Soft Matter* 11.23 (2015), pp. 4562–4571.

[18] S. Gwo et al. "Nanomanipulation and controlled self-assembly of metal nanoparticles and nanocrystals for plasmonics". In: *Chem. Soc. Rev.* 45.20 (2016), pp. 5672–5716.

[19] V. M. Shalaev. *Nonlinear optics of random media: fractal composites and metal-dielectric films*. Vol. 158. Springer Tracts in Modern Physics. Heidelberg: Springer, 2007.

[20] A. Hu et al. "Femtosecond laser welded nanostructures and plasmonic devices". In: *J. Laser Appl.* 24.4 (2012), p. 042001.

[21] E. C. Garnett et al. "Self-limited plasmonic welding of silver nanowire junctions". In: *Nat. Mater.* 11.3 (2012), pp. 241–249.

[22] L. O. Herrmann et al. "Threading plasmonic nanoparticle strings with light". In: *Nat. Commun.* 5 (2014), p. 4568.

[23] J. Mertens et al. "Tracking Optical Welding through Groove Modes in Plasmonic Nanocavities". In: *Nano Lett.* 16.9 (2016), pp. 5605–5611.

[24] X. Zhu et al. "Resonant-laser-printing of structural colors on high-index dielectric metasurfaces". In: *Sci. Adv.* 3 (2017), e1602487.

[25] J. E. Greene. "Thin Film Nucleation, Growth, and Microstructural Evolution: An Atomic Scale View". In: *Handbook of Deposition Technologies for Films and Coatings*. Ed. by P. M. Martin. 3rd ed. Boston: William Andrew Publishing, 2010. Chap. 12, pp. 554–620.

[26] M. I. Stockman, L. Pandey, and T. George. "Inhomogeneous localization of polar eigenmodes in fractals". In: *Phys. Rev. B* 53.5 (1996), p. 2183.

[27] M. I. Stockman. "Inhomogeneous eigenmode localization, chaos, and correlations in large disordered clusters". In: *Phys. Rev. E* 56.6 (1997), p. 6494.

[28] D. A. Genov, A. K. Sarychev, and V. M. Shalaev. "Plasmon localization and local field distribution in metal-dielectric films". In: *Phys. Rev. E* 67.5 (2003), p. 056611.

[29] S. Ducourtieux et al. "Percolation and fractal composites: Optical studies". In: *J. Nonlinear Opt. Phys. Mater.* 9.01 (2000), pp. 105–116.

[30] A. Losquin et al. "Unveiling nanometer scale extinction and scattering phenomena through combined electron energy loss spectroscopy and cathodoluminescence measurements". In: *Nano Lett.* 15.2 (2015), pp. 1229–1237.

[31] L. Novotny and B. Hecht. *Principles of Nano-Optics*. Principles of Nano-optics. Cambridge University Press, 2012.

[32] M. Fox. *Optical Properties of Solids*. Oxford Master Series in Physics. OUP Oxford, 2010.

[33] N. Ashcroft and N. Mermin. *Solid State Physics*. Cengage Learning, 2011.

[34] S. Maier. *Plasmonics: Fundamentals and Applications*. Springer US, 2010.

[35] J. M. Enoch. "History of mirrors dating back 8000 years". In: *Optom. Vis. Sci.* 83.10 (2006), pp. 775–781.

[36] P. Drude. "Zur Elektronentheorie der Metalle". In: *Ann. Phys.* 306.3 (1900), pp. 566–613.

[37] P. Drude. "Zur Elektronentheorie der Metalle; II. Teil. Galvanomagnetische und Thermomagnetische Effecte". In: *Ann. Phys.* 308.11 (1900), pp. 369–402.

[38] G. V. Naik, V. M. Shalaev, and A. Boltasseva. "Alternative plasmonic materials: beyond gold and silver". In: *Adv. Mater.* 25.24 (2013), pp. 3264–3294.

[39] A. D. Rakić et al. "Optical properties of metallic films for vertical-cavity optoelectronic devices". In: *Appl. Opt.* 37.22 (1998), pp. 5271–5283.

[40] M. R. Beversluis, A. Bouhelier, and L. Novotny. "Continuum generation from single gold nanostructures through near-field mediated intraband transitions". In: *Phys. Rev. B* 68.11 (2003), p. 115433.

[41] P. B. Johnson and R.-W. Christy. "Optical constants of the noble metals". In: *Phys. Rev. B* 6.12 (1972), p. 4370.

[42] G. Ruthemann. "Diskrete Energieverluste mittelschneller Elektronen beim durchgang durch dünne Folien". In: *Ann. Phys.* 437.3-4 (1948), pp. 113–134.

[43] W. Lang. "Geschwindigkeitsverluste mittelschneller Elektronen beim durchgang durch dünne Metallfolien". In: *Optik* 3.3 (1948), pp. 233–246.

[44] H. Watanabe. "Experimental Evidence for the Collective Nature of the Characteristic Energy Loss of Electrons in Solids—Studies on the Dispersion Relation of Plasma Frequency—". In: *J. Phys. Soc. Jpn.* 11.2 (1956), pp. 112–119.

[45] Y. Cauchois. "Étude comparée du spectre K d'absorption de l'aluminium metallique". In: *Acta Crystallogr.* 5.3 (1952), pp. 351–356.

[46] D. Pines and D. Bohm. "A collective description of electron interactions: II. Collective vs individual particle aspects of the interactions". In: *Phys. Rev.* 85.2 (1952), p. 338.

[47] D. Bohm and D. Pines. “A collective description of electron interactions: III. Coulomb interactions in a degenerate electron gas”. In: *Phys. Rev.* 92.3 (1953), p. 609.

[48] R. H. Ritchie. “Plasma losses by fast electrons in thin films”. In: *Phys. Rev.* 106.5 (1957), p. 874.

[49] R. Ritchie and H. Eldridge. “Optical emission from irradiated foils. I”. In: *Phys. Rev.* 126.6 (1962), p. 1935.

[50] A. Otto. “Excitation of nonradiative surface plasma waves in silver by the method of frustrated total reflection”. In: *Z. Phys.* 216.4 (1968), pp. 398–410.

[51] E. Kretschmann and H. Raether. “Radiative decay of non radiative surface plasmons excited by light”. In: *Z. Naturforsch. A* 23.12 (1968), pp. 2135–2136.

[52] J. B. Khurgin. “How to deal with the loss in plasmonics and metamaterials”. In: *Nat. Nanotechnol.* 10.1 (2015), pp. 2–6.

[53] D. J. Griffiths. *Introduction to Electrodynamics*. Prentice Hall, 1999.

[54] S. A. Maier and H. A. Atwater. “Plasmonics: Localization and guiding of electromagnetic energy in metal/dielectric structures”. In: *J. Appl. Phys* 98.1 (2005), p. 10.

[55] G. M. Lerman, A. Yanai, and U. Levy. “Demonstration of nanofocusing by the use of plasmonic lens illuminated with radially polarized light”. In: *Nano Lett.* 9.5 (2009), pp. 2139–2143.

[56] A. Yanai and U. Levy. “Radiation of a uniformly moving line charge in a zero-index metamaterial and other periodic media”. In: *Opt. Express* 20.16 (2012), pp. 18515–18524.

[57] G. M. Lerman and U. Levy. “Pin cushion plasmonic device for polarization beam splitting, focusing, and beam position estimation”. In: *Nano Lett.* 13.3 (2013), pp. 1100–1105.

[58] M. Grajower et al. “Subwavelength plasmonics for graded-index optics on a chip”. In: *Opt. Lett.* 38.18 (2013), pp. 3492–3495.

[59] R. Mehfuz, M. Maqsood, and K. Chau. “Enhancing the efficiency of slit-coupling to surface-plasmon-polaritons via dispersion engineering”. In: *Opt. Express* 18.17 (2010), pp. 18206–18216.

[60] Y. Fu and X. Zhou. “Plasmonic Lenses: A Review”. In: *Plasmonics* 5.3 (2010), pp. 287–310.

[61] Z. Liu et al. “Focusing surface plasmons with a plasmonic lens”. In: *Nano Lett.* 5.9 (2005), pp. 1726–1729.

[62] P. Nordlander et al. “Plasmon hybridization in nanoparticle dimers”. In: *Nano Lett.* 4.5 (2004), pp. 899–903.

[63] L. Novotny and N. Van Hulst. “Antennas for light”. In: *Nat. Photon.* 5.2 (2011), pp. 83–90.

[64] H. Fischer and O. J. Martin. “Engineering the optical response of plasmonic nanoantennas”. In: *Opt. Express* 16.12 (2008), pp. 9144–9154.

[65] A. A. Saberi. “Recent advances in percolation theory and its applications”. In: *Phys. Rep.* 578 (2015), pp. 1–32.

[66] B. Voigtländer and M. Kästner. “Evolution of the strain relaxation in a Ge layer on Si (001) by reconstruction and intermixing”. In: *Phys. Rev. B* 60.8 (1999), R5121.

[67] A. Vailionis et al. “Pathway for the strain-driven two-dimensional to three
-dimensional transition during growth of Ge on Si (001)”. In: *Phys. Rev. Lett.* 85.17 (2000), p. 3672.

[68] J. Singh and D. Wolfe. “Review Nano and macro-structured component fabrication by electron beam-physical vapor deposition (EB-PVD)”. In: *J. Mater. Sci.* 40.1 (2005), pp. 1–26.

[69] S. Manzeli et al. “2D transition metal dichalcogenides”. In: *Nat. Rev. Mater.* 2.EPFL-REVIEW-229154 (2017), p. 17033.

[70] M. I. Stockman, L. N. Pandey, and T. F. George. “Enhanced nonlinear-optical responses of disordered clusters and composites”. In: *Nonlinear Optical Materials*. Springer, 1998, pp. 225–245.

[71] J. M. Garnett. “Colours in metal glasses, in metallic films, and in metallic solutions. II”. In: *Philosophical Transactions of the Royal Society of London A* (1906), pp. 237–288.

[72] D. J. Bergman and D. Stroud. “Physical properties of macroscopically inhomogeneous media”. In: *Solid State Phy.* 46 (1992), pp. 147–269.

[73] V. M. Shalaev and A. K. Sarychev. “Nonlinear optics of random metal-dielectric films”. In: *Phys. Rev. B* 57.20 (1998), p. 13265.

[74] F. Brouers et al. “Giant field fluctuations and characteristic lengths in optical properties of nano metal-dielectric films”. In: *Physica A* 241.1-2 (1997), pp. 146–153.

[75] F. Brouers et al. “Theory of giant Raman scattering from semicontinuous metal films”. In: *Phys. Rev. B* 55.19 (1997), p. 13234.

[76] F. Brouers, S. Blacher, and A. K. Sarychev. “Giant field fluctuations and anomalous light scattering from semicontinuous metal films”. In: *Phys. Rev. B* 58.23 (1998), p. 15897.

[77] P. Gadenne, D. Gagnot, and M. Masson. “Surface enhanced resonant Raman scattering induced by silver thin films close to the percolation threshold”. In: *Physica A* 241.1-2 (1997), pp. 161–165.

[78] D. A. Genov et al. “Local field distribution in random metal–dielectric films; theory and experiment”. In: *Physica B* 338.1 (2003), pp. 228–231.

[79] M. I. Stockman, S. V. Faleev, and D. J. Bergman. “Localization versus delocalization of surface plasmons in nanosystems: can one state have both characteristics?” In: *Phys. Rev. Lett.* 87.16 (2001), p. 167401.

[80] M. Bosman et al. “Light splitting in nanoporous gold and silver”. In: *ACS Nano* 6.1 (2011), pp. 319–326.

[81] A. Losquin et al. “Experimental evidence of nanometer-scale confinement of plasmonic eigenmodes responsible for hot spots in random metallic films”. In: *Phys. Rev. B* 88.11 (2013), p. 115427.

[82] M. I. Stockman et al. “Giant fluctuations of local optical fields in fractal clusters”. In: *Phys. Rev. Lett.* 72.15 (1994), p. 2486.

[83] M. Gaio et al. “Percolating plasmonic networks for light emission control”. In: *Farad. Discuss.* 178 (2015), pp. 237–252.

[84] S. I. Bozhevolnyi and V. Coello. “Statistics of local field intensity enhancements at nanostructured surfaces investigated with a near-field optical microscope”. In: *Phys. Rev. B* 64.11 (2001), p. 115414.

[85] J. Mertens et al. “How Light Is Emitted by Plasmonic Metals”. In: *Nano Lett.* 17.4 (2017), pp. 2568–2574.

[86] N. J. Borys, E. Shafran, and J. M. Lupton. “Surface plasmon delocalization in silver nanoparticle aggregates revealed by subdiffraction supercontinuum hot spots”. In: *Sci. Rep.* 3 (2013).

[87] T. Haug et al. “Hot-electron intraband luminescence from single hot spots in noble-metal nanoparticle films”. In: *Phys. Rev. Lett.* 115.6 (2015), p. 067403.

[88] A. Mooradian. “Photoluminescence of metals”. In: *Phys. Rev. Lett.* 22.5 (1969), p. 185.

[89] G. Boyd, Z. Yu, and Y. Shen. “Photoinduced luminescence from the noble metals and its enhancement on roughened surfaces”. In: *Phys. Rev. B* 33.12 (1986), p. 7923.

[90] J. Wilcoxon et al. “Photoluminescence from nanosize gold clusters”. In: *J. Chem. Phys.* 108.21 (1998), pp. 9137–9143.

[91] M. B. Mohamed et al. “Thelightning’gold nanorods: fluorescence enhancement of over a million compared to the gold metal”. In: *Chem. Phys. Lett.* 317.6 (2000), pp. 517–523.

[92] S. Eustis and M. El-Sayed. “Aspect ratio dependence of the enhanced fluorescence intensity of gold nanorods: experimental and simulation study”. In: *J. Phys. Chem. B* 109.34 (2005), pp. 16350–16356.

[93] M. Yorulmaz et al. “Luminescence quantum yield of single gold nanorods”. In: *Nano Lett.* 12.8 (2012), pp. 4385–4391.

[94] D. Huang et al. “Photoluminescence of a plasmonic molecule”. In: *ACS Nano* 9.7 (2015), pp. 7072–7079.

[95] T. Yin et al. “Anomalous Shift Behaviors in the Photoluminescence of Dolmen-Like Plasmonic Nanostructures”. In: *ACS Photonics* 3.6 (2016), pp. 979–984.

[96] Y. Fang et al. “Plasmon emission quantum yield of single gold nanorods as a function of aspect ratio”. In: *Acs Nano* 6.8 (2012), pp. 7177–7184.

[97] S. K. Andersen, A. Pors, and S. I. Bozhevolnyi. “Gold photoluminescence wavelength and polarization engineering”. In: *ACS Photonics* 2.3 (2015), pp. 432–438.

[98] A. Tcherniak et al. “One-photon plasmon luminescence and its application to correlation spectroscopy as a probe for rotational and translational dynamics of gold nanorods”. In: *J. Phys. Chem. C* 115.32 (2011), pp. 15938–15949.

[99] A. Otto, W. Akemann, and A. Pucci. “Normal Bands in Surface-Enhanced Raman Scattering (SERS) and Their Relation to the Electron-Hole Pair Excitation Background in SERS”. In: *Isr. J. Chem.* 46.3 (2006), pp. 307–315.

[100] J. T. Hugall and J. J. Baumberg. “Demonstrating photoluminescence from Au is electronic inelastic light scattering of a plasmonic metal: the origin of SERS backgrounds”. In: *Nano Lett.* 15.4 (2015), pp. 2600–2604.

[101] K.-Q. Lin et al. “Intraband Hot-Electron Photoluminescence from Single Silver Nanorods”. In: *ACS Photonics* 3.7 (2016), pp. 1248–1255.

[102] C. Chen, A. De Castro, and Y. Shen. “Surface-enhanced second-harmonic generation”. In: *Phys. Rev. Lett.* 46.2 (1981), p. 145.

[103] K. Iwaszczuk et al. “Terahertz-field-induced photoluminescence of nanostructured gold films”. In: *Infrared, Millimeter, and Terahertz Waves (IRMMW-THz), 2013 38th International Conference on*. IEEE. 2013, pp. 1–1.

[104] P. Mühlschlegel et al. “Resonant optical antennas”. In: *Science* 308.5728 (2005), pp. 1607–1609.

[105] M. J. Weber. *Handbook of optical materials*. Vol. 19. CRC press, 2002.

[106] Y. Zheng et al. “Hot luminescence from gold nanoflowers and its application in high-density optical data storage”. In: *Opt. Express* 25.8 (2017), pp. 9262–9275.

[107] E. Abbe. “Beiträge zur Theorie des Mikroskops und der mikroskopischen Wahrnehmung”. In: *Arch. Mikrosk. Anat.* 9.1 (1873), pp. 413–418.

[108] M. Minsky. “Memoir on inventing the confocal scanning microscope”. In: *Scanning* 10.4 (1988), pp. 128–138.

[109] S. W. Hell and J. Wichmann. “Breaking the diffraction resolution limit by stimulated emission: stimulated-emission-depletion fluorescence microscopy”. In: *Opt. Lett.* 19.11 (1994), pp. 780–782.

[110] D. W. Pohl, W. Denk, and M. Lanz. “Optical stethoscopy: Image recording with resolution $\lambda/20$”. In: *Appl. Phys. Lett.* 44.7 (1984), pp. 651–653.

[111] L. Novotny. “The history of near-field optics”. In: *Progress in optics* 50 (2007), p. 137.

[112] C. J. R. Sheppard and T. Wilson. “The Image of a Single Point in Microscopes of Large Numerical Aperture”. In: *Proc. R. Soc. A* 379.1776 (1982), pp. 145–158.

[113] J. Enderlein. “Theoretical study of detection of a dipole emitter through an objective with high numerical aperture”. In: *Opt. Lett.* 25.9 (2000), pp. 634–636.

[114] T. Fujimura et al. “Near-field optical images of ordered polystyrene particle layers and their photonic band effect”. In: *JOL* 87 (2000), pp. 954–956.

[115] B. Deutsch, R. Hillenbrand, and L. Novotny. “Near-field amplitude and phase recovery using phase-shifting interferometry”. In: *Opt. Express* 16.2 (2008), pp. 494–501.

[116] J. Hillier and R. Baker. “Microanalysis by means of electrons”. In: *J. Appl. Phys.* 15.9 (1944), pp. 663–675.

[117] D. A. Muller. “Structure and bonding at the atomic scale by scanning transmission electron microscopy”. In: *Nat. Mater.* 8.4 (2009), p. 263.

[118] F. J. García de Abajo. “Optical excitations in electron microscopy”. In: *Rev. Mod. Phys.* 82 (1 2010), pp. 209–275.

[119] R. F. Egerton. *Electron energy-loss spectroscopy in the electron microscope*. Springer Science & Business Media, 2011.

[120] R. F. Egerton. “Electron energy-loss spectroscopy in the TEM”. In: *Rep. Prog. Phys* 72.1 (2008), p. 016502.

[121] V. J. Keast and M. Bosman. “New developments in electron energy loss spectroscopy”. In: *Microsc. Res. Tech.* 70.3 (2007), pp. 211–219.

[122] V. J. Keast. “Application of EELS in materials science”. In: *Mater. Charact.* 73 (2012), pp. 1–7.

[123] D. E. Jesson and S. J. Pennycook. “Incoherent Imaging of Crystals Using Thermally Scattered Electrons”. In: *Proc. R. Soc. A* 449.1936 (1995), pp. 273–293.

[124] M. L. Brongersma, N. J. Halas, and P. Nordlander. “Plasmon-induced hot carrier science and technology”. In: *Nat. Nanotechnol.* 10.1 (2015), pp. 25–34.

[125] S. Link et al. “How long does it take to melt a gold nanorod?: A femtosecond pump–probe absorption spectroscopic study”. In: *Chem. Phys. Lett.* 315.1 (1999), pp. 12–18.

[126] S. Link, Z. L. Wang, and M. A. El-Sayed. “How Does a Gold Nanorod Melt?” In: *J. Phys. Chem. B* 104.33 (2000), pp. 7867–7870.

[127] Q. Jiang, S. Zhang, and M. Zhao. “Size-dependent melting point of noble metals”. In: *Mater. Chem. Phys.* 82.1 (2003), pp. 225–227.

[128] P. Nayebi and E. Zaminpayma. “Crystallization of Liquid Gold Nanoparticles by Molecular Dynamics Simulation”. In: *J. Cluster Sci.* 20.4 (2009), p. 661.

[129] J. Lee et al. “In situ atomic-scale observation of melting point suppression in nanometer-sized gold particles”. In: *Nanotechnology* 20.47 (2009), p. 475706.

[130] D. Moore and H. Thornton. “Effect of oxygen on the bonding of gold to fused silica”. In: *J. R. Natl. Stands.* 62.3 (1959), p. 127.

[131] R. Sangiorgi et al. “Wettability and work of adhesion of nonreactive liquid metals on silica”. In: *J. Am. Ceram. Soc* 71.9 (1988), pp. 742–748.

[132] Y. Kojima and T. Kato. “Nanoparticle formation in Au thin films by electron-beam-induced dewetting”. In: *Nanotechnology* 19.25 (2008), p. 255605.

[133] H. Huang et al. “Controlled joining of Ag nanoparticles with femtosecond laser radiation”. In: *J. Appl. Phys.* 112.12 (2012), p. 123519.

[134] V. Amendola, S. Polizzi, and M. Meneghetti. “Laser ablation synthesis of gold nanoparticles in organic solvents”. In: *J. Phys. Chem. B* 110.14 (2006), pp. 7232–7237.

[135] V. Amendola and M. Meneghetti. “Laser ablation synthesis in solution and size manipulation of noble metal nanoparticles”. In: *Physical chemistry chemical physics* 11.20 (2009), pp. 3805–3821.

[136] S. M. Novikov et al. “White light generation and anisotropic damage in gold films near percolation threshold”. In: *ACS Photonics* 4 (2017). DOI: 10.1021/acsphotonics.7b00107.

[137] A. L. Koh et al. “Electron energy-loss spectroscopy (EELS) of surface plasmons in single silver nanoparticles and dimers: influence of beam damage and mapping of dark modes”. In: *ACS Nano* 3.10 (2009), pp. 3015–3022.

Research Article Vol. 24, No. 15 | 25 Jul 2016 | OPTICS EXPRESS 16743

Optics EXPRESS

Enhancement of two-photon photoluminescence and SERS for low-coverage gold films

SERGEY M. NOVIKOV,[1,*] JONAS BEERMANN,[1] CHRISTIAN FRYDENDAHL,[2] NICOLAS STENGER,[2] VICTOR COELLO,[3] N. ASGER MORTENSEN,[2] AND SERGEY I. BOZHEVOLNYI[1]

[1] *Centre for Nano Optics,University of Southern Denmark, Campusvej 55, DK-5230 Odense, Denmark*
[2] *Department of Photonics Engineering, Technical University of Denmark, Ørsteds Plads 343, DK-2800 Kgs. Lyngby, Denmark*
[3] *CICESE Monterrey, Alianza Centro No.504 PIIT Apodaca, N. L. C. P. 66600, Mexico*
[*] *smn@iti.sdu.dk*

Abstract: Electromagnetic field enhancement (FE) effects occurring in thin gold films 3-12-nm are investigated with two-photon photoluminescence (TPL) and Raman scanning optical microscopies. The samples are characterized using scanning electron microscopy images and linear optical spectroscopy. TPL images exhibit a strong increase in the level of TPL signals for films thicknesses 3–8-nm, near the percolation threshold. For some thicknesses, TPL measurements reveal super-cubic dependences on the incident power. We ascribe this feature to the occurrence of very strongly localized and enhanced electromagnetic fields due to multiple light scattering in random nanostructures that might eventually lead to white-light generation. Raman images exhibit increasing Raman signals when decreasing the film thickness from 12 to 6-nm and decreasing signal for the 3-nm-film. This feature correlates with the TPL observations indicating that highest FE is to be expected near the percolation threshold.

© 2016 Optical Society of America

OCIS codes: (240.6680) Surface plasmons; (180.5810) Scanning microscopy; (290.0290) Scattering; (260.3910) Metal optics; (240.6695) Surface-enhanced Raman scattering; (240.3695) Linear and nonlinear light scattering from surfaces.

References and links

1. D. K. Gramotnev and S. I. Bozhevolnyi, "Plasmonics beyond the diffraction limit," Nat. Photonics **4**(2), 83–91 (2010).
2. J. A. Schuller, E. S. Barnard, W. Cai, Y. C. Jun, J. S. White, and M. L. Brongersma, "Plasmonics for extreme light concentration and manipulation," Nat. Mater. **9**(3), 193–204 (2010).
3. S. Maier, *Plasmonics: Fundamentals and Applications* (Springer, 2007).
4. S. Link, S. Lal, and N. J. Halas, "Plasmonics: nanoscale optics from sensing to waveguiding," Nat. Photonics **1**(11), 641–648 (2007).
5. J. N. Anker, W. P. Hall, O. Lyandres, N. C. Shah, J. Zhao, and R. P. Van Duyne, "Biosensing with plasmonic nanosensors," Nat. Mater. **7**(6), 442–453 (2008).
6. E. Ringe, M. R. Langille, K. Sohn, J. Zhang, J. Huang, C. A. Mirkin, R. P. Van Duyne, and L. D. Marks, "Plasmon length: an universal parameter to describe the size effects in gold nanoparticles," J. Phys. Chem. Lett. **3**(11), 1479–1483 (2012).
7. K. M. Mayer and J. H. Hafner, "Localized surface plasmon resonance sensors," Chem. Rev. **111**(6), 3828–3857 (2011).
8. F. L. Yap, P. Thoniyot, S. Krishnan, and S. Krishnamoorthy, "Nanoparticle cluster arrays for high-performance SERS through directed self-assembly on flat substrates and on optical fibers," ACS Nano **6**(3), 2056–2070 (2012).
9. J. Beermann, S. M. Novikov, O. Albrektsen, M. G. Nielsen, and S. I. Bozhevolnyi, "Surface-enhanced Raman imaging of fractal shaped periodic metal nanostructures," J. Opt. Soc. Am. B **26**(12), 2370 (2009).
10. J. Beermann, S. M. Novikov, K. Leosson, and S. I. Bozhevolnyi, "Surface enhanced Raman microscopy with metal nanoparticle arrays," J. Opt. A, Pure Appl. Opt. **11**(7), 075004 (2009).
11. A. K. Sarychev and V. M. Shalaev, "Electromagnetic field fluctuations and optical nonlinearities in metal-dielectric composites," Phys. Rep. **335**(6), 275–371 (2000).
12. L. Rodríguez-Lorenzo, J. M. Romo-Herrera, J. Pérez-Juste, R. A. Alvarez-Puebla, and L. M. Liz-Marzán, "Reshaping and LSPR tuning of Au nanostars in presence of CTAB," J. Mater. Chem. **21**(31), 11544–11549 (2011).
13. I. P. Radko, V. S. Volkov, J. Beermann, A. B. Evlyukhin, T. Søndergaard, A. Boltasseva, and S. I. Bozhevolnyi, "Plasmonic metasurfaces for waveguiding and field enhancement," Laser Photonics Rev. **3**(6), 575–590 (2009).

#267170 http://dx.doi.org/10.1364/OE.24.016743
Journal © 2016 Received 27 May 2016; revised 1 Jul 2016; accepted 8 Jul 2016; published 15 Jul 2016

14. T. W. H. Oates, H. Sugime, and S. Noda, "Combinatorial Surface-Enhanced Raman Spectroscopy and Spectroscopic Ellipsometry of Silver Island Films," J. Phys. Chem. C **113**(12), 4820–4828 (2009).
15. D. Cialla, A. März, R. Böhme, F. Theil, K. Weber, M. Schmitt, and J. Popp, "Surface-enhanced Raman spectroscopy (SERS): progress and trends," Anal. Bioanal. Chem. **403**(1), 27–54 (2012).
16. A. Balčytis, T. Tolenis, X. Wang, G. Seniutinas, R. Drazdys, P. R. Stoddart, and S. Juodkazis, "Percolation threshold gold films on columnar coatings: characterisation for SERS applications," http://www arXiv:1603.08197.
17. S. Nie and S. R. Emory, "Probing single molecules and single nanoparticles by surface-enhanced Raman scattering," Science **275**(5303), 1102–1106 (1997).
18. K. Kneipp, Y. Wang, H. Kneipp, L. T. Perelman, I. Itzkan, R. R. Dasari, and M. S. Feld, "Single molecule detection using surface-enhanced Raman scattering (SERS)," Phys. Rev. Lett. **78**(9), 1667–1670 (1997).
19. A. Shiohara, Y. Wang, and L. M. Liz-Marzán, "Recent approaches toward creation of hot spots for SERS detection," J. Photochem. Photobiol. Chem. **21**, 2–25 (2014).
20. J. P. Camden, J. A. Dieringer, Y. Wang, D. J. Masiello, L. D. Marks, G. C. Schatz, and R. P. Van Duyne, "Probing the Structure of Single-Molecule Surface-Enhanced Raman Scattering Hot Spots," J. Am. Chem. Soc. **130**(38), 12616–12617 (2008).
21. M. Moskovits, "Imaging: Spot the hotspot," Nature **469**(7330), 307–308 (2011).
22. K. Ueno, S. Juodkazis, V. Mizeikis, K. Sasaki, and H. Misawa, "Clusters of Closely Spaced Gold Nanoparticles as a Source of Two-Photon photoluminescence at Visible Wavelengths," Adv. Mater. **20**(1), 26–30 (2008).
23. G. Toscano, S. Raza, A.-P. Jauho, N. A. Mortensen, and M. Wubs, "Modified field enhancement and extinction by plasmonic nanowire dimers due to nonlocal response," Opt. Express **20**(4), 4176–4188 (2012).
24. N. A. Mortensen, S. Raza, M. Wubs, T. Søndergaard, and S. I. Bozhevolnyi, "A generalized non-local optical response theory for plasmonic nanostructures," Nat. Commun. **5**, 3809 (2014).
25. N. Gandra, A. Abbas, L. Tian, and S. Singamaneni, "Plasmonic Planet-Satellite Analogues: Hierarchical Self-Assembly of Gold Nanostructures," Nano Lett. **12**(5), 2645–2651 (2012).
26. A. Shiohara, S. M. Novikov, D. M. Solís, J. M. Taboada, F. Obelleiro, and L. M. Liz-Marzán, "Plasmon Modes and Hot Spots in Gold Nanostar–Satellite Clusters," J. Phys. Chem. C **119**(20), 10836–10843 (2015).
27. M. Gaio, M. Castro-Lopez, J. Renger, N. van Hulst, and R. Sapienza, "Percolating plasmonic networks for light emission control," Faraday Discuss. **178**, 237–252 (2015).
28. S. Ducourtieux, V. A. Podolskiy, S. Gre'sillon, S. Buil, B. Berini, P. Gadenne, A. C. Boccara, J. C. Rivoal, W. D. Bragg, K. Banerjee, V. P. Safonov, V. P. Drachev, Z. C. Ying, A. K. Sarychev, and V. M. Shalaev, "Near-field optical studies of semicontinuous metal films," Phys. Rev. B **64**(16), 165403 (2001).
29. K. Seal, D. A. Genov, A. K. Sarychev, H. Noh, V. M. Shalaev, Z. C. Ying, X. Zhang, and H. Cao, "Coexistence of Localized and Delocalized Surface Plasmon Modes in Percolating Metal Films," Phys. Rev. Lett. **97**(20), 206103 (2006).
30. S. M. Novikov, A. B. Evlyukhin, A. I. Kuznetsov, J. Beermann, B. N. Chichkov, and S. I. Bozhevolnyi, "Characterization of localized field enhancements in laser fabricated gold needle nanostructures," J. Opt. Soc. Am. B **29**(1), 185–190 (2012).
31. A. Mooradian, "Photoluminescence of metals," Phys. Rev. Lett. **22**(5), 185–187 (1969).
32. G. T. Boyd, Z. H. Yu, and Y. R. Shen, "Photoinduced luminescence from the noble metals and its enhancement on roughened surfaces," Phys. Rev. B Condens. Matter **33**(12), 7923–7936 (1986).
33. J. Beermann, S. M. Novikov, T. Søndergaard, A. Boltasseva, and S. I. Bozhevolnyi, "Two-photon mapping of localized field enhancements in thin nanostrip antennas," Opt. Express **16**(22), 17302–17309 (2008).
34. S. D. Zuani, T. Peterseim, A. Berrier, B. Gompf, and M. Dressel, "Second harmonic generation enhancement at the percolation threshold," Appl. Phys. Lett. **104**(24), 241109 (2014).
35. P. Mühlschlegel, H.-J. Eisler, O. J. F. Martin, B. Hecht, and D. W. Pohl, "Resonant Optical Antennas," Science **308**(5728), 1607–1609 (2005).
36. M. Eichelbaum, B. E. Schmidt, H. Ibrahim, and K. Rademann, "Three-photon-induced luminescence of gold nanoparticles embedded in and located on the surface of glassy nanolayers," Nanotechnology **18**(35), 355702 (2007).
37. S. Raza, S. I. Bozhevolnyi, M. Wubs, and N. Asger Mortensen, "Nonlocal optical response in metallic nanostructures," J. Phys. Condens. Matter **27**(18), 183204 (2015).
38. A. V. Krasavin, P. Ginzburg, G. A. Wurtz, and A. V. Zayats, "Nonlocality-driven supercontinuum white light generation in plasmonic nanostructures," Nat. Commun. **7**, 11497 (2016).
39. P. J. Schuck, D. P. Fromm, A. Sundaramurthy, G. S. Kino, and W. E. Moerner, "Improving the mismatch between light and nanoscale objects with gold bowtie nanoantennas," Phys. Rev. Lett. **94**(1), 017402 (2005).
40. E. C. Le Ru, E. Blackie, M. Meyer, and P. G. Etchegoin, "Surface Enhanced Raman Scattering Enhancement Factors: A Comprehensive Study," J. Phys. Chem. C **111**(37), 13794–13803 (2007).
41. D. P. Fromm, A. Sundaramurthy, A. Kinkhabwala, P. J. Schuck, G. S. Kino, and W. E. Moerner, "Exploring the chemical enhancement for surface-enhanced Raman scattering with Au bowtie nanoantennas," J. Chem. Phys. **124**(6), 061101 (2006).

1. Introduction

Light interaction with nanostructures and nanostructured materials gives rise to various fascinating optical phenomena occurring at the nanoscale [1]. One of the directions of research in nano-optics is the search for structure configurations that efficiently interconvert propagating and strongly localized optical fields and thereby promote strongly enhanced local fields [2]. The field enhancement (FE) occurs due to the resonantly excited collective electron oscillations [3,4]. Resonant interactions in metal nanostructures involving localized as well as propagating surface plasmons, i.e., surface plasmon-polariton (SPP) modes, have been investigated using colloid metallic nanoparticles (NPs) of various sizes and shapes [5–7], particle ensembles [8] with pre-determined optical properties, and periodic [9,10] and random [11] nanostructures. The spectral position of resonances can be tuned through a variety of parameters such as geometry, composition of nanostructures or size and shape of NPs [12]. These structures or NPs represented well-defined regular configurations exhibiting resonant FE at one or several wavelengths [5–10] or irregular random nanostructures featuring (spatially separated) resonant excitations covering a wide spectrum range [11]. The strong FE is extremely important for practical applications such as sensors [5,7] or micro-optical devices [13] and plays a major role in surface-enhanced Raman scattering (SERS) [9,10,14–16]. SERS is a powerful and highly selective tool to chemically identify and determine the structure of materials and molecules, on the basis of their specific vibrational bonds. Strong SERS effects obtained using nanoplasmonic structures or NPs allows the detection of molecules at extremely low concentrations, down to a single molecule level [17,18]. One way to reach a high FE is to create structures with well-known “hot spots” [18–22]. These so-called hot spots are created at interparticle gaps near 1-3 nm. If gaps turn sub-nanometric, then nonlocal effects start limiting the FE levels [23,24].

There are various strategies for the realization of hot spots, e.g., aggregation of NPs, satellite-systems [25,26], nanostructures fabricated by electron-beam lithography (EBL), and focused ion beam (FIB) milling. However, colloids aggregation is unpredictable random process that leads to alternating Raman enhancement and decreased reproducibility. On the other hand, the EBL and FIB are methods that offer high reproducibility, but these methods are limited to roughly 10 nm gap sizes and require rather costly equipment, thus hindering low-cost and large scale production. After all, the main requirements for SERS substrates are not only high reproducibility and robust fabrication procedure, but also large-area homogeneity, low cost, and possibility for mass production. One route for the fabrication of large-area structures with “hot spots” could be realized with the semi-continuous metallic films [27–29]. These films can be obtained by evaporation of noble metals like gold or silver onto a dielectric or semiconductor substrate. In the beginning of the deposition procedure the “film” consists of separated clusters that grow monotonically in size and with irregular shapes as the amount of deposited gold increases. The clusters tend to grow faster along the substrate plane than in height. As the coverage increases and the deposited gold clusters are beginning to merge together, forming a labyrinthine structure where plasmonic “hot spots” occur for specific thicknesses where the clusters do not form a continuous film, while the distance between clusters is minimal. Using electron-beam deposition it is possible to fabricate structures covering rather large, up to wafer size, areas.

In this work, we experimentally investigate electromagnetic field enhancement effects occurring in thin gold films during their transition from low-coverage (island-like) films, where gold clusters are well separated, to intermediate films near the percolation threshold and, finally, to relatively thick films exhibiting (close to) bulk properties. We anticipate that the results reported in this manuscript will be interesting for applications of various surface-enhanced spectroscopies, in general, and SERS applications (in bio- and molecular sensing and identification), in particular.

2. Fabrication and linear spectroscopy

Thin gold films at different thicknesses were deposited with electron-beam evaporation at a vacuum chamber pressure of 10^{-5} mbar, and a deposition rate of 2 Å/s, onto the room temperature glass (borosilicate) substrates. The films were fabricated with the nominal thicknesses 3, 6, 8, 10, and 12 nm and were subsequently imaged by scanning electron microscopy (SEM) [Fig. 1]. The 3 nm film exhibits separate clusters [Fig. 1(a)], whereas with increasing thickness until 6 and 8 nm, the clusters form labyrinthine structure [Fig. 1(b) and (c)], and finally almost continuous films for thickness 10 and 12 nm [Fig. 1(d) and (e)].

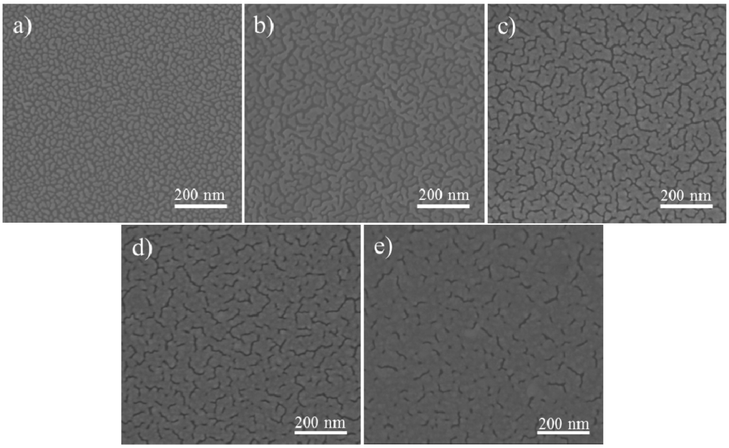

Fig. 1. SEM images of thin Gold films with nominal thicknesses of a) 3nm, b) 6 nm, c) 8 nm, d) 10 nm, and e) 12 nm deposited by electron-beam evaporation on glass substrates.

We emphasize that for the gold films, the quoted "thickness" is the average nominal coverage measured by the quartz oscillator and we estimate variations of the order of ± 0.5 nm across the wafer. Reflection and transmission spectroscopy [Fig. 2] was performed prior to TPL measurements and before covering the sample with the Raman active dye Crystal Violet (CV). Our experimental setup for reflection and transmission spectroscopy has been described previously [9,10,30]. The spectroscopic reflection and transmission analysis were performed on a BX51 microscope (Olympus) equipped with a halogen light source, polarizers and a fiber-coupled grating spectrometer QE65000 (Ocean Optics) with a wavelength resolution of 1.6 nm. The reflected and transmitted light was collected using an MPlanFL (Olympus) objective with magnification × 100 (NA = 0.9). The image area analyzed by the spectrometer is limited by a pinhole with a diameter of 150 μm resulting in a circular probing area with a diameter of 1.5 μm. The experimental data in Fig. 2(a) represent the reflection ratio R_{str}/R_{ref}, where R_{str} is the reflection measured from the films and R_{ref} is the reference spectrum recorded from a bulk optically-smooth gold surface. The experimental data in Fig. 2(b) represent the transmission ratio T_{str}/T_{ref}, where T_{str} is the reflection measured from the films and T_{ref} is the reference spectrum recorded from a bare glass substrate. As expected intuitively, the reflectivity of the films increases with nominal thickness, while the transmission decreases [Fig. 2].

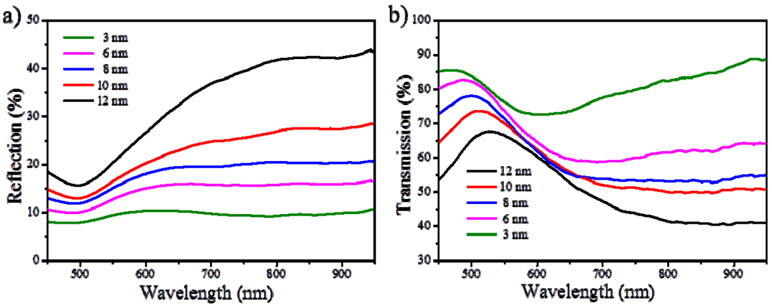

Fig. 2. a) Reflection and b) transmission spectra obtained for the thin gold films with nominal thicknesses of 3 nm, 6 nm, 8 nm, 10 nm, and 12 nm and normalized as explained in the text.

It is seen that, except for the lowest nominal thickness of 3 nm, the spectra do not reveal specific resonances. The reflection spectra resemble those of bulk gold, with the spectral features becoming more pronounced for increasing thicknesses. For the film with thickness 3 nm, the reflection/transmission has a broad peak/dip at ~550-650 nm, which can be explained by local surface plasmon resonances (LSPRs) in clusters with sizes of 10-40 nm [Fig. 1(a)]. At the same time, the peak is inhomogenously broadened, i.e. less pronounced, since the ensemble of clusters have random shapes different heights and orientations.

3. TPL and Raman spectroscopy

Characterization of the FE effects in the fabricated gold films is conducted using TPL [31–33] and Raman microscopy.

3.1 Two photon-excited photoluminescence (TPL) microscopy

The setup consists of a scanning optical microscope in reflection geometry built on the basis of a commercial microscope and a computer-controlled translation stage. The linearly polarized light beam from a mode-locked pulsed (pulse duration ~200 fs, repetition rate ~80 MHz) Ti- Sapphire laser (wavelength $\lambda = 730 - 860$ nm, $\delta\lambda$ ~10 nm, average power ~300 mW) is used as an illumination source at the fundamental harmonic (FH) frequency. After passing an optical isolator (to suppress back-reflection), half-wave plate, polarizer, red color filter and wavelength selective beam splitter, the laser beam is focused on the sample surface at normal incidence with a Mitutoyo infinity-corrected objective (× 100, N.A. = 0.70). The half-wave plate and polarizer allow accurate adjustment of the incident power. TPL radiation generated in reflection and the reflected FH beam are collected simultaneously with the same objective, separated by the wavelength selective beam splitter, directed through the appropriate filters and detected with two photomultiplier tubes (PMTs). The tube for TPL photons (within the transmission band of 350-550 nm) is connected with a photon counter giving typically only ~20 dark counts per second (cps). The FH and TPL spatial resolution at full-width-half-maximum is ~0.75 μm and ~0.35 μm, respectively, which means no individual clusters will be resolved in the TPL images. In this work, we used the following scan parameters: the integration time (at one point) of 50 ms, scanning speed (between the measurement points) of 20 μm/s, scanned area of 10 × 10 μm^2, and scanning step size of 350 nm. We adjusted the incident power P within the range 0.3-1 mW in order to obtain significant TPL signals and record the TPL signal dependence on the incident powers. For bulk gold references (both electron-beam deposited and grown single crystalline substrates), we confirmed that obtained TPL signals depend quadratically on the incident power. For these measurements we kept for simplicity the excitation wavelength fixed at 740 nm, since there are no specific resonances Fig. 2 at this wavelength and 740 nm is more visible and convenient to focus. The typical TPL image [Fig. 3(a)] reveals homogeneous signal from the scanned area.

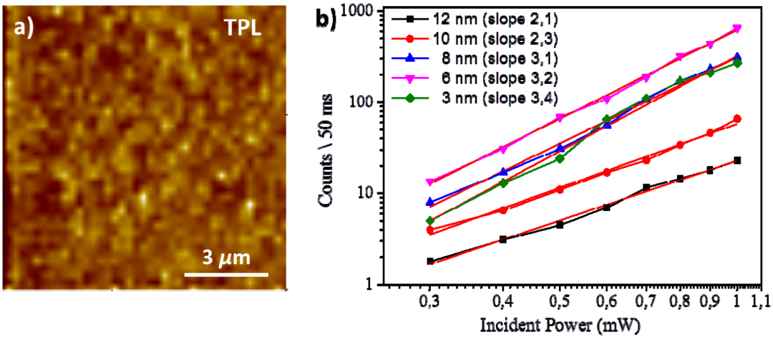

Fig. 3. a) Typical TPL image from the thin gold films, obtained here for 6 nm thickness. (Signal levels at bright spots are typically larger by 30-40% than the average TPL signal). b) Dependence of TPL signal on the power for the thicknesses 3, 6, 8, 10, and 12 nm. The log/log curves are shown with a linear curve fit and slope-values in the legend illustrate the super-cubic signal dependence on incident power.

The TPL measurements show strong TPL signal, which increases with increasing nominal film thicknesses from 3 to 6 nm. For further increase of the film thickness to 8 nm, the TPL signal is again similar to that at 3 nm and dramatically decreases for the thicknesses 10 and 12 nm [Fig. 3(b)]. The remarkable increase of TPL signal can be explained by the coverage approaching the percolation threshold of the gold films. It is important to note that the nominal thickness at which the percolation threshold occurs, depends somewhat on the deposition conditions. We did not perform specific conductivity measurements, which could uniquely indicate the thickness at percolation threshold, but visual analysis of SEM images, clearly indicate that the thickness 3 nm is below, 8-12 nm are above, while 6 nm is in the close vicinity of the percolation threshold [Fig. 1]. It is reasonable that the TPL signal increases for 6 nm thickness as it correlates with the many nano-gaps and -cracks in the film at which hot spots could form [Fig. 1(b)]. With the formation of a continuous film, the number of hot spots significantly reduces and the gold coverage approaches that of a smooth layer [Fig. 1(d) and (e)]. The TPL signal for the 12 nm thickness decreases dramatically compared with that for 6 nm. Meanwhile, the level of TPL signal for the 12 nm film is still above that from the surface of the bulk gold references. The reason is, as was noted above for the thin films, that the film thicknesses is only an average measure. It means that roughness is present not only in the horizontal plane but also in the vertical plane [14,34]. However, we would like to stress that a strongly focused beam will actually also contain z-polarized components, facilitating excitation of longitudinal modes associated with this roughness. The variation of observed TPL signal across the sample was ~15-20% for the thicknesses 3, 6, 8 nm and ~10% for the 10, 12 nm films.

As mentioned above the slope of TPL power dependence should be two, but for some thicknesses [Fig. 3(b)], the TPL-measurements show a non-linear signal with a higher than cubic dependence on incident power. A possible explanation of this higher incident power dependence is supercontinuum white-light generation in the sample [35,36], possibly driven by non-local electron response [37] in the complex geometric shapes of the semi-continues plasmonic nanostructures [38]. It is very important, since it indicates the presence of strong electric fields. Experimentally, the level of TPL enhancement can be objectively evaluated by taking into account the area and incident power producing the TPL signal [39]. The intensity enhancement factor (EF) can be calculated using the following relation:

$$\alpha = \sqrt{\frac{S_{str} \langle P_{ref} \rangle^2 A_{ref}}{S_{ref} \langle P_{str} \rangle^2 A_{str}}} \tag{1}$$

where, S is the obtained TPL signal, $< P >$ is the average incident power, and A is the TPL source area within the FH focus spot (diameter ~0.75 μm) producing the enhancement. Using Eq. (1), the intensity enhancement was estimated for the Gold films as ~14 (12 nm), ~28 (10 nm), ~66 (8 nm), ~96 (6 nm) and ~60 (3 nm). However, these estimations are rather rough as they do not take into account a more detailed ratio between areas, since for the clusters and semi-continues gold it is difficult to accurately evaluate the smaller TPL source area, which would lead to higher FE estimates. Moreover, for such thin films with thicknesses less than the skin depth, not only the source area but also its volume start to play a role, making estimation further complicated. Even if it is possible by a software and SEM images to get an improved estimate of the source area, the film thickness is only an average measure and we cannot be sure of the contributing volume. On the other hand, in the above estimate we did not take into account that the power dependence of the obtained signal is more than quadratic, which would lead to significantly lower FE estimates. The careful calculation for 6 nm thickness with an area reduction, e.g., $A_{str} \sim (40 \times 40\ nm^2) \sim 1/240\ A_{ref}$ and accurate power dependence ~3.2, gives the same FE estimation, and it is clear even from these rough estimates that the easily fabricated substrates still provide rather high and interesting FE effects. In the light of Ref [38]. we speculate that the high FE and the nonlinear response could be associated with nonlocal dynamics.

3.2 Surface enhanced Raman spectroscopy

After obtaining the reflection/transmission spectra and TPL characterization, directly before the Raman measurement, the samples were covered by an ethanol 10^{-6} M solution of Crystal Violet dye. This Raman active dye was chosen as it has well characterized properties, and moreover CV is not resonant at our excitation wavelength (absorption line ~590 nm) and it is relatively stable. The non-resonant Raman characterization helps us prevent the strong fluorescence which can sometimes completely dominate the Raman spectra and influence the enhancement estimation. For these experiments the concentration of CV adsorbed at the sample surface is not really important, since we primarily want to combine our understanding of electromagnetic FE with Raman microscopy, using CV dye and the SERS spectral shape for probing of the thin Gold films. The experimental setup used for Raman microscopy is the commercially available confocal scanning Raman microscope (Alpha300R) from Witec and measurements were obtained using linearly polarized excitation of wavelength 532 nm, 600 lines/mm diffraction grating, and × 100 objective (N.A. = 0.90), whereas we use unpolarized detection in order to have a significant signal to noise ratio. Detailed SERS images were formed by mapping the spatial dependence of SERS intensity integrated around the main Raman peaks within the shift range 1560-1650 cm^{-1} for each of the 28 × 28 points (step size 350 nm) in the scan. We used an incident power of P~0.08 mW, and an integration time of 500 ms for each points [Fig. 4(a)].

These scan-parameters were selected as a compromise between minimum damage/bleaching of the dye molecules and significant signal to noise ratios. Typical SERS images show homogeneous signal across the isotropic sample [Fig. 4(a)]. In this connection, we should stress that for all thicknesses, both TPL and SERS images appear very homogenous. Signal levels at bright spots that we observed [Figs. 3(a) and 4(a)] are typically larger by 30-40% than the average TPL signal and by 10-15% than the average SERS signal. We did not observe any *extremely* bright spots, even for thickness close to percolation threshold where the average signal is high.

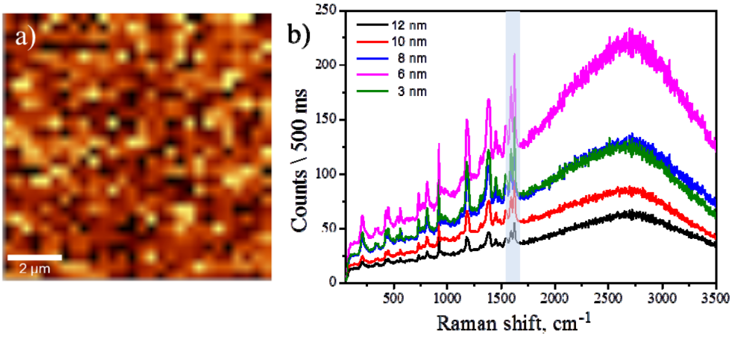

Fig. 4. a) Typical SERS image obtained for the thin Gold films, obtained here for 6 nm thickness. (Signal levels at bright spots larger by 10-15% than the average SERS signal). b) SERS spectra of CV with concentration 10^{-6}M for all thicknesses (3, 6, 8, 10, and 12 nm). The shaded column indicates the range used for SERS imaging in a).

Typical SERS spectra obtained from the thin gold films show that the SERS intensity and fluorescence increases for nominal thicknesses from 3 to 6 nm and then decrease again for 8 nm and continue to decrease for the 10 and 12 nm. Analysis of SEM images explain this behavior as in the case of the 3 nm film thickness [Fig. 1(a)] the gold clusters have sizes ranging from 10 to 40 nm and shapes close to hemi-spheres or elongated rods, with their own LSPRs. The nearest neighbors distance between these clusters is 5-15 nm. The strong SERS originates from LSPRs of these clusters and for this thickness the cluster size and form is important. The increased intensity of the SERS spectra obtained from the film with 6 nm thickness corresponds to increased FE due to a decreased gap between the clusters [Fig. 1(b)]. For this thickness, clusters grow and coalesce into oblong formation of about 20 nm wide and 80-120 nm long. The distance between the nearest neighbors is 15 nm in wide areas and reduces to 1-3 nm in narrow gaps. Some clusters form continuous chains. This happens at a thickness close to percolation threshold and leads to so-called “hot spots” in the nano-gaps between clusters and resulting in an increased SERS signal. With further increasing thickness until 8 nm the size of the clusters increases [Fig. 1(c)], and the amount of “hot spots” decreases. The clusters merge into a labyrinthine structure, hot spots disappear and the roughness of this labyrinthine structure becomes important. For film thicknesses of 10 and 12 nm, the surface looks almost as a homogeneous film. However, since the films with 10 and 12 nm deposition still has some surface roughness, the SERS signal is still present. It should be mentioned that in our previous works we have evaluated the intensity enhancement as the direct ratio between the signal of a reference (obtained signal form the smooth bulk gold film) and the main Raman peaks from dye adsorbed on the structures [9,10]. In the present case, we could not use this method since, with the dye deposited at the same concentration, it was not possible to get a Raman signal on smooth gold. For the calculation of enhancement, we use the analytical EF expression which quantifies how much more signal can be expected from SERS in comparison with normal Raman for the same experimental parameters [40]. The average EF was determined by comparing the signals acquired from CV at a concentration of 5×10^{-2} M on a glass substrate, with the signals obtained from 10^{-6} M of CV on the thin gold films. The EF was calculated using the following relation:

$$EF = \frac{I_{SERS}}{I_{ref}} \frac{C_{ref}}{C_{SERS}}, \tag{2}$$

where I_{SERS} and I_{ref} represent background-subtracted intensities of the 1626 cm^{-1} band (being the most intense band) for CV adsorbed on the thin gold films and on the glass substrate, respectively. C_{SERS} and C_{ref} represent the corresponding concentrations of CV on these different substrates. The average EF of these thin gold films were estimated to be ~0.85 × 10^4 (3 nm), ~1.07 × 10^4 (6 nm), ~0.63 × 10^4 (8 nm), ~0.45 × 10^4 (10 nm), and ~0.25 × 10^4 (12 nm), respectively. We would like to stress that in this case that we have used non-resonant dye at the excitation wavelength, whereas for the resonant case the enhancement estimation would be one or two order of magnitude higher. In addition, although the investigated semi-continuous gold films do not provide as strong enhancements factors as reported for other specifically prepared gold structure configuration [5], our surfaces qualify as intermediate simple and large-scale fabricated SERS substrates. At the 532 nm excitation wavelength used for SERS imaging, the SPPs have considerably shorter propagation lengths of only a few micrometers, but at the same time this excitation wavelength is close to the LSPR of the individual clusters. Furthermore, one should note that in addition to the different excitation wavelengths there is also a fundamental difference between using TPL and SERS for the FE estimation. Here, TPL originates from the gold structure itself (contribution from the bulk), whereas SERS is from the part of analyte located close to the surface with strong fields and near or in hot spots, and in addition, there is a chemical enhancement [41], present due to chemical interactions between analyte and the gold film itself.

4. Summary

In conclusion, we have investigated the scattering properties and the local FE of 3, 6, 8, 10, 12 nm thin gold films using reflection and transmission spectroscopy, nonlinear two-photon photoluminescence scanning optical microscopy, and Raman microscopy. The reflectivity of the semi-continuous films increases with nominal thickness, while the transmission decreases. The extremely strong and homogeneous TPL-signal was observed across the sample close to the percolation threshold, for a thickness of 6 nm, and a decreasing signal for further increasing nominal thickness. For thicknesses of 3, 6 and 8 nm, the TPL-measurement shows a non-linear signal with a higher than cubic dependence on incident power, rather than the quadratic dependence expected from regular TPL-measurements. Such strong power dependence could be related to super-continuum white-light generation involving various high-order nonlinear processes and it is an important signature of strong FE. For the Raman measurements, the samples were covered with 10^{-6} M concentration of Crystal Violet dye, which is non-resonant at the excitation wavelength of 532 nm. The SERS thickness dependence follows a similar trend as observed for the TPL investigation, with an increasing Raman signal for the 6 nm thickness, indicating how SERS enhancement is promoted near the percolation threshold. We believe that these easy-to-fabricate and scalable semi-continuous metallic films constitute a practical alternative for designing SERS substrates to be employed in the single-molecule detection and that the possibility for supercontinuum white-light generation in the percolation geometry should be investigated further, using also spectral and time-resolved measurements.

Acknowledgments

The authors gratefully acknowledge financial support from CONACyT Basic Scientific Research Grant 250719 and the University of Southern Denmark (SDU2020 funding).

192.38.89.49 {ts '2017-05-31 10:42:46'}

ACS Photonics

Article

pubs.acs.org/journal/apchd5

White Light Generation and Anisotropic Damage in Gold Films near Percolation Threshold

Sergey M. Novikov,[†] Christian Frydendahl,[‡,§] Jonas Beermann,[†] Vladimir A. Zenin,[†] Nicolas Stenger,[‡,§] Victor Coello,[∥] N. Asger Mortensen,[‡,§] and Sergey I. Bozhevolnyi*,[†]

[†]Centre for Nano Optics, University of Southern Denmark, Campusvej 55, DK-5230 Odense, Denmark

[‡]Department of Photonics Engineering and [§]Center for Nanostructured Graphene, Technical University of Denmark, DK-2800 Kongens Lyngby, Denmark

[∥]CICESE Monterrey, Alianza Centro No. 504 PIIT, Apodaca, N. L. C. P. 66600, Mexico

Supporting Information

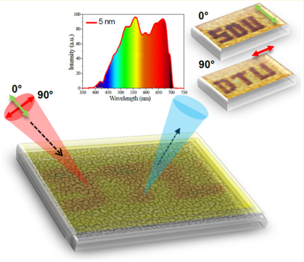

ABSTRACT: Strongly enhanced and confined electromagnetic fields generated in metal nanostructures upon illumination are exploited in many emerging technologies by either fabricating sophisticated nanostructures or synthesizing colloid nanoparticles. Here we study effects driven by field enhancement in vanishingly small gaps between gold islands in thin films near the electrically determined percolation threshold. Optical explorations using two-photon luminescence (TPL) and near-field microscopies reveals supercubic TPL power dependencies with white-light spectra, establishing unequivocally that the strongest TPL signals are generated close to the percolation threshold films, and occurrence of extremely confined (~30 nm) and strongly enhanced (~100 times) fields at the illumination wavelength. For linearly polarized and sufficiently powerful light, we observe pronounced optical damage with TPL images being sensitive to both wavelength and polarization of illuminating light. We relate these effects to thermally induced morphological changes observed with scanning electron microscopy images. Exciting physics involved in light interaction with near-percolation metal films along with their straightforward and scalable one-step fabrication procedure promises a wide range of fascinating developments and technological applications within diverse areas of modern nanotechnology, from biomolecule optical sensing to ultradense optical data storage.

KEYWORDS: *field enhancement, surface plasmons, scanning microscopy, metal optics, linear and nonlinear light scattering from surfaces, phase-resolved near-field microscopy*

Illumination of metal nanostructures results in nanostructured optical fields that are strongly enhanced and localized in the vicinity of sharp corners and in nanometer sized gaps between metal surfaces.[1] While diverse field enhancement (FE) effects can be realized by dedicated design and high-resolution (often rather sophisticated) nanofabrication,[2] intriguing optical properties, including FE-driven linear and nonlinear effects, can be found in thin semicontinuous films near the percolation threshold,[3] the critical point at which individual metal clusters start forming connected structures across the substrate domains.[4−7] These films can be obtained by simple and straightforward metal deposition, for example, thermal evaporation, onto a dielectric or semiconductor substrate. As the average film thickness increases during the metal deposition, individual and well-separated metal islands extend their sizes, eventually forming near the percolation threshold a semicontinuous film that gradually evolves into a homogeneous smooth film exhibiting (close to) bulk properties.[7] The percolation threshold can experimentally be observed by monitoring FE effects with optical methods[3−5,8] and uniquely determined in the low-frequency regime through electric conductivity measurements.[9,10] It should also be noted that the average film thickness corresponding to the percolation threshold depends strongly on the deposition conditions, substrate material, and metal involved.[11,12]

Considerable interest in semicontinuous metal films near the percolation threshold is primarily motivated by their remarkable ability of generating (under illumination) strongly enhanced local electromagnetic fields, so-called "hot-spots",[13−16] that can be observed directly with near-field microscopy techniques[5] and indirectly via strongly enhanced nonlinear optical interactions.[3,7,9] Typically, hot spots are associated with FEs occurring in nm-sized gaps between metal surfaces of nanoparticles (NPs), clusters, or specifically designed nanostructures, with nonlocal effects becoming significant for subnanometer gaps where they limit the FE levels[17,18] with far-reaching implications also for the nonlinear dynamics.[19−22] Strong FE effects in metal nanostructures primarily occur due to resonantly excited surface plasmons

Received: February 3, 2017
Published: April 6, 2017

© 2017 American Chemical Society

DOI: 10.1021/acsphotonics.7b00107
ACS Photonics 2017, 4, 1207−1215

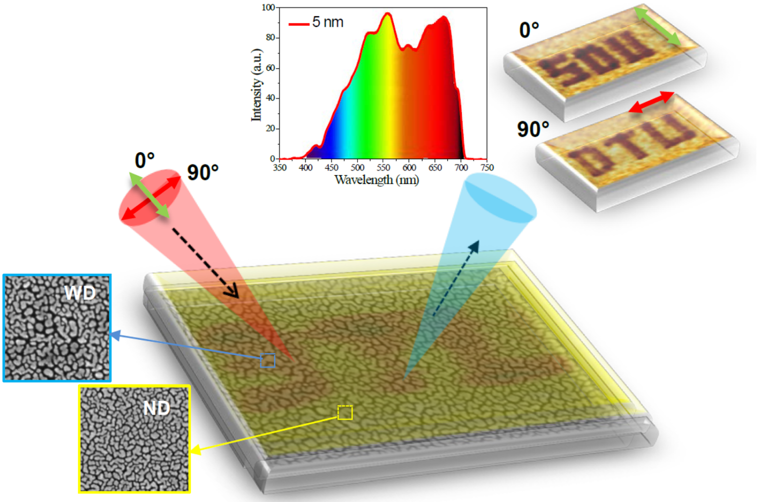

Figure 1. Schematics of the phenomena observed in the photoluminescence experiments with thin near-percolation gold films. Strong local field enhancements occurring upon illumination with a powerful fs-pulsed laser beam result in local melting and reshaping as illustrated with 500 × 500 nm^2 SEM images showing damaged (WD) and undamaged (ND) areas. A damaged pattern can be observed in the TPL images obtained with a weak probe beam polarized similarly to the strong laser beam used for producing the damage. Strong field enhancements lead also to transforming the TPL spectrum into that typical for white light generation.

(SPs), that is, collective electron oscillations in metals coupled to electromagnetic fields in dielectrics.[1−3,23−25] Resonant interactions in metal nanostructures involving localized as well as propagating SPs have been investigated using colloidal metallic NPs of various sizes and shapes,[25−28] NP ensembles[29,30] with predetermined optical properties and periodic[31−33] and random[34] nanostructures. The spectral position of resonances is tunable through a variety of parameters such as metal, geometry, composition of nanostructures, or size and shape of NPs.[24−26,35,36] These artificial nanostructures and NPs represent well-defined regular configurations exhibiting resonant FE at one or several wavelengths[26−29,31,32] or irregular random nanostructures hosting (spatially separated) resonant excitations covering a wide spectral range.[34]

One signature of extremely strong electric fields in metal nanostructures is white-light generation, first observed with resonant optical nanoantennas.[37] Strong FEs are extremely important for both fundamental studies within an emerging field of quantum plasmonics[4,38−40] and practical applications such as sensors,[26,28] playing a major role in surface-enhanced spectroscopies, including surface-enhanced Raman scattering (SERS).[31,41−43] Another interesting application of strong FE effects is pulsed-laser-induced color changes of aluminum disk-hole resonances[44] and optical recording in gold nanorod solutions mediated by local plasmonic heating and melting.[45,46] It should however be noted that widely used colloids of NPs, for example, nanorods, could aggregate during their deposition on a sample surface, leading to strong variations in optical properties over the sample surface and thereby decreased reproducibility. At the same time, electron-beam lithography (EBL) and focused ion-beam (FIB) milling techniques that do offer high reproducibility, feature limited (∼10 nm) spatial resolutions, limiting thereby achievable FE levels, and require rather costly equipment, thus, hindering low-cost and large-scale production. Alternatively, semicontinuous metal films near the percolation threshold can quite easily be fabricated by evaporation of metals like gold or silver onto a dielectric or semiconductor substrate. Using electron-beam deposition, it is possible to fabricate structures covering rather large, up to wafer size, areas in only a few minutes. Two-photon luminescence[47,48] (TPL) microscopy is a powerful tool for characterizing FE effects,[49] and we have recently observed significant FE effects by conducting TPL and SERS experiments with thin gold films during their transition from low-coverage (island-like) to continuous films.[7]

In the present work, by carefully mapping of this transition with parallel TPL microscopy and electrical conductivity characterization, we demonstrate unequivocally that TPL signals reach maximum levels at the percolation threshold, featuring supercubic power dependencies with white-light spectra similar to those obtained with extreme FEs in plasmonic nanoantennas.[37] Moreover, for linearly polarized and sufficiently powerful light, we observe pronounced optical damage with subsequent TPL images being sensitive to both wavelength and polarization of the illuminating light (Figure 1). We relate the polarization and wavelength sensitivity of optical damage to thermally induced morphological changes (at locations of extreme FEs) observed with scanning electron microscopy (SEM). Finally, using phase- and amplitude-resolved near-field imaging of near-percolation films, we directly demonstrate the occurrence of extremely confined and enhanced fields at the illumination wavelength with the FE being both polarization and wavelength dependent. Near-field images allow us to elucidate the underlying physical mechanisms involved in the observed TPL phenomena and evaluate the high FE levels achieved in our experiments.

DOI: 10.1021/acsphotonics.7b00107
ACS Photonics 2017, 4, 1207−1215

RESULTS AND DISCUSSION

TPL Enhancement and White Light Generation. Thin gold films with thicknesses ranging from 2 to 11 nm were deposited onto room-temperature glass substrates (see Methods). A subset of films (with thicknesses of 3, 5, 7, and 9 nm) was also prepared on 18 nm thin SiO_2 membranes for transmission electron microscopy (TEM) imaging (Figure 2a−d). It should be noted that the thickness of gold films specified throughout this work is the average nominal coverage measured by a quartz oscillator, and variations of the order of ±0.5 nm across a 4″ wafer are expected. Very thin films with thicknesses of up to 3 nm consist of well-separated islands (Figure 2a), whereas those with larger thicknesses, from 5 to 7 nm, feature labyrinthine structures (Figure 2b,c). Finally, films become practically continuous for the thickness of 9 nm (Figure 2d). Prior to TPL investigations, the fabricated samples are characterized by linear reflection spectroscopy.

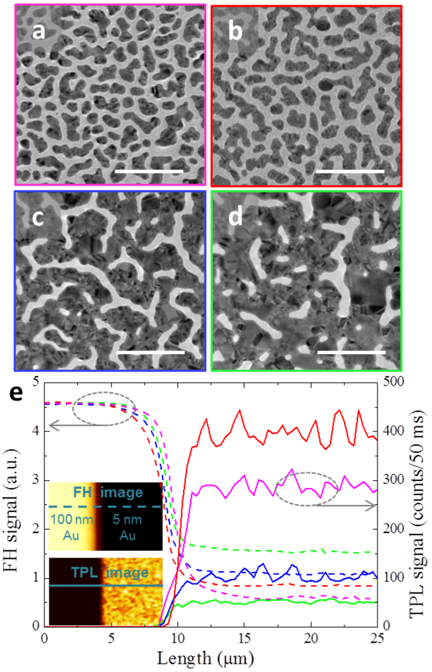

Figure 2. TEM images of thin (near-percolation) gold films with nominal thicknesses of (a) 3, (b) 5, (c) 7, and (d) 9 nm. Dark gray corresponds to the gold. The scale bars are 100 nm. (e) Cross sections of FH (dashed line) and TPL signals (solid line) across the border of bulk gold and thin gold film with nominal thicknesses of 3 (magenta), 5 (red), 7 (blue), and 9 nm (green). The average incident power was ∼0.4 mW. Insets: typical FH (upper) and TPL (lower) images, with lines indicating the orientation of cross sections.

As expected intuitively, the film reflectivity increases gradually and monotonously with nominal film thickness, without revealing any specific resonances in the frequency range of interest (Figure S1a). Characterization of the FE effects in thin gold films is then conducted using the TPL microscopy and spectroscopy (see Methods). In passing, we note that, in all configurations considered here, TPL signals disappear completely after switching a pump laser from fs-pulsed to continuous operation mode, a clear signature of the nonlinear origin of the investigated phenomenon. To compare thin films with bulk gold, we fabricated a complementary set of samples, where thin gold films are evaporated onto a glass substrate, half of which was initially coated (by evaporation) with a 100 nm thin gold film, referred hereafter to as bulk gold. For simplicity, we kept the same excitation wavelength of 740 nm in these measurements, since there are no specific resonances at this wavelength and 740 nm is better visible and convenient for alignment. Cross sections of scanning optical microscopy maps across the boundary between bulk gold and thin gold films, obtained simultaneously with a band-pass filter at the illumination wavelength (noted as the fundamental harmonic, FH) and with a low-pass filter transmitting only the TPL signals, reveal significantly different optical responses (Figure 2e).

As expected, the level of FH signals from the bulk gold is the same for all samples, whereas the level of FH signals from thin films decreases with a reduction of thickness (in accordance with the thickness-dependent linear optical spectra shown in Figure S1a). Contrary to that, the TPL signals from thin films are significantly higher than those from the bulk gold, depending nonmonotonically on the film thickness (in accordance with the thickness-dependent TPL spectra shown in Figure S1c,d). The strongest TPL signals are observed with the 5 nm thin film, being ∼10× higher than those for the 9 nm thin film, which exhibits a very weak and rather homogeneous TPL response (as expected for thick films approaching bulk gold in their optical properties). The TPL response from the 5 nm thin film features noticeable oscillations at the level of ∼10% (Figure 2e), indicating that the TPL sources, which are expected to originate from subwavelength-sized hot spots, differ in strength and are randomly distributed over the film area. These features are also corroborated with near-field optical images and their analysis (Supporting Information, Discussion 1). As the next step, we compare the average TPL signals measured with thin films of different thicknesses with the resistance measurements (see Methods) of the same films (Figure 3a).

One can conjecture that the percolation threshold in electrical conductivity occurs for the film thickness being between 4 and 5 nm, since for 4 nm thin and thinner films we could not observe any finite electrical conductance. The absence of percolation for very thin films is also supported with the TEM images (Figure 2a,b). By comparing the electrical measurements with the TPL data obtained at the same illumination conditions for all film thicknesses, we conclude unequivocally that TPL signals reach maximum levels at the percolation threshold (Figure 3a). Such correlation is reasonable, since the largest density of the small gaps, at which hot spots could form, is expected near the percolation threshold.

With further gold deposition small gaps close, causing gold islands to merge into pathways and eventually approach a continuous film (Figure 2d). The TPL signals, originating from the two-photon absorption, are expected to be proportional to the square of the incident power.[47−49] It turned out, however, that, for all thin films, the TPL signals feature supercubic power dependences (Figure S1b). A possible explanation of this is

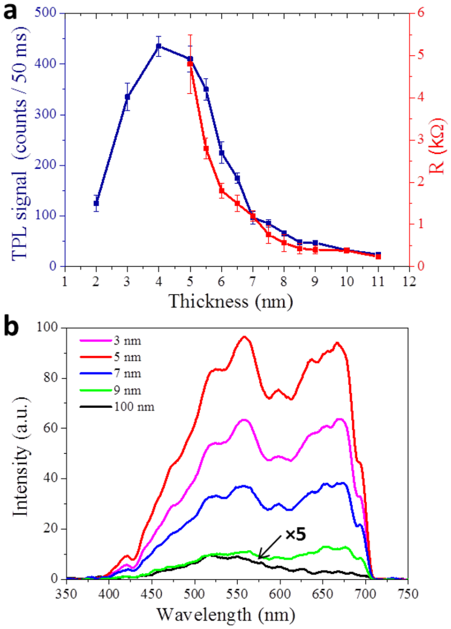

Figure 3. (a) TPL signal (blue) and resistance (red) measured for gold films with thicknesses from 2 to 11 nm at the excitation wavelength of 740 nm. (b) Luminescence spectra obtained for the gold films of thicknesses 3 (magenta), 5 (red), 7 (blue), 9 (green), and 100 nm (black) at the excitation wavelength of 780 nm. The luminescence intensity from bulk gold is multiplied by 5 for visibility. Arbitrary unit in (b) corresponds to 200 counts/s. The average incident power was ∼0.4 mW for thin gold films and ∼10 mW for bulk gold.

supercontinuum white-light generation in the sample,[37,50] possibly driven by nonlocal electron response[51] in complex geometric shapes of semicontinuous plasmonic nanostructures.[22] It seems that TPL and white-light generation (typically related to a fourth-order optical nonlinearity in dielectrics[37]) occur simultaneously contributing to the observed radiation and resulting in supercubic power dependencies. The white-light generation indicates the occurrence of strong FE effects, responsible for giant local fields, at not only illumination but also photoluminescence wavelengths.[52]

The broadband nature of FE effects is in fact expected for semicontinuous films near the percolation threshold.[3,6,34] To confirm the white-light continuum generation we recorded luminescence spectra (see Methods) for the same film thicknesses as those used in the measurements shown in Figure 1e, but at the excitation wavelength of 780 nm (Figure 3b). For comparison, we also recorded luminescence spectra for another excitation wavelength, 740 nm, and other film thicknesses (Figure S1c,d). All spectra measured with thin films appear similar (apart from the signal level) and very different from the spectrum recorded with the 100 nm-thick gold film, especially in the wavelength range of 600−700 nm. The thin-film spectra feature two broad maxima near 550 and 675 nm with the shape being practically independent of the (thin) film thickness and excitation wavelength. The maximum near 550 nm has also been observed on TPL spectra from rough gold surfaces,[48] and can be ascribed to the influence of interband transitions in gold[24,48] and, especially in our case, to localized SP resonances in gold nanoparticles. The second broad maximum near 675 nm is somewhat artificial as the drastic TPL signal decrease near 700 nm is caused by the filter cutting off reflected (powerful) FH radiation. The apparent absence of a pronounced peak at the second-harmonic frequency is related to the fact that the second-harmonic generation, contrary to the TPL, does not benefit from SP-based enhancement effects simply because SPs at wavelengths shorter than 400 nm are not supported by gold.[24] It should be mentioned that the photoluminescence was so strong that it was even possible to directly observe it by eye in the microscope when scans were not recorded. Note that white-light continuum generation in gold was first observed also in the range near 550−600 nm.[37]

Photothermally Induced Anisotropic Damage. It is intuitively expected that the TPL cannot steadily increase with an increase of the incident illumination power simply because any optical absorption is accompanied by heating. In our case, this heating causes eventual damage of the metal nanostructures by their melting and reshaping. The photothermally induced damage incurred by scanning a sample area with a focused pump beam, hereafter referred to as a "writing" process, can easily be visualized in a "reading" procedure when a larger surface area is subsequently scanned with a laser power well below the damage threshold. The same procedure can also be used to verify the absence of damage (and it was systematically used in our experiments reported here). The TPL from the written pattern appears to be weaker than that from the surrounding undamaged area, with TPL signals from written areas decreasing rapidly when increasing the laser power used for writing (Figure S2). This effect can be explained by local heating, melting, and reshaping of gold nanostructures at hot spots, since strong enhancement of local fields implies strong (and local) enhancement of absorption of radiation due to Ohmic losses. It should be noted that the damage could not be reproduced, with the laser operating in the continuous mode with the same average power, because local heating produced by short intense pulses results in much higher (instantaneous) temperatures than that due to continuous heating at low intensities. Additionally, it is expected that the temperature rise is significantly weaker in the continuous operation mode due to fast heat dissipation from relatively small heated volumes of hot spots.

Interestingly, a decrease in TPL signals from the damaged area was only observed when the laser polarization was the same during both reading and writing, while for orthogonal polarizations TPL signals from the damaged area were practically the same or even higher than those from the neighboring undamaged areas (Figure S2). However, such anisotropy was not well reproducible and clearly pronounced for thin gold films on glass substrates. It is reasonable to suggest that thermal conductivity of a substrate plays an important role in the optical damage by influencing the rate of heat dissipation from strongly localized hot spots to the substrate. In order to elucidate the influence of the substrate material, we prepared gold films with nominal thicknesses of 3, 5, 7, and 9 nm on high resistivity silicon substrates (see Methods). It turned out, for the same incident power, that the TPL from thin gold films on silicon substrates is considerably weaker, practically by 2 orders of magnitude, than the TPL from similar thin films on glass

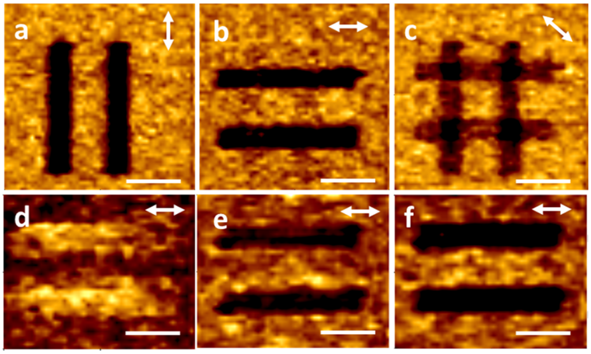

Figure 4. TPL images obtained from the 5 nm thin gold film on a silicon substrate, which demonstrate (a−c) polarization and (d−e) wavelength dependences. Two pairs of lines in (a)−(c) are written with the FH polarization along the corresponding lines. Both writing and reading were carried out at the wavelength of 740 nm. A pair of lines in (d)−(f) is written at the wavelength of 780 nm with the FH polarization along the correspondent lines, while the reading was done at the wavelength of (d) 740, (e) 780, and (f) 820 nm. Double arrows indicate the FH polarization during the read-out. The FH beam powers of ∼3 and ∼1 mW are used for writing and reading, respectively. The scale bars are 5 μm.

substrates, although the luminescence spectra are very similar (Figure S3). We relate this striking difference to a very large difference in the thermal conductivity of glass and silicon, which is also about 2 orders of magnitude,[53] because relaxation processes in gold are expected to speed up at elevated temperatures. At the same time, the polarization anisotropy effect in writing and reading out experiments, although requiring large powers of illumination, became much more pronounced and better defined compared to that observed with the films on glass substrates. Two orthogonal pairs of stripes written with orthogonal polarizations can be observed separately and practically without cross talk by using the corresponding orthogonal polarizations during the read-out procedure (Figure 4a−c). Noting that thermal conductivities of silicon and gold are of the same order of magnitude,[52] we explain the observed differences by the circumstance that gold nanostructures on glass substrates are heated to higher temperatures and more homogeneously than those on silicon substrates, because the latter serve as a very efficient heat dissipation channel (even more efficient than thin gold films). Consequently, the damage in gold nanostructured films on silicon substrates is expected to be stronger localized, essentially to the area of hot spots. The hypothesis is therefore that, within the illuminating 0.75 μm diameter beam spot (see experimental details SI), there are several bright (dipolar) localized SP excitations (hot spots), and each can be excited with a particular linear polarization, contributing substantially to the TPL signal obtained in the read-out procedure.

It is also reasonable to expect that many hot spots are related to the gap-induced FEs, with the electric fields being strongly enhanced in tiny gaps (oriented perpendicular to the incident field polarization) between resonant nanoparticle.[37,54−56] The hot spots can be damaged by local heating (when using silicon substrates) with subsequent reshaping, but only when using the correspondingly polarized illumination during writing. Damaged locations can no longer efficiently contribute to TPL when the same polarization is used during reading, resulting in the overall decrease of the TPL signal. At the same time, for the read-out with the orthogonal polarization, this damage can hardly be seen, since the damaged locations were not hosting hot spots for this polarization in the first place. This explanation accounts also for the polarization-dependent damage observed in the FH images (i.e., at the illumination wavelength), although with a reduced resolution and contrast (Figure S4) simply because of linear contrast being weaker than the nonlinear one.

The suggested mechanism is somewhat resembling that exploited in the polarization and wavelength multiplexed optical recording mediated by SP in gold nanorods.[45] In our case, the TPL images obtained during the read-out procedure also exhibit the sensitivity with respect to the illumination wavelength: the contrast becomes stronger for longer wavelengths and (unexpectedly) inverted for short wavelengths (Figure 4d−f). Moreover, the contrast inversion for short wavelengths is also observed in the FH images (Figure S5). These effects can be explained within the same hypothesis described above by taking into account the fact that metal nanoparticles upon melting tend to decrease their surface area due to surface tension.[1] Therefore, elongated nanoparticles that are resonant at a given wavelength become thicker and shorter during writing at this wavelength with their resonance shifting to shorter wavelengths. Their contribution to both FH and TPL signals are thereby increasing for shorter and decreasing for longer read-out wavelengths (Figure S5). The damage mechanism described above is consistent with SEM images of pristine and damaged areas of the 5 nm thin gold film on a silicon substrate, showing unambiguously an increase of interparticle distances along the polarization direction of writing field due to reshaping, including merging of tiny particles, caused by (enhanced and localized) heating induced by the gap-induced FEs (Figure 5a,b). This observation accounts for the pronounced polarization effects in the TPL writing/reading procedures. Other damage effects include spatial subwavelength-sized localization of damaged areas and reshaping in the form of rounding of particles (Figure S6). The latter feature is important for understanding of the contrast inversion in the FH and TPL images at wavelengths shorter than that used for writing.

Near-Field Imaging. The proposed mechanism of the photothermally induced anisotropic damage relies on the

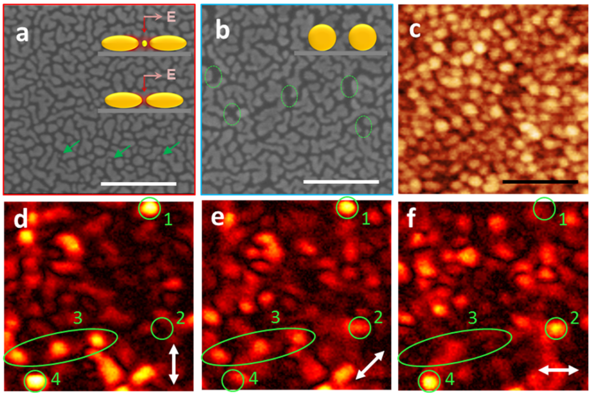

Figure 5. SEM images of (a) the pristine 5 nm thin gold film on a silicon substrate and (b) the same film after the laser-induced damage. Insets schematically depict the process, where hot spots created inside a small gap with or without a small gold particle, heat up under illumination, resulting in melting and reshaping, eventually increasing the gap. Green arrows in (a) show some of the small particles presented in the undamaged sample, and green ellipses in (b) represent large gaps created after laser illumination. (c−f) Pseudocolour SNOM images of (c) topography and (d−f) optical near-field amplitude of the pristine 5 nm thin gold film on a glass substrate. Double arrows represent the illumination polarization of the telecom laser (λ = 1500 nm). Green circles in (d)−(f) encircles the same hot spots. The scale bars in (a)−(c) are 200 nm.

existence of strongly enhanced and confined (dipolar) resonant SP excitations in near-percolation thin gold films used in our experiments. In principle, their existence at thin (semicontinuous) near-percolation metal films illuminated with practically any wavelength is well documented,[3−6,13−16,34] but their spatial extensions and the corresponding FEs as well as the polarization and wavelength sensitivity are strongly dependent on the actual film morphology, for example, self-similarity and self-affinity properties.[34] In order to reveal main features in spatial distribution of hot spots and associated FEs, we conducted near-field phase- and amplitude resolved mapping of local optical fields formed at the pristine 5 nm thin gold film on a glass substrate illuminated with a tunable continuous laser at telecom wavelengths (see experimental details, SI). Scanning near-field optical microscopy (SNOM) images revealed the existence of randomly distributed and strongly localized (~30 nm wide) and enhanced (Figure S7) electromagnetic excitations with the FE levels that exhibit a well pronounced polarization dependence, indicating a dipolar response (Figure 5c−f). For example, intense hot spots marked as "1" and "2" in Figures 4d,e are lighting up for orthogonal polarizations of the incident light while being separated by ~400 nm, a separation that is smaller than the illuminating beam spot size in the TPL experiments.

These observations strongly support our explanation of the polarization dependent TPL (and FH) writing and reading. Although the direct overlap of the simultaneously recorded hot spots with topography suggests that the hot spots observed can primarily be related to gaps between particles or to single particles (Figure S8), we find this evidence inconclusive because of a limited SNOM resolution (~10 nm) dictated by the probe tip size.[57,58] Near-field images obtained at different illumination wavelengths indicate that the FE levels at hot spots weakly depend on the wavelength, at least within the wavelength interval (~200 nm) available for near-field characterization (Figure S9). Note that the gap-induced FEs are associated with the boundary conditions for the electric field,[54,55] and are thereby weakly wavelength dependent. Overall, these observations are also consistent with the wavelength-dependent features in TPL experiments discussed in the previous section.

Our SNOM operation relies on a high-harmonic filtering procedure (see Methods) that makes a direct evaluation of the FE levels impossible.[57,58] However, by analyzing the results of both SNOM and TPL measurements, we can quantitatively estimate the FE levels in the brightest hot spots by relating their contributions to the overall TPL signal (see Supporting Information, Note 1). As can be deduced from the experimental near-field spatial distributions (Figure S7), the strongest hot spot within the area of TPL scanning laser spot contributes ~20% to the total TPL signal, causing the observed TPL variations (Figure 2e). By comparing the TPL signals from the bulk and thin gold films and taking into account the size of hot spots measured from the SNOM images, we estimate the average field intensity enhancement of ~6000 in hot spots observed with the 5 nm-thin gold film (see Supporting Information, Note 1). This FE level is favorably compared to that reported in the first experiments on white-light generation in gold dimer antennas[37] and, in general, found consistent with the results reported by other groups for nanostructures containing sub-10 nm-wide gaps (see Supporting Information, Note 2).

■ CONCLUSIONS

Summarizing, the main features of the TPL from thin (naturally semicontinuous) near-percolation gold films have been thoroughly investigated using linear reflection spectroscopy along with the TPL and near-field microscopies applied to the films of different thicknesses (ranging from 2 to 11 nm) deposited on glass and silicon substrates. We have mapped the thickness-dependent TPL signals simultaneously with the electrical conductivity measurements, establishing unequivocally that the strongest TPL signals are generated with close to the percolation threshold films. We have revealed the underlying physical mechanisms behind the photothermally induced reshaping of nanostructured films that are involved in the polarization and wavelength damage observed in the TPL writing and reading out procedures. We believe that these easy-to-fabricate and scalable semicontinuous (randomly nanostructured) metallic films near the percolation threshold constitute an important and attractive alternative to more traditional nanostructures, which are admittedly much better defined and controlled but also requiring sophisticated fabrication procedures, used currently for diverse FE applications, including SERS based diagnostics and other kinds of biomolecule optical sensing.

The near-percolation films also open up new venues also for direct laser writing in plasmonic nanostructures that can be conducted over wafer-size areas with the capabilities extended by the polarization effect. We estimate the writing beam energy required to write 1 pixel/bit on the 5 nm thin gold film to be ~25−50 μJ/bit for glass substrates and ~150 μJ/bit for silicon substrates (Figure S10). Although this level is larger than that obtained with gold nanorods,[45] the fabrication of near-percolation films is much more straightforward, while also allowing for multiplexing in depth by sandwiching several thin layers of dielectric and gold. One should not underestimate the importance of exciting possibilities offered by these films for generating broadband and very strong FE effects for quantum plasmonics,[4,38−40] especially when taking into account extremely tight confinement of hot spots,[59] as revealed by near-field imaging in this work. Finally, white-light generation in the percolation geometry should definitely be investigated further with the perspective of exploiting this phenomenon in nonlinear plasmonics and nanophotonics. Overall, we believe that extremely rich and interesting physics involved in light interaction with near-percolation metal films along with their straightforward and scalable one-step fabrication procedure promises a wide range of fascinating developments and technological applications within diverse areas of modern nanotechnology, from biomolecule optical sensing to ultra-dense optical data storage.

■ METHODS

Fabrication. Stripe patterned thin films of gold were fabricated for conductive measurements at different thicknesses by UV-lithography and electron-beam deposition. The borosilicate glass substrates are baked out overnight at 250 °C. After baking, the wafers are immediately spin-coated with a 2 μm layer of NZ nLOF 2020 resist, and then exposed with UV-radiation through a shadow mask. After exposure the samples are baked for 2 min at 110 °C after which the pattern for the thin films are puddle developed with a 2.38% TMAH water solution. After development, gold is deposited with electron-beam at a vacuum chamber pressure of $\sim 10^{-5}$ mbar, and a deposition rate of 2 Å/s, onto the room temperature substrates. After deposition, the samples are transferred to a lift-off bath of Microposit Remover 1165, where they remain for several hours to remove excess photoresist. To protect the thin films, ultrasound is not used during the lift-off process. Films were produced with thicknesses between 2 and 11 nm. The dimensions of the stripes were 1 mm × 250 μm. The fabrication was repeated without lithography to produce a set of percolation films on glass with the full range of thicknesses between 2 and 11 nm, to avoid any risk of contamination from left-over photoresist for the optical experiments. Another set of samples on borosilicate glass substrates was prepared to compare bulk gold and thin films. A silicon shadow mask was used to cover one-half of the wafer, and a 100 nm bulk gold film was deposited at 10 Å/s using the same deposition system. After removing the mask a 3, 5, 7, or 9 nm thin film was deposited on the wafer with 2 Å/s rate. The samples on silicon substrate and TEM membranes with thicknesses of 3, 5, 7, and 9 nm were prepared by using the same deposition parameters as the first samples on glass substrates, but no photolithography was used to define the shape of the deposited films.

SEM and TEM. For the visualization of gold films, we used a scanning electron microscope Nova NanoSEM from FEI and transmission electron microscope Tecnai T20 G^2 from FEI. SEM images were recorded with a through-the-lens detector (TLD), using an acceleration voltage of 3.00 kV at a working distance of 4 mm. TEM images were recorded at an acceleration voltage of 200 kV.

Linear Spectroscopy. The spectroscopic reflection analysis was performed on a BX51 microscope (Olympus) equipped with a halogen light source, polarizers and a fiber-coupled grating spectrometer QE65000 (Ocean Optics) with a wavelength resolution of 1.6 nm. The reflected and transmitted light was collected using an MPlanFL objective (Olympus) with magnification 100× (NA = 0.9). The image area analyzed by the spectrometer is limited by a pinhole with a diameter of 150 μm resulting in a circular probing area with a diameter of 1.5 μm. The experimental data in (Figure S1a) represent the reflection ratio R_{str}/R_{ref}, where R_{str} is the reflection measured from the films and R_{ref} is the reference from a broadband laser mirror (Edmund Optics, NT64−114) that exhibits an average reflection of 99% between 350 and 1100 nm of light wavelength.

Two Photon-Excited Photoluminescence (TPL) Microscopy. We rely on the approach described in refs 50−52, and the setup consists of a scanning optical microscope in reflection geometry built on the basis of a commercial microscope and a computer-controlled translation stage. The linearly polarized light beam from a mode-locked pulsed (pulse duration ~200 fs, repetition rate ~80 MHz) Ti-Sapphire laser (wavelength λ = 730−860 nm, $\delta\lambda \approx$ 10 nm, average power ~ 300 mW) is used as an illumination source at the FH frequency. After passing an optical isolator (to suppress back-reflection), half-wave plate, polarizer, red color filter and wavelength selective beam splitter, the laser beam is focused on the sample surface at normal incidence with a Mitutoyo infinity-corrected long working distance objective (100×, NA = 0.70). The half-wave plate and polarizer allow accurate adjustment of the incident power. TPL radiation generated in reflection and the reflected FH beam are collected simultaneously with the same objective, separated by the wavelength selective beam splitter, directed through the appropriate filters and detected with two photomultiplier tubes (PMTs). The tube for TPL photons (within the transmission band of 350−550 nm) is connected with a photon counter giving typically only ~20 dark counts per second (cps). The FH and TPL spatial resolution at full-width−half-maximum is ~0.75 and ~0.35 μm, respectively, which means no individual clusters will be resolved in the TPL images. In this work, we used the following scan parameters: the integration time (at one point) of 50 ms, scanning speed (between the measurement points) of 20 μm/s, and scanning step sizes of ~350 and 700 nm. We adjusted the incident power P within the ranges of 0.15−0.5 mW, for films on glass substrates, and 0.5−1.2 mW, for films on silicon substrates, in order to obtain significant TPL signals and record the TPL signal dependence on the incident powers. For writing we used incident power *P* within the ranges of 0.6−4 and 2.5−5 mW for films on glass and silicon substrates, respectively. For the reference bulk gold sample, we confirmed that the TPL signals obtained depend quadratically on the incident power. During these measurements, we kept for simplicity the excitation wavelength fixed at 740 nm, since there are no specific resonances (Figure S1a) at this wavelength, and 740 nm is more visible and convenient to focus.

Electrical Measurements. For the conductive measurements, we used the two-probe method and results obtained by a Keithley 2400 SourceMeter. In the experiment, we used the stripes on silica substrate (see Fabrication) with an electrical contact made at each end. Electrical contacts were established using EPO-TEK H20E conductive epoxy.

Photoluminescence Spectroscopy. To record spectra of the observed photoluminescence, we used the same setup as for TPL measurements but instead of the PMT for TPL photons we used the spectrometer QE65000 (Ocean Optics) and with only a filter to cut off the laser line. Since long exposure time or high power could damage the sample during recording of photoluminescence spectra, we continuously scanned the sample with the following parameters. Integration time (at one point) of 50 ms, scanning speed (between the measurement points) of 20 μm/s, scanning step size of ∼350 nm, and incident power $P \sim 0.4$ mW for gold film on silica substrate and ∼2 mW on silicon. The recording time for the spectrum is 60 s.

Near-Field Microscopy. The near-field investigations were performed using a scattering-type SNOM (NeaSpec) based on an atomic force microscope (AFM), in which the near-field is scattered by an uncoated silicon probe, operating in a tapping mode at a frequency $\Omega \approx 250$ kHz. The sample was illuminated normally from below (transmission mode) with a linearly polarized tunable (1425−1625 nm) telecom laser. The scattered signal was detected and demodulated at the fourth harmonic 4Ω to filter the near-field contribution from the background. Additionally, the interferometric pseudoheterodyne detection was employed, which allows imaging of both the amplitude and the phase of the near-field.

■ ASSOCIATED CONTENT

Ⓢ Supporting Information

The Supporting Information is available free of charge on the ACS Publications website at DOI: 10.1021/acsphotonics.7b00107.

> Additional figures for the characterization of the gold films and estimation of the average field intensity enhancement (PDF).

■ AUTHOR INFORMATION

Corresponding Author

*E-mail: seib@iti.sdu.dk.

ORCID

N. Asger Mortensen: 0000-0001-7936-6264

Sergey I. Bozhevolnyi: 0000-0002-0393-4859

Author Contributions

S.I.B. and J.B. conceived the experiment. C.F. and N.S. designed and fabricated the samples and performed the electron microscopy (SEM and TEM). S.M.N. and V.C. performed the two-photon luminescence experiments. S.M.N. conducted electrical measurements and optical spectroscopy. V.A.Z. performed and analyzed near-field microscopy measurements. S.M.N. and J.B. drafted the manuscript. All authors discussed the results and commented on the manuscript. S.I.B. and N.A.M. supervised the project.

Notes

The authors declare no competing financial interest.

■ ACKNOWLEDGMENTS

The authors gratefully acknowledge financial support from the European Research Council, Grant 341054 (PLAQNAP), CONACyT Basic Scientific Research Grant 250719, and the Danish Council for Independent Research−Natural Sciences (Project 1323-00087). Center for Nano Optics was financially supported from the University of Southern Denmark (SDU 2020 Funding), while Center for Nanostructured Graphene (CNG) was funded by the Danish National Research Foundation (CoE Project DNRF103).

■ REFERENCES

(1) Schuller, J. A.; Barnard, E. S.; Cai, W.; Jun, Y. C.; Justin, S.; White, J. S.; Brongersma, M. L. Plasmonics for extreme light concentration and manipulation. *Nat. Mater.* **2010**, *9*, 193−204.

(2) Zhu, Z. F. X. Plasmonics in nanostructures. *Adv. Mater.* **2013**, *25*, 3840−3856.

(3) Shalaev, V. M. Electromagnetic properties of small-particle composites. *Phys. Rep.* **1996**, *272*, 61−137.

(4) Gaio, M.; Castro-Lopez, M.; Renger, J.; van Hulst, N.; Sapienza, R. Percolating plasmonic networks for light emission control. *Faraday Discuss.* **2015**, *178*, 237−252.

(5) Ducourtieux, S.; Podolskiy, V. A.; Grésillon, S.; Buil, S.; Berini, B.; Gadenne, P.; Boccara, A. C.; Rivoal, J. C.; Bragg, W. D.; Banerjee, K.; Safonov, V. P.; Drachev, V. P.; Ying, Z. C.; Sarychev, A. K.; Shalaev, V. M. Near-field optical studies of semicontinuous metal films. *Phys. Rev. B: Condens. Matter Mater. Phys.* **2001**, *64*, 165403.

(6) Seal, K.; Genov, D. A.; Sarychev, A. K.; Noh, H.; Shalaev, V. M.; Ying, Z. C.; Zhang, X.; Cao, H. Coexistence of localized and delocalized surface plasmon modes in percolating metal films. *Phys. Rev. Lett.* **2006**, *97*, 206103.

(7) Novikov, S. M.; Beermann, J.; Frydendahl, C.; Stenger, N.; Coello, V.; Mortensen, N. A.; Bozhevolnyi, S. I. Enhancement of two-photon photoluminescence and SERS for low- coverage gold films. *Opt. Express* **2016**, *24*, 16743−16751.

(8) De Zuani, S.; Rommel, M.; Gompf, B.; Berrier, A.; Weis, J.; Dressel, M. Suppressed percolation in nearly closed gold films. *ACS Photonics* **2016**, *3*, 1109−1115.

(9) De Zuani, S.; Peterseim, T.; Berrier, A.; Gompf, B.; Dressel, M. Second harmonic generation enhancement at the percolation threshold. *Appl. Phys. Lett.* **2014**, *104*, 241109.

(10) Hövel, M.; Gompf, B.; Dressel, M. Dielectric properties of ultrathin metal films around the percolation threshold. *Phys. Rev. B: Condens. Matter Mater. Phys.* **2010**, *81*, 035402.

(11) McPeak, K. M.; Jayanti, S. V.; Kress, S. J. P.; Meyer, S.; Iotti, S.; Rossinelli, A.; Norris, D. J. Plasmonic films can easily be better: rules and recipes. *ACS Photonics* **2015**, *2*, 326−333.

(12) Greene, J. Thin film nucleation, growth, and microstructural evolution: An atomic scale view. In *Handbook of Deposition Technologies for Films and Coatings*, 3rd ed.; Martin, P. M., Ed.; William Andrew Publishing: Boston, 2010; pp 554−620.

(13) Losquin, A.; Camelio, S.; Rossouw, D.; Besbes, M.; Pailloux, F.; Babonneau, D.; Botton, G. A.; Greffet, J.-J.; Stéphan, O.; Kociak, M. Experimental evidence of nanometer-scale confinement of plasmonic eigenmodes responsible for hot spots in random metallic films. *Phys. Rev. B: Condens. Matter Mater. Phys.* **2013**, *88*, 115427.

(14) Shiohara, A.; Novikov, S. M.; Solís, D. M.; Taboada, J. M.; Obelleiro, F.; Liz-Marzán, L. M. Plasmon modes and hot spots in gold nanostar-satellite clusters. *J. Phys. Chem. C* **2015**, *119*, 10836−10843.

(15) Moskovits, M. Imaging: Spot the hotspot. *Nature* **2011**, *469*, 307−308.

(16) Wen, F.; Ye, J.; Liu, N.; Van Dorpe, P.; Nordlander, P.; Halas, N. J. Plasmon Transmutation: Inducing New Modes in Nanoclusters by Adding Dielectric Nanoparticles. *Nano Lett.* **2012**, *12*, 5020−5026.

(17) Toscano, G.; Raza, S.; Jauho, A.-P.; Mortensen, N. A.; Wubs, M. Modified field enhancement and extinction in plasmonic nanowire dimers due to nonlocal response. *Opt. Express* **2012**, *20*, 4176−4188.

(18) Mortensen, N. A.; Raza, S.; Wubs, M.; Søndergaard, T.; Bozhevolnyi, S. I. A generalized nonlocal optical response theory for plasmonic nanostructures. *Nat. Commun.* **2014**, *5*, 3809.

(19) Ginzburg, P.; Krasavin, A. V.; Wurtz, G. A.; Zayats, A. V. Nonperturbative hydrodynamic model for multiple harmonics generation in metallic nanostructures. *ACS Photonics* **2015**, *2*, 8−13.

(20) Hille, A.; Moeferdt, M.; Wolff, C.; Matyssek, C.; Rodríguez-Oliveros, R.; Prohm, C.; Niegemann, J.; Grafström, S.; Eng, L. M.; Busch, K. Second harmonic generation from metal nano-particle resonators: Numerical analysis on the basis of the hydrodynamic Drude model. *J. Phys. Chem. C* **2016**, *120*, 1163−1169.

(21) Huynh, D.-N.; Moeferdt, M.; Matyssek, C.; Wolff, C.; Busch, K. Ultrafast three-wave-mixing in plasmonic nanostructures. *Appl. Phys. B: Lasers Opt.* **2016**, *122*, 139.

(22) Krasavin, A. V.; Ginzburg, P.; Wurtz, G. A.; Zayats, A. V. Nonlocality-driven supercontinuum white light generation in plasmonic nanostructures. *Nat. Commun.* **2016**, *7*, 11497.

(23) Gramotnev, D. K.; Bozhevolnyi, S. I. Plasmonics beyond the diffraction limit. *Nat. Photonics* **2010**, *4*, 83−91.

(24) Maier, S. A. *Plasmonics: Fundamentals and Applications*; Springer: New York, 2007.

(25) Lal, S.; Link, S.; Halas, N. J. Nano-optics from sensing to waveguiding. *Nat. Photonics* **2007**, *1*, 641−648.

(26) Anker, J. N.; Lyandres, O.; Shah, N. C.; Jing Zhao, J.; Van Duyne, R. P. Biosensing with plasmonic nanosensors. *Nat. Mater.* **2008**, *7*, 442−453.

(27) Ringe, E.; Langille, M. R.; Sohn, K.; Zhang, J.; Huang, J.; Mirkin, C. A.; Van Duyne, R. P.; Marks, L. D. Plasmon length: A universal parameter to describe size effects in gold nanoparticles. *J. Phys. Chem. Lett.* **2012**, *3*, 1479−1483.

(28) Mayer, K. M.; Hafner, J. H. Localized surface plasmon resonance sensors. *Chem. Rev.* **2011**, *111*, 3828−3857.

(29) Yap, F. L.; Thoniyot, P.; Krishnan, S.; Krishnamoorthy, S. Nanoparticle cluster arrays for high-performance SERS through directed self-assembly on flat substrates and on optical fibers. *ACS Nano* **2012**, *6*, 2056−2070.

(30) Gandra, N.; Abbas, A.; Tian, L.; Singamaneni, S. Plasmonic planet-satellite analogues: Hierarchical self-assembly of gold nanostructures. *Nano Lett.* **2012**, *12*, 2645−2651.

(31) Beermann, J.; Novikov, S. M.; Albrektsen, O.; Nielsen, M. G.; Bozhevolnyi, S. I. Surface- enhanced Raman imaging of fractal shaped periodic metal nanostructures. *J. Opt. Soc. Am. B* **2009**, *26*, 2370−2376.

(32) Beermann, J.; Novikov, S. M.; Leosson, K.; Bozhevolnyi, S. I. Surface enhanced Raman microscopy with metal nanoparticle arrays. *J. Opt. A: Pure Appl. Opt.* **2009**, *11*, 075004.

(33) Ueno, K.; Juodkazis, S.; Mizeikis, V.; Sasaki, K.; Misawa, H. Clusters of closely spaced gold nanoparticles as a source of two-photon photoluminescence at visible wavelengths. *Adv. Mater.* **2008**, *20*, 26−30.

(34) Sarychev, A. K.; Shalaev, V. M. Electromagnetic field fluctuations and optical nonlinearities in metal-dielectric composites. *Phys. Rep.* **2000**, *335*, 275−371.

(35) Rodríguez-Lorenzo, L.; Romo-Herrera, J. M.; Pérez-Juste, J.; Alvarez-Puebla, R. A.; Liz-Marzán, L. M. Reshaping and LSPR tuning of Au nanostars in the presence of CTAB. *J. Mater. Chem.* **2011**, *21*, 11544−11549.

(36) Knight, M. W.; Liu, L.; Wang, Y.; Brown, L.; Mukherjee, S.; King, N. S.; Everitt, H. O.; Nordlander, P.; Halas, N. J. Aluminum Plasmonic Nanoantennas. *Nano Lett.* **2012**, *12*, 6000−6004.

(37) Mühlschlegel, P.; Eisler, H. J.; Martin, O. J. F.; Hecht, B.; Pohl, D. W. Resonant optical antennas. *Science* **2005**, *308*, 1607−1609.

(38) Tame, M. S.; McEnery, K. R.; Özdemir, Ş. K.; Lee, J.; Maier, S. A.; Kim, M. S. Quantum plasmonics. *Nat. Phys.* **2013**, *9*, 329−340.

(39) Bozhevolnyi, S. I.; Mortensen, N. A. Plasmonics for emerging quantum technologies. *Nanophotonics* **2017**, *6*, n/a DOI: 10.1515/nanoph-2016-0179.

(40) Bozhevolnyi, S. I.; Martín-Moreno, L.; García-Vidal, F. J. Quantum Plasmonics. *Springer Series in Solid-State Sciences*; Springer International Publishing: New York, 2017; Vol. *185*.

(41) Oates, T. W. H.; Sugime, H.; Noda, S. Combinatorial surface-enhanced Raman spectroscopy and spectroscopic ellipsometry of silver island films. *J. Phys. Chem. C* **2009**, *113*, 4820−4828.

(42) Cialla, D.; Marz, A.; Bohme, R.; Theil, F.; Weber, K.; Schmitt, M.; Popp, J. Surface-enhanced Raman spectroscopy (SERS): progress and trends. *Anal. Bioanal. Chem.* **2012**, *403*, 27−54.

(43) Mie, S. M.; Emery, S. R. Probing single molecules and single nanoparticles by surface- enhanced Raman scattering. *Science* **1997**, *275*, 1102−1106.

(44) Zhu, X.; Vannahme, C.; Højlund-Nielsen, E.; Mortensen, N. A.; Kristensen, A. Plasmonic colour laser printing. *Nat. Nanotechnol.* **2015**, *11*, 325−329.

(45) Zijlstra, P.; Chon, J. W.; Gu, M. Five-dimensional optical recording mediated by surface plasmons in gold nanorods. *Nature* **2009**, *459*, 410−413.

(46) Gu, M.; Zhang, Q.; Lamon, S. Nanomaterials for optical data storage. *Nature Reviews Materials* **2016**, *1*, 16070.

(47) Mooradian, A. Photoluminescence of metals. *Phys. Rev. Lett.* **1969**, *22*, 185−187.

(48) Boyd, G. T.; Yu, Z. H.; Shen, Y. R. Photoinduced luminescence from the noble metals and its enhancement on roughened surfaces. *Phys. Rev. B: Condens. Matter Mater. Phys.* **1986**, *33*, 7923−7936.

(49) Schuck, P. J.; Fromm, D. P.; Sundaramurthy, A.; Kino, G. S.; Moerner, W. E. Improving the mismatch between light and nanoscale objects with gold bowtie nanoantennas. *Phys. Rev. Lett.* **2005**, *94*, 017402.

(50) Eichelbaum, M.; Schmidt, B. E.; Ibrahim, H.; Rademann, K. Three-photon-induced luminescence of gold nanoparticles embedded in and located on the surface of glassy nanolayers. *Nanotechnology* **2007**, *18*, 355702.

(51) Raza, S.; Bozhevolnyi, S. I.; Wubs, M.; Mortensen, N. A. Nonlocal optical response in metallic nanostructures. *J. Phys.: Condens. Matter* **2015**, *27*, 183204.

(52) Andersen, S. K. H.; Pors, A.; Bozhevolnyi, S. I. Gold photoluminescence wavelength and polarization engineering. *ACS Photonics* **2015**, *2*, 432−438.

(53) Weber, M. J. *Handbook of Optical Materials*. CRC Press: New York, 2003.

(54) Søndergaard, T.; Bozhevolnyi, S. I. Slow-plasmon resonant nanostructures: Scattering and field enhancements. *Phys. Rev. B: Condens. Matter Mater. Phys.* **2007**, *75*, 073402.

(55) Søndergaard, T.; Bozhevolnyi, S. I. Metal nano-strip optical resonators. *Opt. Express* **2007**, *15*, 4198−4204.

(56) Beermann, J.; Novikov, S. M.; Søndergaard, T.; Boltasseva, A. E.; Bozhevolnyi, S. I. Two-photon mapping of localized field enhancements in thin nanostrip antennas. *Opt. Express* **2008**, *16*, 17302−17309.

(57) Zenin, V. A.; Andryieuski, A.; Malureanu, R.; Radko, I. P.; Volkov, V. S.; Gramotnev, D. K.; Lavrinenko, A. V.; Bozhevolnyi, S. I. Boosting local field enhancement by on-chip nanofocusing and impedance-matched plasmonic antennas. *Nano Lett.* **2015**, *15*, 8148−8154.

(58) Andryieuski, A.; Zenin, V. A.; Malureanu, R.; Volkov, V. S.; Bozhevolnyi, S. I.; Lavrinenko, A. V. Direct Characterization of Plasmonic Slot Waveguides and Nanocouplers. *Nano Lett.* **2014**, *14*, 3925−3929.

(59) Bozhevolnyi, S. I.; Khurgin, J. B. Fundamental limitations in spontaneous emission rate of single-photon sources. *Optica* **2016**, *3*, 1418−1421.

Nanoscale

PAPER

Cite this: *Nanoscale*, 2017, **9**, 12014

Optical reconfiguration and polarization control in semi-continuous gold films close to the percolation threshold†

Christian Frydendahl, *[a,b] Taavi Repän, [a] Mathias Geisler, [a,b] Sergey M. Novikov,[c]
Jonas Beermann,[c] Andrei V. Lavrinenko, [a] Sanshui Xiao, [a,b]
Sergey I. Bozhevolnyi, [c] N. Asger Mortensen [a,b,c] and Nicolas Stenger *[a,b]

Received 12th May 2017,
Accepted 2nd August 2017

DOI: 10.1039/c7nr03378h

rsc.li/nanoscale

Controlling and confining light by exciting plasmons in resonant metallic nanostructures is an essential aspect of many new emerging optical technologies. Here we explore the possibility of controllably reconfiguring the intrinsic optical properties of semi-continuous gold films, by inducing permanent morphological changes with a femtosecond (fs)-pulsed laser above a critical power. Optical transmission spectroscopy measurements show a correlation between the spectra of the morphologically modified films and the wavelength, polarization, and the intensity of the laser used for alteration. In order to understand the modifications induced by the laser writing, we explore the near-field properties of these films with electron energy-loss spectroscopy (EELS). A comparison between our experimental data and full-wave simulations on the exact film morphologies hints toward a restructuring of the intrinsic plasmonic eigenmodes of the metallic film by photothermal effects. We explain these optical changes with a simple model and demonstrate experimentally that laser writing can be used to controllably modify the optical properties of these semi-continuous films. These metal films offer an easy-to-fabricate and scalable platform for technological applications such as molecular sensing and ultra-dense data storage.

Introduction

The ability of metallic nanostructures to localize and enhance optical fields down to the nanoscale *via* collective electron excitations (plasmons) has been the subject of intense study in the recent decades.[1] Many promising applications arise from the careful engineering of nanostructures to tune their optical properties. This allows sub-diffraction light focusing for spectroscopy and sensing applications like surface-enhanced Raman scattering (SERS),[2] enhancing light–matter interaction with new 2D materials,[3,4] and quantum information processing technologies.[5–7] Another application recently gaining in popularity is the tuning of a surface's spectral reflectivity by plasmonic nanostructures to produce colour images[8] with ultra-dense information storage.[9–11] However, due to the nanometre size scales needed these structures often require elaborate fabrication methods such as electron-beam lithography (EBL) or focused ion beam (FIB) milling.[12] EBL allows for precise and reproducible definition of nanostructures but at the cost of time consuming process steps to produce a mask pattern in a polymer resist.[13] Additionally, in most state of the art lithography systems the spatial resolution is still limited to about 10 nm.[13] FIB offers an alternative method for high-resolution and mask-less fabrication, but still requires long pattern writing times, and also comes with the potential problem of contaminating the structure materials with the milling ions.[14]

Self-assembled and self-similar metallic structures where high levels of field enhancement are hosted by the naturally occurring sub-nanometre sized gaps or protrusions, are thus of great interest as they offer an alternative source of strong field localization and enhancement. Typically these structures also have fast and scalable (bottom-up) fabrication methods with few processing steps.[15–17] While these types of structures promise scalable and easily fabricated nanostructures, their specific optical properties are however limited within the scope of their assembly methods. One way to expand the range of achievable excitations is of course to influence the assembly

---

[a] *Department of Photonics Engineering, Technical University of Denmark, Ørsteds Plads 343, DK-2800 Kongens Lyngby, Denmark. E-mail: chrfr@fotonik.dtu.dk, niste@fotonik.dtu.dk*

[b] *Center for Nanostructured Graphene, Technical University of Denmark, Ørsteds Plads 343, DK-2800 Kongens Lyngby, Denmark*

[c] *Center for Nano Optics, University of Southern Denmark, Campusvej 55, DK-5230 Odense M, Denmark*

† Electronic supplementary information (ESI) available: Additional morphology analysis from laser reshaping of the gold films, outline of how simulation geometry was achieved, and additional simulations. See DOI: 10.1039/C7NR03378H

This journal is © The Royal Society of Chemistry 2017

process during fabrication,[18] but another way is to alter metallic and dielectric nanostructures post-assembly *via* controlled photothermal reshaping.[11,19–24] One such system, that we study here, is thin gold films near the percolation threshold subjected to morphological modifications by pulsed laser illumination. The nanostructured morphology of percolation metal films arises from the Volmer–Weber process of metal growth on amorphous dielectric substrates.[25–27] During the deposition process the metal atoms have a mutually strong interaction, while interacting less with the substrate. This leads to the formation of isolated clusters that tend to grow in the substrate plane during deposition, eventually reaching a percolation threshold where they merge to form a connected system. Further metal deposition will then serve to close up any remaining gaps in the film morphology, and eventually the system will transition into a metal on metal growth process. Depending on the deposition parameters and substrate used, it is possible to routinely fabricate large-scale areas of such metal structures where the smallest feature sizes can be at the sub-nanometre scale.[25]

These films also hold interesting non-linear optical properties with prospects for white-light generation with modest pump powers.[28] However, the optical properties of these films remain to be fully investigated experimentally with dedicated spectroscopic methods. The small feature sizes of these metal films present a significant challenge for experimental exploration with conventional near-field optics. For scattering scanning near-field optical microscopes (s-SNOMs) the spatial resolution limit of the setup will still be defined by the cantilever tip size, which in the most state of the art devices is still in the order of a few nanometres.[29] Despite being an exceptionally high spatial resolution for photon-based characterization, the limited spatial resolution of the tip does not allow to explore the optical properties of ultra-small plasmonic gaps with dimensions on the single nanometre scale and below.[30,31] Furthermore, s-SNOM techniques are usually spectrally limited to a single or a small set of energies which is detrimental to fully characterize the plasmonic eigenmodes of these complex structures. Electron-based spectroscopic techniques such as energy-filtered electron energy-loss spectroscopy in monochromated transmission electron microscopes (TEMs) offers an attractive alternative to access the optical properties of nanometre and subnanometre sized plasmonic structures.[32–43] Indeed, the exceptional subnamometre spatial resolution and the broadband excitation spectrum of the electron beam[44,45] has recently been used to spatially map the intrinsic plasmonic eigenmodes in self-similar pristine silver films.[42] This method permits to identify unambiguously plasmonic hot spots that are not related to the morphology of the films in a simple way, as predicted theoretically.[46]

Here we explore novel aspects of the optical reconfiguration of the plasmon excitations in gold films near the percolation threshold. After illumination with a fs-pulsed laser above a critical power, it is possible to induce permanent morphological modifications in the films. For clarity we will refer to this process by *laser writing* in the rest of the text. These morphology changes allow for controlled changes to the film's optical properties. Using optical transmission spectroscopy, we demonstrate how it is possible to inscribe polarized and wavelength selective field enhancement into these otherwise broadly resonant films with laser writing. We explain the morphology changes of the films from laser writing by photothermal reshaping of the metal nanoparticles in resonance with the excitation wavelength. We show that this process depends intricately on the degree of film percolation, illumination power, polarization, and wavelength of the laser. Our explanation includes three different processes: particle spherification for elongated nanoparticles, dimer decoupling for large plasmonic gaps, and dimer welding/particle fusion for small gaps. We use hyperspectral imaging with nanometre resolution to show statistically the effect of morphological changes on the distribution of plasmonic modes in the near-field. By utilizing full-wave simulations of our explored morphologies, we highlight that the polarization dependence in the inscribed films originates from resonant elongated particles that have formed during the photothermal processes. Despite the complexity of the optical properties in these percolation films, we show that the far-field optical properties can be modified controllably through laser writing.

Results and discussion

Morphology changes and induced optical anisotropy

We have fabricated 3 samples of thin gold films on 18 nm thin SiO_2 TEM membranes (see methods). The films are of nominal thicknesses 5, 6, and 7 nm. After fabrication, a series of areas on the gold films are illuminated by scanning a fs-pulsed laser at various powers across the films, Fig. 1a (see Methods). If the illumination is performed above a critical level of laser power, permanent morphological changes will be induced in the films. The degree and nature of this morphology reconfiguration can be controlled based on the scan parameters used, but principally depend on the laser power or wavelength used. Fig. 1b shows scanning transmission electron microscope (STEM) dark-field images of the intrinsic film morphologies, and examples of the effect of laser writing (a more detailed morphology study is available in ESI Fig. 1 and Discussion†). In Fig. 1b we observe that the reconfiguration of the gold films is remarkably different for percolated (7 nm) and unpercolated (5 and 6 nm) samples. Indeed, high powers in the writing laser will generate more isolated nanoparticles in gold films with thicknesses below the percolation threshold. This is in stark contrast to the percolated metal film where the film is already an inter-connected network of clusters, and it remains a network of connected gold clusters even for much larger laser powers.

To understand how the morphology changes are linked to changes in the plasmonic resonances in the intrinsic film, we present a simple toy model of resonant elongated particles that have their aspect ratios altered while maintaining their initial volume (see Methods). We can imagine that three

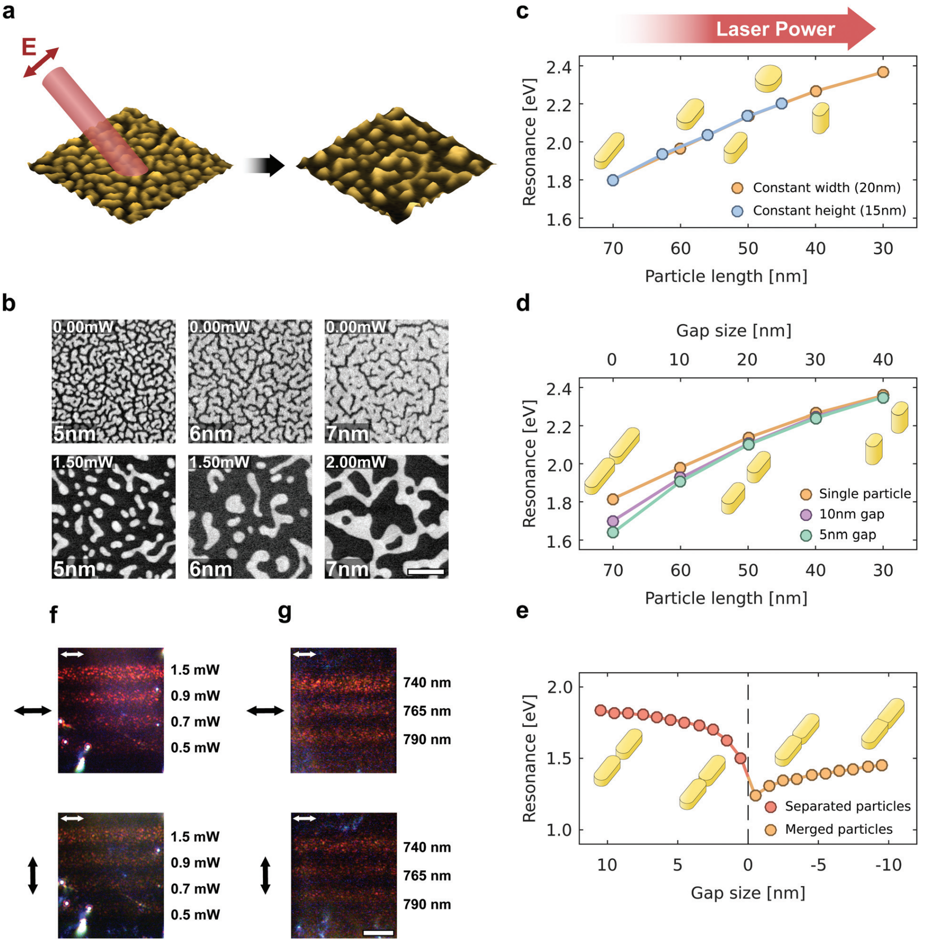

Fig. 1 Optical reconfiguration of thin gold films. (a) Schematic overview of the laser writing process used to alter sample morphology. (b) STEM dark-field images of intrinsic film morphologies and laser written morphologies. All images at same scale, scale bar is 150 nm. (c) Simulations of the blueshift of longitudinal resonance energy for a particle being shortened, and then either widened or increased in height to preserve particle volume. (d) Simulation results of the blueshift from opening of a gap between two plasmonic particles from shortening the particles. (e) Simulation of how closing of a plasmonic gap and merging the two particles (welding) causes a redshift in resonance energy. (f–g) Transmission dark-field images of stripes written in the gold films with (f) different laser powers with a 740 nm wavelength, and (g) with different laser wavelengths. White arrows on the images indicates the polarization of laser writing, black arrows on left show the polarization used for illumination when recording the image. Scale bar is 7.5 µm.

different scenarios will occur during the photothermal reshaping: Particle shortening/spherification, particle decoupling/gap widening, and particle fusion/welding. In Fig. 1c we highlight how shortening a particle while adding the 'lost' volume to either its height or width will result in a blueshift of the particle's longitudinal mode. This change in aspect ratios will correspond to the general contraction of a metal cluster into a more spherical shape due to the surface tension in the molten metal trying to minimize the particle's surface energy. In Fig. 1d we show how this kind of particle contraction (lost volume in length added to height) of two coupled particles will again result in a blueshift of the system's longitudinal mode from increasing the gap distance between them. When the two particles are sufficiently contracted, their coupling will also be

This journal is © The Royal Society of Chemistry 2017

broken and they will start resonating like two individual particles. This kind of morphology change will correspond to how plasmonically coupled clusters that are too far apart for particle welding/fusion will become decoupled. Finally in Fig. 1e we have the scenario of two metal clusters that are close enough to each other to fuse under laser writing. We here simulate the fusion process by progressively moving the two elongated particles closer to each other, and when they start to overlap (gap size of 0) the overlapping volume gets added to the resulting single particle's height. Both in terms of closing the gap distance and merging the two particles into one, a general redshift of the initial resonance is observed, with a strong shift at the merging point. After merging, the combined particle exhibits single particle behaviour (see Fig. 1c).

The effect of the laser writing on the gold films and its morphological changes can be observed with a microscope at low magnification, as shown in Fig. 1f and g. From Fig. 1f and g we see a clear difference between the illuminated and the unilluminated regions of the gold films from the distinctive colours that emerge from the morphological changes in the film. Interestingly, from Fig. 1f and g, we also see that the laser writing has left behind a polarization dependence in the films' optical properties, correlated with the polarization of the laser used to perform the writing, as a redder hue becomes visible when the polarization of the illumination in the microscope (black arrow) is aligned with the one used in the laser writing (white arrow).

Optical far-field properties of optical reconfigured gold films

To investigate the emergent red colour from laser writing in greater detail, we perform optical spectroscopy on our samples with an inverted microscope connected to a state of the art spectrometer (see Methods). From the bright-field transmission spectra of Fig. 2 (full data available in ESI Fig. 2†), when aligning the polarization of the light source in the transmission experiment parallel with the polarization of the laser used for the writing, we see a sharp decrease in transmission for photon energies in the range of 1.8–2.0 eV. When turning the polarization of the light source in our microscope to the perpendicular direction of the laser writing, this feature is strongly suppressed. On Fig. 2c we show for the 5 nm sample that the position of this feature is also dependent on the wavelength used for the writing process, with longer wavelengths also producing a feature deeper in the red part of the spectrum. For the 7 nm (and 6 nm) sample this feature is less pronounced for the lower powers used, but it still becomes apparent for sufficiently high writing powers. This can be understood from comparing the morphologies in Fig. 1b, as the thicker gold films seem generally less perturbed by the laser writing. We explain this from the fact that the 6 and 7 nm films appear to be close to and above the percolation threshold, respectively. As such, higher levels of laser power is needed to fully separate the particles as heat will be more efficiently conducted away from its injection point in a connected system.[47,48] Another observed trend is that the central position of the transmission feature tends to blueshift for increasing levels of laser power used for the writing. We attribute this to two effects. First, the individual particles become shortened for the higher writing powers, due to increasing spherification of the gold at higher temperatures, and secondly due to the likewise increasing thickness of the gold particles as the volume of gold that was previously covering the flat surface now accumulates into thicker particles (when we assume only minimal gold evaporation).

Statistical analysis of EELS intensity distributions

We have shown that laser-induced reshaping of the metal films has a strong effect on their optical far-field properties. In order to investigate the plasmonic properties of the individual particle clusters and gaps, we recorded high resolution EELS maps of the samples. Due to the highly random nature of the film morphologies, the specific detailed distribution of the

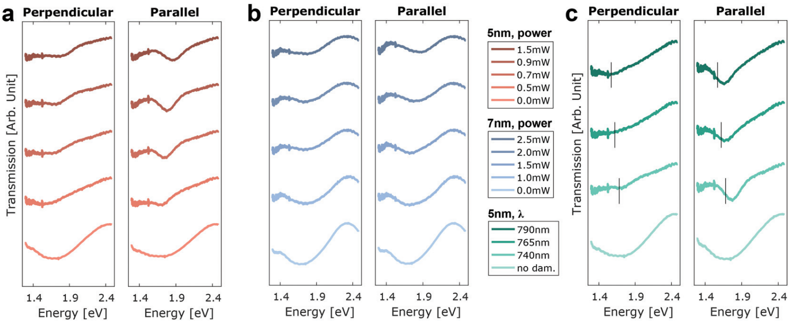

Fig. 2 Optical anisotropy. Polarized bright-field transmission spectra of the (a) 5 nm, (b) 7 nm films from regions illuminated with different laser powers, and (c) for illumination with different photon energies on the 5 nm sample. Vertical black lines indicate the photon energy of the laser used. The white-light source used to illuminate the samples in the measurements was polarized parallel or perpendicular to the polarization of the laser used for writing.

electric fields associated with the plasmon resonances is difficult to reproduce, making qualitative comparisons between samples difficult (example EELS maps are available in Fig. 3a). Secondly, comparisons between large sets of EELS maps for such random geometries can become very overwhelming to interpret. But, due to the self-similar and isotropic nature of the films, a quantitative statistical analysis of sufficiently large regions of the films can provide a reproducible and comparable probability distribution function (PDF) of the EELS intensity of a specific film morphology. Furthermore, the total shape of the PDF informs us on the degree of coupling between the plasmonic eigenmodes in the semi-continuous film. A Gaussian shape corresponds to plasmonic excitations coupled throughout the metal film, while a more power-law shape (see lines in Fig. 3e and f) corresponds to isolated plasmonic excitations.[31]

In order to construct PDFs of our EELS intensities, we take advantage of the methods of previous theoretical and experimental works on self-similar and fractal structures.[31,49,50] In short, for each spectral image we can extract the resonance energy and EELS intensity of the measured plasmons. By then binning the found intensities we form a distribution of intensities in the spectral image (*i.e.* a histogram). For each intensity value, this PDF then gives us the probability of finding this EELS intensity in the image (see methods for more details). The EELS intensity gives the probability of an electron losing a certain amount of energy along its trajectory through the sample, and it is proportional to the integral of the electric field induced in the sample along this trajectory by the electron.[44] As such, the EELS intensity is not itself a direct measure of the plasmonic electric field amplitude, but the two are strongly related.[44,51–53] We use this to justify the comparison of EELS intensity to previous measurements and calculations of the near-field intensities of semi-continuous metal films.

To extract the plasmon resonant energies and peak intensities from our background-corrected spectral images, we perform an iterative series of Gaussian fits on the individual spectra. First a set of energy ranges of interest are determined from taking an average of the full spectral image, and within these energy ranges individual Gaussian functions are fitted to a smoothing spline constructed from the data. The parameters of these fits are then used for initial guesses to fit a sum of Gaussian functions that are fitted to the full range of the individual spectra's datasets (see methods for more details). An example of these sequential fits can be seen in Fig. 3b. From the extracted peak central energies we can construct histograms of how the resonances are concentrated in terms of energy, and from the found peak intensities we can construct distribution functions of the EELS intensities in terms of their spectral position (Fig. 3c–f, and ESI Fig. 3–5†). For all of the films we see that prior to optical reconfiguration the central

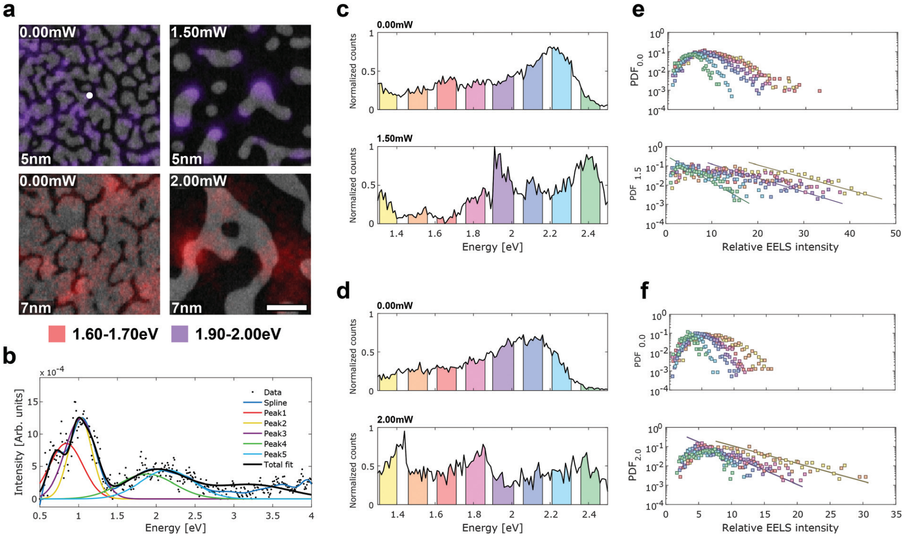

Fig. 3 Plasmonic resonance distribution. (a) Integrated EEL spectra overlaid on STEM dark-field images for 5 and 7 nm morphologies. Scale bar is 75 nm. (b) Example of an EEL spectrum and Gaussian fits used to extract peak central positions and energies, taken from the white dot in (a). Normalized histograms of identified central energies of plasmon resonances in the (c) 5 nm and (d) 7 nm films before and after laser writing. Constructed PDFs of the EELS intensity distributions for the intrinsic and reconfigured (e) 5 nm and (f) 7 nm samples. Straight lines added as a guide to the eye.

This journal is © The Royal Society of Chemistry 2017

energies of the detected plasmon resonances form a wide continuum with a slight peak in the distribution around 2.1–2.2 eV. The position of this peak in the distribution seems to redshift slightly for increasing film thickness. The constructed PDFs for the intrinsic films also show that the near-infrared and red part of the spectrum (1.3–1.8 eV) contributes with higher relative EELS intensities (seen from the total width of the PDFs), in agreement with prior experiments and the scaling theory for semi-continuous metal films predicting higher field enhancement for longer wavelengths.[31,54,55]

As the samples gets subjected to high laser powers, we see a dramatic redistribution of the resonance energies, as well as the intensity distributions (results for the full range of powers on the three film samples are available in ESI Fig. 3–5†). The effect is especially pronounced for the 5 nm sample, Fig. 3c and e, where increasing levels of power of laser writing gradually reshapes the PDFs from the normal distribution expected for these kinds of films, towards a scaling power-law of isolated dipoles.[31,49] We explain this from the morphology images in Fig. 1b and our toy model in Fig. 1c–e. For the high laser powers we see the inter-particle gaps increase significantly, and the resulting morphology consists mainly of isolated particles. As a result, the inter-particle coupling present in the intrinsic films has been lifted. This isolating and the reshaping into thicker and more spherical particles also explains why we generally see a strong blueshifting in the resonance energies in Fig. 3c. For the 7 nm sample we see a distinctly different morphology and resonance behaviour, compared to the 5 nm sample. For all levels of laser writing power the 7 nm sample remains a connected structure forming large networked clusters, where the small gaps that previously dominated the morphology either have fused or opened fully. The removal of these small features and their replacement by large connected clusters can help us to understand why the laser written film seems to have a large increase in red and near-infrared modes in Fig. 1d. From the fact that the structures also never become truly isolated, we can understand why the EELS intensity distributions for the laser written parts do not deviate as dramatically in their shape from the intrinsic PDFs, as in the 5 nm case. Interestingly, we are able to see a large increase in the relative EELS intensities from the ~1.9 eV part of the spectrum in the laser written parts of the 5 nm film, when compared with the intrinsic films. This increase in intensity also seems to become larger for increasing powers of laser writing, and it is worth noting that the energy corresponds to the reduction in far-field optical transmission observed for the parallel polarization for the 5 nm sample in Fig. 2a.

Polarization dependence

In order to qualitatively investigate the polarization dependence of the extinction features seen in the transmission spectra of Fig. 2, we have constructed EELS maps for the 5 nm film samples by integrating the EEL spectra in the 1.8–2.0 eV energy range, as seen in Fig. 4 (full energy ranges are available in ESI Fig. 7–10†). From these maps several elongated particles appear to host dipole-like plasmon resonances, that are predominantly aligned with the direction of the polarization of the laser used to induce the optical reconfiguration. To verify if these particles are dominated by a dipolar response in this energy range, we performed finite-element simulations of plane wave excitations with two orthogonal polarizations on

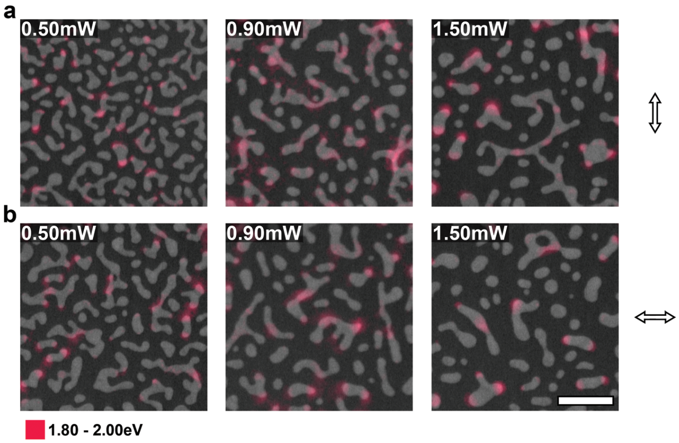

Fig. 4 EELS anisotropy. Colour maps of the recorded EEL spectra integrated in the energy range of 1.80–2.00 eV and overlaid on top of their respective STEM dark-field images of the 5 nm samples. Each row of images consists of samples with the same polarization used for laser writing (white arrows), (a) being the samples with *y*-polarized laser writing, and (b) the samples with *x*-polarized laser writing. The numbers in the top left corners of the images indicate the amount of power used for laser writing. The scale bar is 150 nm.

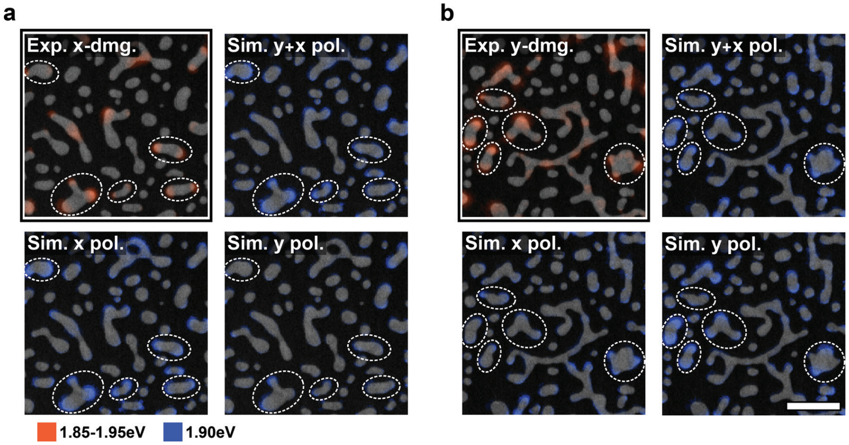

Fig. 5 Far-field simulations. Comparison between EELS data and the norms of electric field *z*-components from simulated polarized far-field excitation of the 1.5 mW laser written regions in the 5 nm sample. (a) For laser written with polarization along the images' *x*-axis, and (b) for the sample laser written along the *y*-axis. The EELS data was integrated in the region of 1.85–1.95 eV and the excitation energy for simulations was 1.90 eV. The electric field norms from the simulation were taken right below the gold particles. The scale bar is 150 nm.

the same film morphologies (see Methods). A comparison between the simulated field distributions and the measured EELS intensities can be seen in Fig. 5. Because the plane wave simulations allow us to make comparisons to the two excitation polarizations individually, we can now see how the measured plasmon resonances from the EELS data are decoupled in terms of polarization. With this we show that the suspected elongated particles are in fact behaving like strongly polarized nanorods with resonances in the same energy range as the features measured in the transmission experiments. A one-to-one comparison of EELS and plane-waves is usually difficult due to the inherent differences of the excitation sources.[37,56,57] The electron beam in EELS is able to excite plasmon modes that are normally inaccessible with optical fields,[58] and is also able to excite all different polarizations simultaneously.[44,51] However, here we are only interested in identifying the bright modes around 1.9 eV that are optically active in our transmission measurements. We expect from this comparison to identify the polarization dependence of the plasmonic modes in the reshaped films (Fig. 2). Similar comparison between hyperspectral imaging and finite-difference simulations have been used to identify the polarization dependence of the optical response of resonant wedge-plasmons[59] and of toroidal modes in heptamer and hexamer nanocavities.[60]

Conclusions

In summary, we have characterized the morphological and plasmonic restructuring of semi-continuous gold films of nominal thicknesses 5, 6, and 7 nm when subjected to fs-laser pulses of different powers (Fig. 1 and ESI Fig. 1†). This kind of optical reconfiguration becomes apparent in the far-field properties of the films, as a resonant feature is seen in the transmission spectra from the laser written areas of the films. When the samples are illuminated with a polarized light source that is aligned to the polarization of the laser used for the optical reconfiguration, a strong decrease in transmission is observed. Furthermore, the spectral position of this transmission feature can be controlled by varying the laser wavelength and power when performing the optical reconfiguration (Fig. 2). By measuring EELS maps from selected regions of the altered and intrinsic parts of the samples, we have constructed histograms of the central energies of the plasmon resonances present in the films, as well as PDFs of the EELS intensity distributions for different resonance energies (Fig. 3 and ESI Fig. 2–4†). From these we conclude that generally the resonances at longer wavelengths have higher EELS intensities in the intrinsic films, while in the altered films we observe a redistribution of the resonances that contribute to the largest EELS intensities, in qualitative agreement to our toy model. The intensities in reconfigured films are also generally higher overall, when compared to the intrinsic films. Finally, we have investigated the origin of the polarization dependence of the features observed in the transmission experiments, by plotting EELS intensity maps of energies related to the measured decrease in transmissions (Fig. 4). We have performed finite-element simulations to reconstruct the electric field distributions in our sample morphologies from polarized far-field excitation. We compare these to the measured EELS intensities to confirm that the resonant particles formed after laser writing are responsible for the polarization dependence of the measured transmission spectra (Fig. 5).

These types of metallic films have previously been demonstrated to function as SERS substrates.[19,61–64] We show here that it is possible to convert the broad ensemble of different plasmonic resonances found in these films into a more narrow band of resonances, making the films more selectively resonant for a specific wavelength and polarization of light. This could potentially be used to further increase the enhancement factor from such films in SERS applications, by tuning and enhancing the resonances towards the wavelength and polarization of the laser used in the Raman experiment. New sensing applications could also harvest the potential of these kinds of metal films.

Finally, we have shown that by using a different laser wavelength or power when performing the optical reconfiguration it is possible to tune the wavelength of the resulting resonant particles created in the film. This could be useful for plasmonic colour printing by laser writing, as it would be possible to inscribe pixels of different colours into the films by use of different wavelengths and powers, constructing a colour image that would be visible clearly when viewing the film through a correctly aligned polarizer. The spatial resolution of this writing method will at least be diffraction limited, as observed in our previous work (see Fig. 4 in ref. 28). Although nonlinear effects could increase this resolution, as seen in multiphoton absorption lithography.[65,66] This could be the scope of future investigations. Recent experiments have already been performed demonstrating laser writing,[11] but rely on using specifically fabricated substrate structures. The ease with which these metal films can be fabricated, even at very large-scale areas, could offer an alternative low-cost substrate structure for emerging plasmonic colour printing technologies, as well as applications in ultra-dense data storage media.[9]

Experimental

Sample fabrication

Thin gold films of 5, 6, and 7 nm nominal thicknesses were deposited onto 18 nm thick SiO_2 TEM membranes from Ted Pella, Inc. using an electron beam deposition system. The gold was deposited with a constant rate of 2 Å s^{-1}, with the total deposition time defining the thickness of the final film. Chamber pressure was maintained at $\sim 10^{-5}$ mbar and deposition was on room temperature substrates.

Optical reconfiguration

The laser writing is performed with a two-photon photoluminescence (TPL) setup, consisting of a scanning optical microscope in reflection geometry built based on a commercial microscope with a computer-controlled translation stage. The linearly polarized light beam from a mode-locked pulsed (pulse duration ∼200 fs, repetition rate ∼80 MHz) Ti-Sapphire laser (wavelength λ = 730–860 nm, $\delta\lambda \sim 10$ nm, average power ∼300 mW) is used to locally restructure the gold film at the fundamental harmonic (FH) frequency. After passing an optical isolator (to suppress back-reflection), half-wave plate, polarizer, red colour filter and wavelength selective beam splitter, the laser beam is focused on the sample surface at normal incidence with a Mitutoyo infinity-corrected long working distance objective (100×, NA = 0.70). The FH resolution at full-width-half-maximum is ∼0.75 μm. The half-wave plate and polarizer allows accurate adjustment of the incident power. The laser writing was done with the following scan parameters: Integration time (at one point) of 50 ms, speed of scanning (between the measurement points) of 20 μm s^{-1}, and scanning step size of 350 nm. The incident power was within the range 0.5–2.0 mW. Unless stated otherwise, the excitation wavelength was fixed at 740 nm. We should mention that with this laser power, morphology changes could only be induced in the pulsing regime of the laser.

Optical spectroscopy

Bright-field transmission spectra were recorded from the intrinsic and laser written regions of the samples on the TEM membranes. A custom spectroscopy setup built from a Nikon Eclipse Ti-U Inverted microscope was used. The system is fitted with a halogen white-light source with peak emission at 675 nm. The light is collected by a CFI S Plan Fluor ELWD objective from Nikon (60×, NA = 0.70), and the spectra are recorded using a Shamrock 303i Spectrometer equipped with a Newton 970 EMCCD. A LPVISE200-A visible linear polarizer from Thorlabs is placed between the light source and sample stage, allowing for polarized illumination. Spectra are collected for polarizations perpendicular and parallel to the optically induced changes in the gold films. The transmission spectra are corrected for the spectral profile of the halogen lamp by recording a reference spectrum through a similar glass slide as the membranes are mounted on, for both polarizer positions. After dividing the intensities point by point with the reference, the final spectrum is obtained by averaging over the individual laser modified areas (∼20 pixels on the CCD) and normalizing with the maximum value for comparison.

STEM and EELS measurements

The EELS measurements were performed with a FEI Titan TEM equipped with a monochromator and a probe aberration corrector. The microscope was operated in STEM mode at an acceleration voltage of 120 kV, with a probe diameter of 0.5 nm and with zero-loss peak (ZLP) full-width-half-maximums of ∼0.2 eV. For spectral images, 500 × 500 nm^2 areas were scanned with 5–8 nm step sizes, using larger step sizes for the films modified by high laser powers. Before imaging, the samples were cleaned in an O_2-plasma for 45 s.

From the width of the ZLP, its central position is determined and the energy scale of the spectra is shifted to zero for this position. The spectra are then normalized by integrating the background signal found in the higher energies of the spectrum. After normalization the ZLP is subtracted by performing a series of power law fits, and the fit producing the minimum residual is picked. The full background corrected spectral image is averaged together, and a sum of Gaussian functions are fitted to the now emerging 'primary modes' of the image, *i.e.* the modes so sufficiently common or intense that they contribute overwhelmingly to the total average of the spectral image. A smoothing spline is then constructed for each individual spectra's data. These smoothing splines are then segmented within the full-width-half-maximum of the Gaussian functions fitted to the 'primary modes', and within each of these data segments a Gaussian function is fitted. The quality of these individual fits are then evaluated to determine if a peak is present in this energy range of the spectrum or not. From each segment of the spectrum, we now get the information if a peak is present, and if so, what its amplitude and central position is. Using these values for initial guesses, a sum of Gaussian functions are then fitted to the full range of the spectrum's dataset and the plasmon resonance energies and EELS intensities are extracted from these fits.

Statistical analysis

Using the central position of the Gaussian fits described above, a histogram can be constructed of identified central energies, with bin sizes of 0.01 eV, matching the energy resolution of the TEM's detector. The PDFs of discretized windows of the energy range are constructed from the corresponding amplitudes of the Gaussian fits with central energies in those windows. Each energy window is 0.10 eV wide, and to construct the PDF the fitted amplitudes are binned into 30 equally wide bins of intensities. We have estimated a base level intensity as the median of the 50 lowest identified amplitudes from each of the spectral images for each sample. All the identified intensities for each energy window are then normalized with respect to this base level intensity to be represented in terms of a relative EELS intensity.

Simulations

Full-wave 3D simulations of the gold structures were carried out using the finite-element software package COMSOL Multiphysics (v5.1). The simulation domain was truncated with perfectly matched layers from all sides. The system was solved in a scattered wave formulation, with analytical solution for three layer system (air–glass–air) as the background field. A custom Python script was used, which generated the simulation geometry from the outlines that were extracted from the binaries of STEM dark-field images (see ESI Methods†). The particles were represented as straight prisms in the 3D geometry. The relative thicknesses, t_r, of the gold films have been calculated by $t_r = \log(I_{tot}/I_{ZLP})$, where I_{ZLP} is the integral of the ZLP in the EEL spectrum, and I_{tot} is the total integral of the EEL spectrum, ranging from 0–17 eV. Calculating this for each pixel in our spectral images, and performing a plane background correction to this, provided the relative height map for the samples. By averaging the height map values inside the particle contours, the relative heights of the particles were obtained. The tallest particles were set to a height of 28 nm, as this provides the best correlation to the EELS measurements. An example of obtained particle contours and their relative heights are shown in ESI Fig. 6.†

Simulations for Fig. 1c–e are based on a similar setup. One or two nanorods are placed on the glass membrane. Calculations for Fig. 1c are done with a single nanorod that is composed of a rectangular prism (width w, height h, length l) with semi-cylindrical caps (radius $w/2$) at both ends. A series of calculations was done, for various lengths of the particle. For each particle size an absorption spectrum was calculated and the corresponding resonance peak was found. The particle size was varied to model the melting process, but the particle volume ($V = h(wl + 2\pi w^2/4)$) was kept constant either by scaling the particle height (h) or particle width (w).

For Fig. 1d we simulated two nanorods, with fixed centre positions. Consequently, as the particle length was reduced the gap between the nanorods increased. Particle height was scaled to keep the volume of the particles constant as they decreased in length.

For Fig. 1e the particle length was kept constant but the distance between the two particles varied. For positive gap sizes the particle shape stayed constant, but for negative gap sizes (particle overlap) the particle height was increased to keep the volume of the merged particle equal to the volume of the two initial particles.

Acknowledgements

The authors gratefully acknowledge financial support from the Danish Council for Independent Research-Natural Sciences (Project 1323-00087). S. I. B. acknowledges the European Research Council, Grant 341054 (PLAQNAP). N. A. M. is a Villum Investigator supported by Villum Fonden, Grant 1401500. Center for Nano Optics was financially supported from the University of Southern Denmark (SDU 2020 funding), while Center for Nanostructured Graphene (CNG) was funded by the Danish National Research Foundation (CoEProject DNRF103). T. R. acknowledges support from Archimedes Foundation (Kristjan Jaak scholarship) and Villum Fonden (DarkSILD project). The A. P. Møller and Chastine Mc-Kinney Møller Foundation is gratefully acknowledged for the contribution towards the establishment of the Center for Electron Nanoscopy. The microscope for optical characterization used in this work is funded by the Danish National Research Foundation (DNRF122), Villum Fonden (Grant No. 9301) and European Research Council Proof of Concept (Grant No. 713474).

C. F. would like to personally thank Søren Raza, Kåre Wedel Jacobsen, and Johan Rosenkrantz Maack for many valuable discussions during this work.

The authors would also like to thank Shima Kadkhodazadeh for her assistance with performing EELS measurements.

References

1 J. A. Schuller, E. S. Barnard, W. Cai, Y. C. Jun, J. S. White and M. L. Brongersma, *Nat. Mater.*, 2010, **9**, 193–204.

This journal is © The Royal Society of Chemistry 2017

2 T. Y. Jeon, D. J. Kim, S.-G. Park, S.-H. Kim and D.-H. Kim, *Nano Convergence*, 2016, **3**, 18.

3 Z.-W. Li, Y.-H. Hu, Y. Li and Z.-Y. Fang, *Chin. Phys. B*, 2017, **26**, 036802.

4 T. Low, A. Chaves, J. D. Caldwell, A. Kumar, N. X. Fang, P. Avouris, T. F. Heinz, F. Guinea, L. Martin-Moreno and F. Koppens, *Nat. Mater.*, 2017, **16**, 182–194.

5 M. S. Tame, K. McEnery, Ş. Özdemir, J. Lee, S. Maier and M. Kim, *Nat. Phys.*, 2013, **9**, 329–340.

6 M. Pelton, *Nat. Photonics*, 2015, **9**, 427–435.

7 S. I. Bozhevolnyi and N. A. Mortensen, *Nanophotonics*, 2017, **6**, DOI: 10.1515/nanoph-2016-0179.

8 A. Kristensen, J. K. W. Yang, S. I. Bozhevolnyi, S. Link, P. Nordlander, N. J. Halas and N. A. Mortensen, *Nat. Rev. Mater.*, 2016, **2**, 16088.

9 P. Zijlstra, J. W. Chon and M. Gu, *Nature*, 2009, **459**, 410.

10 K. Kumar, H. Duan, R. S. Hegde, S. C. W. Koh, J. N. Wei and J. K. W. Yang, *Nat. Nanotechnol.*, 2012, **7**, 557–561.

11 X. Zhu, C. Vannahme, E. Højlund-Nielsen, N. A. Mortensen and A. Kristensen, *Nat. Nanotechnol.*, 2016, **11**, 325–329.

12 Z. F. X. Zhu, *Adv. Mater.*, 2013, **25**, 3840–3856.

13 Y. Chen, *Microelectron. Eng.*, 2015, **135**, 57–72.

14 C.-S. Kim, S.-H. Ahn and D.-Y. Jang, *Vacuum*, 2012, **86**, 1014–1035.

15 P. Colson, C. Henrist and R. Cloots, *J. Nanomater.*, 2013, **2013**, 948510.

16 A. Klinkova, R. M. Choueiri and E. Kumacheva, *Chem. Soc. Rev.*, 2014, **43**, 3976–3991.

17 C. Xi, P. F. Marina, H. Xia and D. Wang, *Soft Matter*, 2015, **11**, 4562–4571.

18 S. Gwo, H.-Y. Chen, M.-H. Lin, L. Sun and X. Li, *Chem. Soc. Rev.*, 2016, **45**, 5672–5716.

19 V. M. Shalaev, *Nonlinear optics of random media: fractal composites and metal-dielectric films*, Springer, Heidelberg, 2007, vol. 158.

20 A. Hu, P. Peng, H. Alarifi, X. Zhang, J. Guo, Y. Zhou and W. Duley, *J. Laser Appl.*, 2012, **24**, 042001.

21 E. C. Garnett, W. Cai, J. J. Cha, F. Mahmood, S. T. Connor, M. G. Christoforo, Y. Cui, M. D. McGehee and M. L. Brongersma, *Nat. Mater.*, 2012, **11**, 241–249.

22 L. O. Herrmann, V. K. Valev, C. Tserkezis, J. S. Barnard, S. Kasera, O. A. Scherman, J. Aizpurua and J. J. Baumberg, *Nat. Commun.*, 2014, **5**, 4568.

23 J. Mertens, A. Demetriadou, R. W. Bowman, F. Benz, M.-E. Kleemann, C. Tserkezis, Y. Shi, H. Y. Yang, O. Hess, J. Aizpurua, *et al.*, *Nano Lett.*, 2016, **16**, 5605–5611.

24 X. Zhu, W. Yan, U. Levy, N. A. Mortensen and A. Kristensen, *Sci. Adv.*, 2017, **3**, e1602487.

25 J. E. Greene, *Handbook of Deposition Technologies for Films and Coatings*, William Andrew Publishing, Boston, 3rd edn, 2010, ch. 12, pp. 554–620.

26 J. Venables, G. Spiller and M. Hanbucken, *Rep. Prog. Phys.*, 1984, **47**, 399.

27 V. Shchukin, N. N. Ledentsov and D. Bimberg, *Epitaxy of nanostructures*, Springer Science & Business Media, 2013.

28 S. M. Novikov, C. Frydendahl, J. Beermann, V. A. Zenin, N. Stenger, V. Coello, N. A. Mortensen and S. I. Bozhevolnyi, *ACS Photonics*, 2017, **4**, 1207–1215.

29 S.-F. Wu, *Front. Phys. China*, 2006, **1**, 263–274.

30 S. Ducourtieux, V. Podolskiy, S. Grésillon, S. Buil, B. Berini, P. Gadenne, A. Boccara, J. Rivoal, W. Bragg, K. Banerjee, *et al.*, *Phys. Rev. B: Condens. Matter*, 2001, **64**, 165403.

31 D. A. Genov, K. Seal, M. A. Nelson, A. K. Sarychev, Z. C. Ying and V. M. Shalaev, *Physica B*, 2003, **338**, 228–231.

32 J. Nelayah, M. Kociak, O. Stéphan, F. J. G. de Abajo, M. Tencé, L. Henrard, D. Taverna, I. Pastoriza-Santos, L. M. Liz-Marzán and C. Colliex, *Nat. Phys.*, 2007, **3**, 348–353.

33 B. Ögüt, N. Talebi, R. Vogelgesang, W. Sigle and P. A. Van Aken, *Nano Lett.*, 2012, **12**, 5239–5244.

34 J. A. Scholl, A. L. Koh and J. A. Dionne, *Nature*, 2012, **483**, 421.

35 J. A. Scholl, A. García-Etxarri, A. L. Koh and J. A. Dionne, *Nano Lett.*, 2013, **13**, 564–569.

36 S. Raza, N. Stenger, A. Pors, T. Holmgaard, S. Kadkhodazadeh, J. B. Wagner, K. Pedersen, M. Wubs, S. I. Bozhevolnyi and N. A. Mortensen, *Nat. Commun.*, 2014, **5**, 4125.

37 S. Raza, S. Kadkhodazadeh, T. Christensen, M. Di Vece, M. Wubs, N. A. Mortensen and N. Stenger, *Nat. Commun.*, 2015, **6**, 8788.

38 N. Talebi, W. Sigle, R. Vogelgesang, M. Esmann, S. F. Becker, C. Lienau and P. A. van Aken, *ACS Nano*, 2015, **9**, 7641–7648.

39 S. Raza, M. Esfandyarpour, A. L. Koh, N. A. Mortensen, M. L. Brongersma and S. I. Bozhevolnyi, *Nat. Commun.*, 2016, **7**, 13790.

40 R. G. Hobbs, V. R. Manfrinato, Y. Yang, S. A. Goodman, L. Zhang, E. A. Stach and K. K. Berggren, *Nano Lett.*, 2016, **16**, 4149–4157.

41 M. Bosman, G. R. Anstis, V. J. Keast, J. D. Clarke and M. B. Cortie, *ACS Nano*, 2011, **6**, 319–326.

42 A. Losquin, S. Camelio, D. Rossouw, M. Besbes, F. Pailloux, D. Babonneau, G. A. Botton, J.-J. Greffet, O. Stéphan and M. Kociak, *Phys. Rev. B: Condens. Matter*, 2013, **88**, 115427.

43 C. Gritti, S. Raza, S. Kadkhodazadeh, B. Kardynal, R. Malureanu, N. A. Mortensen and A. V. Lavrinenko, *Nanophotonics*, 2017, **6**, 289–297.

44 F. J. García de Abajo, *Rev. Mod. Phys.*, 2010, **82**, 209–275.

45 C. Colliex, M. Kociak and O. Stéphan, *Ultramicroscopy*, 2016, **162**, A1–A24.

46 K. Seal, M. A. Nelson, Z. C. Ying, D. A. Genov, A. K. Sarychev and V. M. Shalaev, *Phys. Rev. B: Condens. Matter*, 2003, **67**, 035318.

47 T. Andersson, *J. Phys. D: Appl. Phys.*, 1976, **9**, 973.

48 Y. Namba, *Jpn. J. Appl. Phys.*, 1970, **9**, 1326.

49 M. I. Stockman, L. N. Pandey, L. S. Muratov and T. F. George, *Phys. Rev. Lett.*, 1994, **72**, 2486.

50 S. I. Bozhevolnyi and V. Coello, *Phys. Rev. B: Condens. Matter*, 2001, **64**, 115414.

51 M. Kociak and O. Stéphan, *Chem. Soc. Rev.*, 2014, **43**, 3865–3883.

This journal is © The Royal Society of Chemistry 2017

52 P. Shekhar, M. Malac, V. Gaind, N. Dalili, A. Meldrum and Z. Jacob, *ACS Photonics*, 2017, **4**, 1009–1014.

53 A. Losquin and T. T. A. Lummen, *Front. Phys.*, 2017, **12**, 127301.

54 A. K. Sarychev, V. Shubin and V. M. Shalaev, *Phys. Rev. B: Condens. Matter*, 1999, **60**, 16389.

55 A. K. Sarychev and V. M. Shalaev, *Phys. Rep.*, 2000, **335**, 275–371.

56 M. Husnik, F. von Cube, S. Irsen, S. Linden, J. Niegemann, K. Busch and M. Wegener, *Nanophotonics*, 2013, **2**, 241–245.

57 T. Christensen, W. Yan, S. Raza, A.-P. Jauho, N. A. Mortensen and M. Wubs, *ACS Nano*, 2014, **8**, 1745–1758.

58 U. Hohenester, H. Ditlbacher and J. R. Krenn, *Phys. Rev. Lett.*, 2009, **103**, 106801.

59 L. Gu, W. Sigle, C. T. Koch, B. Ögüt, P. A. van Aken, N. Talebi, R. Vogelgesang, J. Mu, X. Wen and J. Mao, *Phys. Rev. B: Condens. Matter*, 2011, **83**, 195433.

60 N. Talebi, B. Ögüt, W. Sigle, R. Vogelgesang and P. Aken, *Appl. Phys. A*, 2014, **116**, 947–954.

61 P. Gadenne, D. Gagnot and M. Masson, *Physica A*, 1997, **241**, 161–165.

62 V. P. Drachev, M. D. Thoreson, V. Nashine, E. N. Khaliullin, D. Ben-Amotz, V. J. Davisson and V. M. Shalaev, *J. Raman Spectrosc.*, 2005, **36**, 648–656.

63 J. Perumal, K. V. Kong, U. Dinish, R. M. Bakker and M. Olivo, *RSC Adv.*, 2014, **4**, 12995–13000.

64 S. M. Novikov, J. Beermann, C. Frydendahl, N. Stenger, V. Coello, N. A. Mortensen and S. I. Bozhevolnyi, *Opt. Express*, 2016, **24**, 16743–16751.

65 S. Kawata, H.-B. Sun, T. Tanaka and K. Takada, *Nature*, 2001, **412**, 697–698.

66 M. Deubel, G. Von Freymann, M. Wegener, S. Pereira, K. Busch and C. M. Soukoulis, *Nat. Mater.*, 2004, **3**, 444–447.

This journal is © The Royal Society of Chemistry 2017

Christian Frydendahl received a BSc (2011) and a MSc (2013) in physics from the Department of Physics and Astronomy (IFA), Aarhus University (AU), Denmark.

In 2014 he started his PhD-study at The Technical University of Denmark (DTU), at the Department of Photonics Engineering (DTU Fotonik). The study has been performed in the groups of "*Structured Electromagnetic Materials*" and "*Plasmonics and Metamaterials*", and was supervised by Assoc. Prof. Nicolas Stenger, Assoc. Prof. Andrei V. Lavrinenko, and Prof. N. Asger Mortensen (now of University of Southern Denmark).

The thesis was successfully defended on November 2nd, 2017. The evaluation committee consisted of Prof. Mark I. Stockman, Prof. Uriel Levy, and Prof. Peter Uhd Jepsen.

Metallic nanostructures can support so-called plasma oscillations (plasmons). Plasmons allow for the concentration of the energy from light, down to sizes well below the conventional diffraction limit known from optics. Plasmonics thus allows for a plethora of new optical applications at the nanoscale.

In this thesis, we have investigated the optical and plasmonic properties of semi-continuous gold films (also called percolation films). These films consist of complex tortuous fractal patterns on the nanoscale. They are an easy, fast, and scalable method to fabricate metallic nanostructures.

We show, that despite their very complex overall geometry, a large part of the films' properties can be understood alone based on their strongly localized plasmonic 'hotspots' – areas of just a few nanometres in the films, wherein optical fields are enhanced several thousand times.

Additionally, we show that such films can be used for the enhancement of gold two-photon photoluminescence and white light continuum generation. We have also shown that it is possible, via femtosecond-laser pulses, to inscribe information into the films, *via* phototheral processes. This has potential applications for ultra-dense information storage, and plasmonic colour laser printing.

Technical University of Denmark
Department of Photonics Engineering
Ørsteds Plads, building 343
DK-2800, Kgs. Lyngby

http://www.fotonik.dtu.dk/